NASA/CR-2010-216697

Developments and Validations of Fully Coupled CFD and Particle Vortex Transport Method for High-Fidelity Wake Modeling in Fixed and Rotary Wing Applications

Phuriwat Anusonti-Inthra
National Institute of Aerospace, Hampton, Virginia

May 2010

NASA STI Program . . . in Profile

Since its founding, NASA has been dedicated to the advancement of aeronautics and space science. The NASA scientific and technical information (STI) program plays a key part in helping NASA maintain this important role.

The NASA STI program operates under the auspices of the Agency Chief Information Officer. It collects, organizes, provides for archiving, and disseminates NASA's STI. The NASA STI program provides access to the NASA Aeronautics and Space Database and its public interface, the NASA Technical Report Server, thus providing one of the largest collections of aeronautical and space science STI in the world. Results are published in both non-NASA channels and by NASA in the NASA STI Report Series, which includes the following report types:

- TECHNICAL PUBLICATION. Reports of completed research or a major significant phase of research that present the results of NASA programs and include extensive data or theoretical analysis. Includes compilations of significant scientific and technical data and information deemed to be of continuing reference value. NASA counterpart of peer-reviewed formal professional papers, but having less stringent limitations on manuscript length and extent of graphic presentations.

- TECHNICAL MEMORANDUM. Scientific and technical findings that are preliminary or of specialized interest, e.g., quick release reports, working papers, and bibliographies that contain minimal annotation. Does not contain extensive analysis.

- CONTRACTOR REPORT. Scientific and technical findings by NASA-sponsored contractors and grantees.

- CONFERENCE PUBLICATION. Collected papers from scientific and technical conferences, symposia, seminars, or other meetings sponsored or co-sponsored by NASA.

- SPECIAL PUBLICATION. Scientific, technical, or historical information from NASA programs, projects, and missions, often concerned with subjects having substantial public interest.

- TECHNICAL TRANSLATION. English-language translations of foreign scientific and technical material pertinent to NASA's mission.

Specialized services also include creating custom thesauri, building customized databases, and organizing and publishing research results.

For more information about the NASA STI program, see the following:

- Access the NASA STI program home page at *http://www.sti.nasa.gov*

- E-mail your question via the Internet to help@sti.nasa.gov

- Fax your question to the NASA STI Help Desk at 443-757-5803

- Phone the NASA STI Help Desk at 443-757-5802

- Write to:
  NASA STI Help Desk
  NASA Center for AeroSpace Information
  7115 Standard Drive
  Hanover, MD 21076-1320

NASA/CR-2010-216697

Developments and Validations of Fully Coupled CFD and Particle Vortex Transport Method for High-Fidelity Wake Modeling in Fixed and Rotary Wing Applications

Phuriwat Anusonti-Inthra
National Institute of Aerospace, Hampton, Virginia

National Aeronautics and
Space Administration

Langley Research Center
Hampton, Virginia 23681-2199

Prepared for Langley Research Center
under Contract NNL07AA32C

May 2010

Available from:

NASA Center for AeroSpace Information
7115 Standard Drive
Hanover, MD 21076-1320
443-757-5802

Abstract

A novel Computational Fluid Dynamics (CFD) coupling framework that uses a conventional Reynolds-Averaged Navier-Stokes (RANS) solver to resolve the flow field near the body and Particle-based Vorticity Transport Method (PVTM) to predict the evolution of the far field wake is developed, refined, and evaluated for fixed and rotary wing cases. For rotary wing case the RANS/PVTM modules are loosely coupled to a Computational Structural Dynamics (CSD) module that provides blade motion and vehicle trim information. The results from the coupled framework are compared with several experimental data sets (a fixed-wing wind tunnel test and a rotary-wing hover test). The PVTM module is refined by the additions of vortex diffusion, stretching, and reorientation models as well as an efficient memory model. Validation with the fixed-wing wind tunnel test data shows that the coupled RANS/PVTM method provides good prediction on wing performance (pressure distribution and sectional loads) and tip vortex parameters (core size, location and swirl velocity). For the rotary wing under hover condition, the results from the coupled RANS/PVTM/CSD framework correlate well with the hover test data, however the simulation over-predicts the rotor torque by about 50%. Overall, the tip vortex parameter validations are good. The tip vortex swirl velocity is slightly over-predicted, and the difference in tip vortex trajectory is within one chord length over 150° wake age. Significant improvement on the correlations of vortex trajectory and swirl velocity is observed when the vortex stretching model is used in the PVTM module.

Table of Contents

Lists of Tables

Lists of Figures

Notation

Abbreviations

2D	Two dimensional
3D	Three dimensional
BVI	Blade Vortex Interaction
CAMRAD	Comprehensive Analytical Model of Rotorcraft Aerodynamics and Dynamics
CFD	Computational Fluid Dynamics
CSD	Computational Structural Dynamics
CII-FW	CAMRAD II (free wake)
CII-LI	CAMRAD II (linear inflow)
DLR	German Aerospace Center
HART	Higher Harmonic Control Aeroacoustic Rotor Test
HOTIS	Hover Tip Vortex Structure Test
LES	Large Eddy Simulation
MPI	Message Passing Interface
NASA	National Aeronautics and Space Adminsistration
NIA	National Institute of Aerospace
PIV	Particle Image Velocimetry
PVTM	Particle-based Vorticity Transport Method
RANS	Reynolds Averaged Navier-Stokes
RK	Runge-Kutta
VTM	Vorticity Transport Method

Symbols

A	Area of boundary
A_m	Measure of time integration accuracy
A_ε	Strain tensor
c	Chord length
C_C	Chordwise force coefficient
C_D	Drag coefficient
C_L	Lift coefficient
C_Q	Rotor thrust coefficient
C_M	Moment coefficient
C_N	Normal force coefficient
C_T	Rotor torque coefficient
d	PVTM cell size
E	Internal energy density
f_{ij}	Diffusion redistribution factor
h	Effective diffusion distance
L	number of PVTM levels
L_c	Characteristic length
M	Mach number

N	number of vortex particles
$\hat{n}$	Outward normal vector
P	Pressure
R	Rotor radius
Re	Reynolds number
r	radial station
S	Vorticity source
t, T	Time
u	Velocity vector
V	Volume and Velocity vector
V_θ	Tip vortex wirl velocity
x,y,z	Location vector of vortex particle
α	Vorticity strength vector of vortex particle ($\int \omega dV$)
δ	Desingularized parameter
ε	Desired accuracy
$\hat{\varepsilon}$	Principle strain
Γ	Vorticity strength
η	Attraction coefficient
θ_{75}	Collective control
ρ	Density
λ	Eigenvalue of A_ε
χ	Eigenvector
ω	Vorticity
ν	Kinematic viscosity
$(\,)^k$	Quantity at time step k
$(\,)_i$	Quantity at time step k

Operators

∇	$= \frac{\partial}{\partial x} i + \frac{\partial}{\partial y} j + \frac{\partial}{\partial z} k$
$\dot{(\,)}$	$= \frac{\partial}{\partial t}$

Acknowledgements

The financial support for this current research from NASA under Contract NNL07AA32C, with Dr. Doug Nark as a technical monitor, is gratefully acknowledged. The author is also grateful for the financial support for the initial investigation prior to this current research from another NASA Contract NAS1-2117, Task Order NNL04AA96T (Rotorcraft Aeromechanics) with Dr. Mark W. Nixon (Army Research Laboratory) as a technical monitor.

The author also would like to thank Dr. Yi Liu, Dr. Doug Nark, Dr. Doug Boyd, Ms. Casey Burley, Dr. Berend van der Wall, and Dr. Wayne Johnson for their valuable technical guidance and suggestions.

Access to NASA Advanced Supercomputing (NAS) facility is gratefully acknowledged.

Chapter I

Introduction

1.1 Background and motivation

Accurately predicting the long-term dynamics of the wake produced by wings and rotors under high Reynolds number flow condition is still one of the most challenging tasks for CFD simulations. The wake structure behind a wing under such condition, in the simplest form, consists of vortex sheet from the boundary layer and a strong tip vortex from 3D finite wing effects. The tip vortex is quickly formed and is normally well organized before leaving the wing trailing edge [1.1]. Typical velocity profiles of the wing tip vortices can be found in Ref. [1.2]. The tip vortex continues strengthening after leaving the trailing edge by rolling in the vortex sheet. Then the viscous diffusion effect causes the tip vortex to grow in size and lose strength very slowly as it convects downstream.

The wake structure from a rotor is much more complex since all the vortex sheets, tip, and root vortices released from all of the blades are intertwined due to the rotation of the blades to form a helical wake structure [1.3]-[1.4]. Unlike the wake from wings, the helical structure of rotor wake produces very strong blade-wake and wake-wake aerodynamic interactions. The blade-wake aerodynamic interaction often causes the unpleasant Blade Vortex Interaction (BVI) noise [1.5].

Many researchers have simulated the wing and rotor wake flow successfully using a variety of classical and physics-based approaches. Simulations of the wake flow behind wings were attempted using vortex filament method [1.6], vortex panel method [1.7], a classical wing theory [1.8], Computational Fluid Dynamics (CFD) [1.9], and vortex particle method [1.10]. The CFD calculations in Ref. [1.9] used two CFD solvers (Reynolds-Averaged Navier-Stokes (RANS) and hybrid Euler/Large Eddy Simulation (LES) solvers) to compute aircraft wake very far

downstream, with an equivalent distance of more than two nautical miles (~500*c*) for a typical commercial aircraft. With the vortex particle method [1.10], a high resolution wake from an aircraft was simulated using billions of vortex particles.

Four major approaches were used to simulate rotor wake flow - *(i)* vortex lattice, *(ii)* vortex blob or particle, *(iii)* full Computational Fluid Dynamics (CFD), and *(iv)* Vorticity Transport Method (VTM). The first and most widely used method for rotor wake prediction is using vortex lattices to represent the shed and trailed vorticity generated by the rotor [1.3]-[1.4]. Both straight and curved vortex lattices have been considered. Generally, these vortex elements are free to move with local velocity induced by other vortex elements in the flow field, however less sophisticated rigid wake models use empirical data to define the location of the lattices and do not allow the vortex elements to move. In either case the induced velocity is calculated using the Biot-Savart law, which is a computationally expensive operation. In order to minimize the amount of computation, the trailing vortices are often approximated as a single or few tip vortices after 60° to 90° wake age and the shed vortices are kept up to 30° to 45° behind the rotor. The strength of the vortex lattices is calculated from the bound circulation on the blade, which is derived from the blade sectional lift. Other parameters for this vortex lattice method such as core models and releasing points are very difficult to determine.

Vortex particle method was also used to capture shed and trailed vorticity in the rotor wake [1.11]-[1.12]. Sometime the term vortex "blob" is introduced as collections of vortex particles. The vortex particles or blobs can also move with local velocity which is calculated again using the Biot-Savart law for every particle in the computational domain. Since a large number of particles (N) is needed to define the entire flow field the computational cost can be as high as N^2 operations although some techniques can be used to reduce this cost, e.g. Particle-Mesh (NlogN) and Fast Multipole (NlogN). The strength of vortex particles again can be determined from the bound circulation on the blade. Core models of this vortex particle method are well established, but the location of releasing points is still challenging to obtain.

Full CFD has also been considered for simulating the rotor wake [1.13]-[1.14]. This approach solves the Navier-Stokes equations for primitive variables (i.e. velocity, density, and pressure) in the flow field at all grid points in the entire domain. Normally, two sub domains are implemented in rotorcraft CFD modeling. One domain rotates with the blades and another non-

rotating domain is used in the background to capture the rotor wake. Interpolation between the two domains has to be performed at every time step. The rotating domain usually extends three to five chord lengths from the rotor surface, while the background grid extends three to five rotor radii from the surface. This method has the fidelity to capture boundary layer and 3-D effects near the root and tip of the blade very well. However, a very large number of grid points is necessary to simulate the vortex wake satisfactorily, since the cell dimensions inside the boundary layer can be as small as 1/10000 of the chord length and the cell dimensions in the vicinity of the tip vortices can be approximately 1/50 of the chord length. Grid adaptation is a necessity to properly distribute more grid points to the regions with high vorticity, and these regions usually move constantly throughout the field.

A rotor wake can also be modeled using VTM [1.15]. The vorticity transport equations, which are derived from conservation of momentum, are solved to determine the evolution of vortex parameters on a Cartesian grid. The maximum resolution of the grid typically used for this approach is about a quarter of the chord length. Similar to other vortex approaches, the induced velocity is calculated using the Biot-Savart law. A multi-level grid is introduced to reduce the computational cost. The initial strength of the vortex is obtained from 2D lifting line theory. This VTM approach can satisfactorily model the evolution of the rotor wake.

Overall traditional RANS solvers can predict the generation of vorticity very well, but often have difficulties in simulating the evolution of the vorticity field over a long period of time because of limitations due to numerical dissipation and regeneration/adaptation of the grid. On the other hand, the evolution of the vorticity field can be modeled satisfactorily using VTM or modern vortex particle method which are both based on the vorticity transport equations. In addition, the vortex particle method does not require grid adaptation, since there is a natural tendency of particles to cluster around regions with high vorticity. Therefore, a hybrid approach using a RANS solver near the surface to calculate the generation of vorticity and a Particle-based VTM (PVTM) to simulate the evolution of the far field wake flow offers a unique capability to capture the entire wing or rotor wake flow with high accuracy.

Recently, a new hybrid approach using fully coupled Reynolds-Averaged Navier-Stokes (RANS) and Particle-based Vorticity Transport Method (PVTM) solvers was introduced to simulate rotorcraft wake flow [1.16]. The approach divides the flow field into several regions and uses

appropriate flow solvers according to the dominant physical features of the flow in each region. The first region covers the flow field near aerodynamic surfaces (extending about one chord from the surfaces), where the flow features are dominated by the effects of boundary layer viscosity and the geometry of the airfoil and blade planform. The near body flow field is resolved using a 3D compressible RANS solver [1.17]. Outside of the RANS regions, the flow field is primarily dominated by the vortices being shed from the aerodynamic surfaces. This vortex-dominated flow region is simulated using a Particle-based Vorticity Transport Method (PVTM). The influence of this far field flow region is transferred to the RANS regions using the field velocity approach [1.17]. By modeling the far field with PVTM, the shed vorticity can remain well organized and in particular the tip vortices can maintain their compact and stable cores for a longer period of time than vortices simulated using conventional RANS/CFD. This approach is particularly suitable for rotorcraft applications where maintaining the correct velocity gradient in the vortex core is critical for acoustic and vibratory loads calculations, which depend greatly on the location, size, and strength of the vortex. A previous study showed that the methodology is viable, but did not illustrate quantitatively how well the approach predicted the near body flow field and associated vortex-dominated flow field [1.16].

1.2 Focus of the present research

Further development and validations of the fully coupled RANS/PVTM/CSD methodology are achieved in this study (Fig. 1.1). The development efforts include - (i) refining coupling methodology between RANS/PVTM, (ii) coupling the RANS/PVTM with Computational Structural Dynamics (CSD) code, (iii) implementing a diffusion model for PVTM, (iv) adding a vortex stretching model for PVTM, (v) implementing a dynamic memory model for PVTM to reduce memory usage. The coupled RANS/PVTM methodology is validated against several experimental data sets including - (a) a low aspect ratio fixed-wing wind tunnel test, and (b) a hover test for a lightly loaded rotor.

Chapter II

Coupled PVTM/RANS/CSD Methodology

2.1 Coupled RANS/PVTM methodology

In the present study, the entire flow field is divided into near and far fields, which are resolved using RANS and PVTM solvers, respectively. The RANS solver predicts the generation of the vorticity field near aerodynamic surfaces and releases the vorticity into the PVTM domain through a convection process at the boundary of the RANS domains. The PVTM solver determines the evolution of the entire far field vorticity after the vortex particles are released from the RANS domains. At every time step, the RANS domains provide vorticity information to PVTM, and PVTM provides current induced velocity information from all vortex particles in the far field to the near field RANS grids. A summary of the RANS and PVTM methodologies and the coupling process is provided in the following sections.

2.1.1 Near field analysis (RANS domain)

A RANS solver is used to calculate the generation of the vorticity field near the aerodynamic surfaces (wing or rotor blades), and in the present study the solver is based on a 3D RANS implementation described in Ref. [1.17]. The analysis solves the RANS Equations for primitive variables (i.e. ρ, V, and P) inside a 3D structured grid using a finite volume approach. This RANS domain defined by the grid usually extends to approximately one chord length away from the surface. The short distance to the boundary minimizes numerical dissipation of the generated vorticity field before reaching the boundary and releasing into the PVTM domain. The boundary conditions for this RANS domain are – (i) the induced velocity from the far field (PVTM and other disconnected RANS domains), (ii) the free stream density, and (iii) the non-reflective boundary condition (extrapolation of pressure from inside the RANS grid). In addition, the induced velocity from the far field (PVTM and other disconnected RANS domains) is included

as field velocity [1.17] to all of the grid points in the RANS domain to ensure accuracy and to speed up convergence of the coupling process.

For the fixed wing computation, only one RANS domain is used. The RANS grid extends to about one chord in all directions except behind the trailing edge, where it extends only to about a half chord length to minimize the dissipation of vorticity to be transferred into the PVTM domain. An example of the near body RANS grid for a fixed wing calculation is shown in Fig. 2.1a. The RANS grid has a dimension of 249×131×79 grid points.

The near field calculation with a RANS solver in the rotor simulation involves as many RANS domains as the number of blades in the rotor. All domains are disconnected from the other RANS domains. Figure 2.1b shows the RANS grid system required for a four bladed rotor simulation. The coverage of the grid points is similar to the RANS grid for the fixed wing case: 0.5c behind the trailing edge, and 1c in other directions. For each blade, the RANS grid has a dimension of 239×151×69 grid points. The influence of one blade to the other blades is calculated by - (i) converting the velocity field inside the RANS domain into a vorticity field, (ii) converting the vorticity field into a particle vortex field, and (iii) calculating the additional induced velocity from this near blade particle vortex field to other blades.

2.1.2 Far field analysis (PVTM domain)

Outside of the near surface RANS domains, the flow field is represented by collections of three-dimensional vortex particles similar to those presented in Ref. [2.1]. Each vortex particle has two vector quantities, location and strength, associated with it. The strength of the vortex is a volume integration of the vorticity field around the particle, and the evolution of the strength is governed by the vorticity transport equations:

$$\int \frac{d\omega}{dt} dV_i = \int [\omega \cdot \nabla u] dV_i + \int \left[\nu \nabla^2 \omega\right] dV_i + S_i^r \tag{2.1}$$

$$\alpha = \int \omega \, dV_i \tag{2.2}$$

$$\frac{d\alpha}{dt} = \alpha \cdot \nabla u + \dot{\alpha}_d + \dot{\alpha}_r \tag{2.3}$$

$$\frac{dx}{dt} = u$$

where u is the local flow velocity, ω is vorticity, ν is kinematic viscosity, and $\vec{S}_i$ is the vorticity released from the RANS domain into the differential volume dV_i. Using the vortex particle strength definition in Eq. (2.2), Eq. (2.1) becomes the vortex particle governing equation (Eq. 2.3), where α is the strength of a vortex particle in dV_i, $\alpha \cdot \nabla u$ is the vortex stretching term which cannot incur reduction or increase in the vorticity strength, $|\alpha|$ [2.2], $\dot{\alpha}_d$ is the rate of change of tge vortex particle strength due to diffusion, $\dot{\alpha}_r$ is the rate of release of vortex particle strength from RANS domains, and x is the location of the vortex particle. The differential volume, dV_i, represents the PVTM cell resolution, and a 3D Cartesian volume is chosen for convenience. Representations of the multi-level PVTM computational domains are presented in Fig. 2.2 for the fixed wing and the rotor cases. To reduce computational cost, only one vortex particle is allowed in a PVTM cell. When two or more particles are inside the same PVTM computational cell, they are merged into one particle as graphically shown in Fig. 2.3b, with the new strength being the sum of the strength of all particles, and the location being the strength weighted centroid of all the particles. The location of each vortex particle is governed by the local velocity induced from - (i) all vortex particles in the far field, (ii) vortex particles representing vorticity in the RANS domains. The detailed derivation of vortex particle evolution equations are given in Chapter III, while the derivation of the released vortex from RANS domains is given below.

2.1.3 Coupling RANS/PVTM domains

In order to couple the RANS and PVTM domains, proper information is passed between them at every time step. The information passing from RANS domains to the PVTM domain is the vorticity field for calculating - (i) the vortex particles released from RANS domains to PVTM domain, (ii) the induced velocity from RANS domains. The information passing from PVTM domain to RANS domains is the vortex particle field which represents the entire far field vorticity that is used to calculate the far field induced velocity. Additional information transfer (vortex particles representation of the RANS vorticity field) between the RANS domains is needed for calculating the induced velocity from one RANS domain to the other RANS domains.

2.1.3.1 Vortex particles released from RANS domains to PVTM domain

The vorticity released from RANS domains into the PVTM domain, α_r, is derived from the convection of the vorticity field from the boundary of the RANS domains. For each RANS cell

that is on the boundary, the vorticity convected from the RANS domain into the PVTM domain is defined as follows:

$$\alpha_r = \int \omega A \cdot (u \cdot \hat{n})\, dt \tag{2.4}$$

$$X_r = X_{mid} + \int u\, dt$$

where α_r is the strength of the released particle, X_r is the location of the released particle, A is area of the outer boundary, $\hat{n}$ is the outward normal vector and X_{mid} is the mid-point of the area A. In addition to these convectively released vortex particles, the moving RANS grid also releases vortex particles due to the movement of the grid boundary as follows:

$$\alpha_r = \int \omega A u\, dt = \tfrac{1}{2}\left(\omega^k + \omega^{k-1}\right) A \left| X_{mid}^k - X_{mid}^{k-1} \right| \tag{2.5}$$

$$X_r = \tfrac{1}{2}\left(X_{mid}^k + X_{mid}^{k-1}\right)$$

After the release, the vortex particles in the same PVTM computational cell are merged to reduce the computational cost. Graphical representation of the vorticity releasing process from RANS domain to PVTM domain is presented in Fig. 2.4.

2.1.3.2 Induced velocity from RANS domains to PVTM domain

The aerodynamic influence from RANS domains to the PVTM domain is taken into account by including the induced velocity from vorticity in the RANS domains to calculate the particle velocity in Eq. (2.3). The continuous vorticity field in the RANS domains is processed into a particle vortex field representing the RANS domains. These vortex particles representing the RANS domains are included in calculation of the local flow velocity for vortex evolution equations. Detailed derivation of the induced velocity calculation is given in Chapter III.

2.1.3.3 Induced velocity from PVTM domain to RANS domains

The far field induced velocity from the PVTM domain is included to the near field RANS calculation as field velocity [1.17]. The induced velocity is added to all of the grid points in the RANS domain to ensure accuracy and to speed up convergence of the coupling process. To reduce the computational effort, the induced velocity from the PVTM domain is calculated on an

interpolation grid and the induced velocity on all RANS grid points are calculated from 3D linear interpolation from the induced velocities on the interpolation grid (see Fig. 2.5) .

2.1.3.4 Induced velocity from a RANS domain to other RANS domains

When more than one RANS domains (not connected to each other) are used, the influence between these domains are accounted for by calculating the induced velocity from one RANS domain to the other RANS domains. Again, the continuous vorticity field in a RANS domain is converted to a vortex particle field that represents the vorticity in the RANS domain. The induced velocity from this vortex particle field is included in the calculation of the induced velocity for other RANS domains.

2.2 Coupling RANS/PVTM with CSD

For the rotor case, a loose coupled trim methodology is used to couple a CSD code (CAMRAD II [2.3]) with the RANS/PVTM analysis. The comprehensive CSD code, CAMRAD II, handles the vehicle trim calculation and performs a structural analysis for the blade motion in response to the RANS/PVTM aerodynamic loading. The loose coupled trim methodology presented in Ref. [2.4] is adopted for coupling CAMRAD II and RANS/PVTM and is summarized in Fig. 2.6.

The calculations for the vehicle trim and the structural analyses are performed by CAMRAD II with the aerodynamic loading from RANS/PVTM analysis in a once-per-revolution basis (a more frequent information transfer is also possible). The pressure and shear forces on the blades (from the near blade RANS domains) are integrated to provide the blade sectional load (M^2C_L, M^2C_D, and M^2C_M) at various collocation points along the blade quarter chord line for the CSD analysis. The CSD code uses this blade sectional loading to retrim the rotor and provides the RANS/PVTM analysis a new blade motion (6 DOFs) at the collocation points. The new blade motion is used in the RANS/PVTM analysis to calculate the new blade aerodynamic loadings. This coupled trim process continues until the following variables are converged: (i) trim parameters, (ii) blade motion, and (iii) blade loading.

Chapter III

PVTM Methodology

3.1 Vorticity Transport Equations and solution methodology

Vorticity transport equations (derived from taking the curl of the momentum equations from Navier-Stokes Eqs.) can be expressed in several frames of reference - (i) Eulerian frame [1.15] or (ii) Lagragian frame [2.1]. In the current study, the Lagragian frame implementation is adopted for convenience since it offers gridless capability (no flow calculations at the grid points). The approach discretized the vorticity field into a vortex particle field, and each vortex particle carries a local vorticity field around it. The movement of these vortex particles represents the transportation of vorticity without any loss in vorticity strength. Again, the vorticity transport Eq. (2.3) is presented here in a slightly different form:

$$\alpha^{k+1} = \alpha^{k} + \int \left(\alpha^{k} \cdot \nabla u\right) dt + \alpha_{d} + \alpha_{r} \tag{3.1a}$$

$$x^{k+1} = x^{k} + \int u \; dt \tag{3.1b}$$

where superscript k represents a time step index, $\alpha = \int \omega \, dV$, u is the local velocity, α_d is the change in vortex particle strength due to the diffusion effect, α_r is the strength of the vortex particle released from the RANS domains (Eqs. 2.4-2.5), and x is the location of the vortex particle. Equation 3.1a governs the change in the strength of the vortex particle in a particular PVTM cell, while the location of the particle is calculated using Eq. 3.1b. The detailed definition of each term in Eq. 3.1 can be found in Section 2.1.2.

Equations 3.1 are solved using explicit integration schemes based on Runge-Kutta (RK) integration method with 4^{th} or 6^{th} order accuracy in time [3.1]. Equation 3.1b is solved directly with the RK scheme with adaptive time step (see Appendix A). When solving Eq. 3.1a, the

terms α_d and α_r are calculated in separate steps and included at the end of the time step, thus without these terms, Eq. 3.1a reduces to:

$$\alpha^{k+1} = (I + A_\varepsilon)\alpha^k \tag{3.2}$$

$$A_\varepsilon = \int \nabla u \, dt$$

where A_ε is the strain tensor of the local velocity field. It should be noted that the summation of the eigenvalues of A_ε is zero (continuity condition). There is also one eigenvalue of A_ε that is zero, λ_0, representing a solution that conserves the total vorticity ($|\alpha^{k+1}| = |\alpha^k|$). Other eigenvalues are associated with non-physical increase or decrease in vorticity strength. Thus, the only solution that conserves vorticity must have the strength vector oriented in the direction of the eigenvector associated with λ_0. Numerically, the solution of Eq. 3.2 represents a reorientation or 3D-rotation of the vortex strength vector, α^k, into the direction of the eigenvector associated with λ_0. The derivation of this eigenvector is given in Appendix B for a system of two vortex particles. Due to the fact that the strain tensor is a summation of the stain field induced from all vortex particles in the entire field, a superposition method can be used to determine the reorientation of the strength vector of a vortex particle in response to other vortex particles in the field.

3.2 Induced velocity calculation and computational scheme

Calculation of induced velocity involves summation of the induced velocity from all vortex particles in the flow field (far field PVTM domain and near field RANS domains). The induced velocity at an arbitrary location X from N vortex particles can be calculated using the modified Biot-Savart law [2.1]:

$$u(X) = \sum_{i=1}^{N} -\frac{1}{4\pi} \frac{(X - x_i) \times \alpha_i}{\left(|X - x_i|^2 + \delta^2\right)^{3/2}} \tag{3.3}$$

where δ is the desingularized parameter which is introduced to avoid singularity of the induce velocity when $X = x_i$. The value of δ is set to be $0.1 \times d$. The numerical effect of this desingularized parameter is similar to using a vortex core radius of δ.

The calculation of the induced velocity is very computationally expensive. In order to reduce the number of induced velocity calculations within the RK integration substep, the induced velocity is calculated on tetrahedral basis points (Fig. 3.1) and a trilinear interpolation is used to determine the induced velocity within the RK substep. The distance from the particle to the all vertices of the tetrahedral is set to 0.5% of the PVTM cell size. The interpolation is based on the first order Taylor expansion of the quantity u about the center of the tetrahedral. The derivatives of the quantity u are calculated using Eq. (3.4)

$$\begin{aligned}\frac{\partial u}{\partial x} &= \frac{1}{4}\sum_{i=1}^{4}\frac{u_i - u_o}{x_i - x_o} \\ \frac{\partial u}{\partial y} &= \frac{1}{4}\sum_{i=1}^{4}\frac{u_i - u_o}{y_i - y_o} \\ \frac{\partial u}{\partial z} &= \frac{1}{4}\sum_{i=1}^{4}\frac{u_i - u_o}{z_i - z_o}\end{aligned} \tag{3.4}$$

where the subscript i represents the i^{th} vertex of the tetrahedral, and the subscript o represents the values at the center of the tetrahedral (u_o is the average value of u_1, u_2, u_3, u_4). The interpolated value, $u'(x',y',z')$, is obtained following Eq. (3.5)

$$u' = u_o + \begin{bmatrix}\frac{\partial u}{\partial x} & \frac{\partial u}{\partial y} & \frac{\partial u}{\partial z}\end{bmatrix}\begin{bmatrix}x' - x_o \\ y' - y_o \\ z' - z_o\end{bmatrix} \tag{3.5}$$

3.3 Local strain tensor calculation

The calculation of the local strain tensor is straightforward since the strain rate tensor is already calculated from Eq. (3.4) for the velocity interpolation. A first order time integration scheme is used to determine the strain tensor in Eq. (3.2b).

3.4 Reorientation of vortex strength vector

The strength vector of the vortex particles is reoriented or rotated toward the direction of the eigenvector associated with λ_0 for a vorticity solution that conserves the total vorticity. It is shown in Appendix B that the reorientation of the vortex strength vector can be achieved by using a vortex stretching term in the following form:

$$\alpha^P \cdot \nabla u = \sum_i \frac{\eta}{4\pi} \frac{(\alpha^P \times \alpha_i) \times \alpha^P}{\left(\left|x^P - x_i\right|^2 + \delta^2\right)^{3/2}} \tag{3.6}$$

where η dictates how fast the reorientation of the strength vector occurs. An adjustment in the velocity calculation is required to mitigate the numerical error accumulation due to the explicit time integration scheme (see Appendix B).

3.5 Diffusion model for PVTM

3.5.1 Diffusion model using vortex redistribution

For vortex method, the effect of diffusion process can be simulated using a vortex redistribution method. In this study, the diffusion effect is simulated by splitting a vortex particle into five smaller particles and redistributing the original vortex strength to the new particles. The locations of these five particles are defined by the vertices of a randomly oriented tetrahedral and its center (see Fig. 3.2). The distance from the original particle (center of the tetrahedral) to the locations of the new particles (vertices of the tetrahedral) is equal to $d/2$, where d is PVTM cell size). The redistribution factors are calculated using the Vorticity Redistribution Method [3.2]-[3.3], which is outlined below. As outlined in Section 3.1, the diffusion step is solved separately from the vortex convection step. Without the vortex stretching and the source terms, the Vorticity Transport Eqs. can be written in a non-dimensional form (Eq. 3.7), the effective diffusion distance, h, is defined in Eq. (3.8), where Δt_d is the non-dimensional diffusion time step. This diffusion time step can be different from a convection time step. The redistribution method simulates the diffusion process within the effective diffusion distance, h, as presented in Eq. (3.9) by splitting a vortex particle into five smaller particles.

$$\frac{\partial \omega}{\partial t} = \frac{1}{\mathrm{Re}} \nabla^2 \omega \tag{3.7}$$

$$h = \sqrt{\frac{\Delta t_d}{\mathrm{Re}}} \tag{3.8}$$

$$\omega_i(x,t) = \Gamma_i \phi(x - x_i) \tag{3.9a}$$

$$\omega_i(x,t+\Delta t) = \sum_{j=1}^{5} f_{ij} \Gamma_i \phi(x - x_j) \tag{3.9b}$$

The redistribution factors, f_{ij}, are determined by using either Fourier transforms [3.2] or series expansion [3.3]. The resulting system of equations with first order of accuracy is given in Eqs. (3.10), where $\hat{x}_{ij} = (x_j - x_i)/h$, $\hat{y}_{ij} = (y_j - y_i)/h$, and $\hat{z}_{ij} = (z_j - z_i)/h$.

$$\begin{aligned}
&\sum_j f_{ij} = 1 \\
&\sum_j f_{ij}\hat{x}_{ij} = \sum_j f_{ij}\hat{y}_{ij} = \sum_j f_{ij}\hat{z}_{ij} = 0 \\
&\sum_j f_{ij}\hat{x}_{ij}\hat{y}_{ij} = \sum_j f_{ij}\hat{y}_{ij}\hat{z}_{ij} = \sum_j f_{ij}\hat{x}_{ij}\hat{z}_{ij} = 0 \\
&\sum_j f_{ij}\hat{x}_{ij}^2 = \sum_j f_{ij}\hat{y}_{ij}^2 = \sum_j f_{ij}\hat{z}_{ij}^2 = 2
\end{aligned} \tag{3.10}$$

The system of linear equations, Eq. (3.10), is solved to obtain the redistribution factors, f_{ij}. A higher order of accuracy solutions can be achieved by solving additional expansion equations similar to Eqs. (3.10) [3.3]. Once the diffusion factors are determined, each particle is split based on Eq. (3.11).

$$\alpha_d = \sum_{j=1}^{5} f_j \alpha^k \tag{3.11}$$

3.5.2 Solving the Convection-Diffusion steps

Since the convection and diffusion steps are solved separately, the convection and diffusion time steps need not necessarily to be the same. In this study, a diffusion step is performed every 20 convection steps because the high Reynolds number makes the effective diffusion distance, h, very small compared to the PVTM cell size. If the diffusion step is carried out with the same time step as the convection step, the splitting of the particle due to diffusion effect will be repealed with the merging of the vortex particles (introduced to reduce the computational cost).

3.6 Vortex stretching model for PVTM

In addition to the reorientation of the vortex strength vector, the vortex stretching term in the Vorticity transport equations involves a physical stretching or thinning of the vorticity field. A stretching of vortex elements normally occurs when the vortex elements are subjected to a strain field. The direction of the stretch is governed by the invariant subspace (usually referred to as eigenvector) of the strain field, while the amount of stretching is governed by the principal strain of the strain field [3.4]. In order to simulate the stretching phenomenon of a vortex element, a scalar variable is added to each vortex element to represent a characteristic length, L_c, of the

element (L_c is normalized using PVTM cell size, d). Thus each vortex element has two vectors and one scalar quantity associated with it: (i) vortex strength vector, α, (ii) vortex location vector, x, and (ii) characteristic length, L_c. This vortex element is subjected to a velocity field, u. The strain rate field, ∇u, can be found by differentiating the velocity field with respect to spatial variables (see also Section 3.3). The principal strain of the characteristic length is found through Eq. 3.12:

$$\hat{\varepsilon} = \int \max\left[eig\left(\tfrac{1}{2}\nabla u + \tfrac{1}{2}\nabla u^T\right)\right] dt \tag{3.12}$$

Thus the equation governing the characteristic length is:

$$L_c^{k+1} = L_c^k\left(1.0 + \hat{\varepsilon}\right) \tag{3.13}$$

where k is the time step index. The initial value of the characteristic length is d, and if the characteristic length of a vortex element is greater than $2d$, then the vortex element is split into two elements along the principle strain axis. The distance between the split elements is the PVTM cell size, d. After the split, the characteristic length of the split elements is reset. This stretching process is shown graphically in Fig. 3.3.

3.7 Memory models for PVTM

The implementation of the PVTM code uses either static or dynamic memory models as shown in Fig. 3.4. The static memory model offers fast and direct access to vortex particle information since the memory for all PVTM cells is allocated a priori and each cell is associated with a specific PVTM volume in the flow field. However, the static memory model suffers from inefficient usage of the memory because there are many empty cells in the PVTM domain. A dynamic memory model using a linked-list access is introduced to improve the efficiency of memory usage, but access to vorticity information in this dynamic memory model is very slow compared to the static memory model. The static memory PVTM model is referred to in the result sections as “Static PVTM”, while the dynamic memory PVTM model is referred to as “Dynamic PVTM”.

Chapter IV

RANS/PVTM Results: Fixed-Wing Case

In this chapter, the coupled RANS/PVTM methodology is applied to a fixed-wing case and the results are validated against wind tunnel test data. Comparisons with measured pressure distribution, loadings, and vortex parameters, and the corresponding results from the full RANS and coupled RANS/PVTM simulations are presented for a semi-span NACA 0015 wing. Although full RANS calculations are provided for reference, these full RANS calculations do not take advantage of higher order or refinement techniques, so they do not represent the state of the art in wake modeling with RANS CFD.

4.1 Modeling Experimental Test Conditions

A comprehensive experiment to measure the detailed progression of the tip vortex from a semi-span NACA 0015 wing [4.1], conducted at the NASA Ames 7- by 10-Foot Subsonic Wind Tunnel, is used as the reference data to validate the results from the RANS/PVTM simulations. The experimental setup is shown in Fig. 4.1. The experiment used a pressure-instrumented, untwisted semi-span NACA 0015 wing with a square tip (meaning the end is flat and perpendicular to the span axis). A round end cap was installed for some conditions to change the tip geometry of the wing from square tip to rounded tip. The experiments were conducted for a small range of Reynolds numbers between 1×10^6 and 3×10^6. Velocity profiles across the tip vortex were measured at various downstream locations up to six chords behind the wing using a two-component laser velocimeter. The data provided by this test include *(i)* the chordwise pressure distribution along several span locations; *(ii)* the velocity, location, and core size of the tip vortex; *(iii)* integrated sectional lift, drag, and moment coefficients at various span locations.

The experimental configuration and condition described in Ref. [4.1] is used to develop computational models of the semi-span NACA 0015 wing. The rectangular wing has a constant

and untwisted NACA 0015 airfoil along the span with a full-span aspect ratio of 6.6. The wing was mounted on a vertical supporting end plate that fitted one foot away from the side wall of the tunnel. This end plate prevents the formation of the trailing vortex near the mounting point and effectively creates an infinite wing (2D) boundary condition at the mounting point. Several angles of attack were tested in the experiment. For the current study, only one angle of attack of 12° is simulated. An additional 0.51° is added to the angle of attack in the simulations as a correction for the closed-tunnel wall effect [4.1]. The full effects of the wind tunnel walls are not fully accounted for in this study except near the root of the wing where only the no cross-flow condition is applied. The free-stream velocity corresponds to a Mach number of 0.13 and Reynolds number of 1.5×10^6.

4.2 Full RANS Analysis

The baseline or full RANS simulation results in the present study are obtained using the TURNS 3D compressible solver [1.17]. The analysis solves the RANS equations for primitive variables ρ, ρV, ρE inside a 3D structured grid using a finite volume approach. The grid used in the calculation for the square tip wing is presented in Fig. 4.2 with the dimension of 399×131×97 grid points. The grid extends to about six chords in all directions from the wing surface, and grid points are distributed a priori and mostly concentrated in regions with high velocity gradient such as near the leading edge, boundary layer, tip vortex, and vortex sheet. The boundary condition at the root of the wing is set to be extrapolated from flow parameters inside the RANS domain, simulating the infinite wing (2D) boundary condition to match the experiment. The vorticity profile calculated using this full RANS analysis is shown in Fig. 4.3. It is seen that the tip vortex and vortex sheet are diffused very quickly before reaching the boundary of the RANS domain (six chords behind the wing). The rapid diffusion of the tip vortex is caused primarily by numerical diffusion, insufficient grid resolution (high velocity gradient regions), and the use of low order scheme. An improvement in the results may be obtained by using better grid resolution, grid adaptation scheme near high gradient region, and high order schemes.

4.3 Coupled RANS/PVTM Analysis

In the coupled RANS/PVTM analysis, the flow field is divided into a near-body grid and a far field region. The flow field in the near-body grid is resolved using the same 3D compressible

RANS solver and boundary conditions as described in the previous section, but the domain is much smaller. The RANS domain extends to about one chord length in all directions except behind the trailing edge, where it extends only to about a half chord length, see Fig. 4.4. The small extent behind the trailing edge minimizes the dissipation of vorticity to be transferred into the PVTM domain. This small RANS grid has a dimension of 249×131×79 grid points. The same 2D boundary condition at the wing root is used. In addition, the induced velocity from the vortex particles in the far field is included in the RANS calculation as field velocity [1.17]. The vorticity field resulting from this coupled RANS/PVTM calculation is presented in Fig. 4.5, and the vorticity isosurface of the vorticity field in the PVTM domain is shown in Fig. 4.6. These results demonstrate that the coupled RANS/PVTM methodology preserves the vorticity in the far field qualitatively quite well.

4.4 Tip Vortex Core Parameter Identification

The identification of the tip vortex core parameters, namely size and location, is adopted from the procedure presented in Ref. [4.1]. In the experiment, an approximate location of the tip vortex at some distance behind the trailing edge was measured using a vortex meter. Then a laser doppler velocimeter was used to measure the swirl velocity across the vortex core in the spanwise direction. The vortex core size reported is the distance between the locations of the maximum and minimum swirl velocity across the core. The precise location of the core was determined to be the mid-point between the minimum and maximum swirl velocity.

Similar methodologies are employed for the computational results. To identify the vortex core parameters inside a RANS domain, the approximate location of the tip vortex core is determined by searching for the maximum amplitude of vorticity in a given plane behind the trailing edge. Once this is known, the swirl velocity across the vortex core is calculated by linear interpolation, and then the core size and precise location of the core are calculated in the same manner as in the experiment.

A slightly different procedure is used for identifying the vortex core parameters for the PVTM domain, since the PVTM analysis does not calculate the velocity field directly. At the desired distance behind the trailing edge, properly located virtual velocity measurement planes are created to record the induced velocity from the vortex particle field. These measurement planes

are shown in Fig. 4.5 at a distance 1, 2, 4, and 6 chords behind the wing. The induced velocity field from the vortex particles is calculated in each measurement plane, similar to particle image velocimetry measurements in the experiment. The velocity fields are processed into vorticity with the strength vector perpendicular to the measurement plane. The vorticity field is searched to find the location of the maximum vorticity in order to obtain the location of the vortex core. The swirl velocity can be extracted directly from the measurement plane to obtain the core size in the same way as for the measurement and for the RANS-calculated velocity field. For the PVTM vortex parameter identification, 200 samples of the core size and swirl velocity field are averaged to obtain the reporting vortex parameters. This is necessary because the induced velocities from the particles are highly dependent on the proximity of the particle to the virtual measurement planes where the velocity is being calculated. The averaging scheme reduces the fluctuation of the core size and swirl velocity results due to the movement of the vortex particles into and out of the virtual measurement planes.

4.5 Result comparison: Experiment, full RANS, RANS/PVTM

Comparisons of the experimental data from Ref. [4.1] and the results obtained using the full RANS and the RANS/PVTM calculations are presented based on the test metric shown in Table 4.1. Only the static PVTM is used for the calculation of the fixed wing cases. This case metric is developed to provide a comprehensive representation of RANS/PVTM results that show the sensitivity of the RANS/PVTM results on a number of parameters including time step size (Δt^*), RANS grid boundary, PVTM cell resolution, and PVTM redistribution methods.

Computational efficiency (time step size and number of vortex elements) is presented in Table 4.2. All calculations are obtained using NIA high performance computing clusters. Post-processing of the results for plotting purposes is performed on a PC workstation using MATLAB. Each of the calculation presented in this report is carried out using parallel computing based on MPI with eight CPUs. For a comparison, the computational time and parameters for the full RANS calculation using four CPUs is given in Table 4.3.

The vorticity isosurface results from the coupled RANS/PVTM calculations are presented in Fig. 4.7 for the different cases in the test matric. The comparison of full RANS, RANS/PVTM results and the experimental data from Ref. [4.1] are presented in Figs 4.8-4.14, which shows the vorticity isosurface of the tip vortex; the chordwise pressure distribution; spanwise

distribution of sectional lift, drag and pitching moment; and tip vortex parameters including core size, vertical and spanwise locations, and swirl velocity. Overall the results from full RANS and RANS/PVTM calculations yield good correlation with pressure distribution data. The vortex parameters from the full RANS calculation do not correlate well with the data, while the vortex parameters from RANS/PVTM calculations correlate better with the experimental data.

4.5.1 The effects of RANS/PVTM parameters on vorticity field

The RANS/PVTM results in Figure 4.7 show vorticity isosurface and the location of vortex particles on three planes behind the wing using various combinations of RANS/PVTM parameters. The parameters include – (i) location of RANS grid boundary, (ii) time step size, (iii) PVTM cell resolution, and (iv) vortex diffusion model. The parameter variations and the case numbering are given in Table 4.2. It is seen from Fig. 4.7 that the effects of these parameters on the vorticity field in the PVTM domain qualitatively is negligible, since the results from all of the cases produce a very similar vorticity field behind the wing.

4.5.2 Pressure distribution

The comparisons of chordwise pressure distribution at four span locations are presented in Fig. 4.8. The pressure distribution from all of the cases from RANS/PVTM calculations is similar, and only the results from Case 7 are shown. Overall, the pressure distribution compares well with the experimental data. Only the peak pressure near the leading edge is not resolved well from the RANS and RANS/PVTM results. The potential sources of this difference include: RANS grid resolution near the peak pressure, the use of low order turbulent modeling and flux limiter.

4.5.3 Wing sectional loading

Figure 4.9 shows the wing sectional loading comparison between the experimental data, full RANS and RANS/PVTM (Case 7) results. Only the results from Case 7 are shown since the differences in the RANS/PVTM results are negligible. The comparisons in sectional lift, C_L, are: very good near the wing tip, good near the root of the wing. The sectional drag, C_D, correlation for RANS/PVTM is very good throughout the span. The sectional moment, C_M, comparison is

very good near the tip, but is poor inboard, likely due to the differences in peak pressure of the leading edge compared to the experiment.

4.5.4 Tip vortex core size

The comparison of the tip vortex core size is presented in Figure 4.10. The tip vortex core size predicted by the RANS/PVTM method right at the release plane (at the boundary of the RANS grid, about half a chord behind the trailing edge) is about 30% larger than that of the test data. Then the core size initially increases (between 1-2c behind the wing) and then reduces and the core size at six chords behind the wing is about 40% larger than the core size from the data. Comparing the PVTM results from all of the cases, the vortex core size from Case 5 is closest to the experimental data. The better correlation is probably due to the proper combination of PVTM parameters (small time step, smaller RANS grid in downstream direction, and the PVTM cell size that is similar to the data). It should be noted that this tip vortex core size is not equal to the PVTM cell size, for example Case 5 PVTM cell size and the resulting core size are 0.1c and 0.14c, respectively. The core size predicted from the full RANS calculation increases rapidly and the core size at six chords behind the wing is more than 125% larger than the test data. This rapid growth in core size in the full RANS calculation is the result of numerical dissipation and the tip vortex moving away from the dense grid region.

4.5.5 Tip vortex location

The vertical and spanwise locations of the tip vortex are shown in Figs 4.11- 4.12, respectively. Overall, the correlation of the spanwise location from RANS/PVTM is very good. The comparison of the vertical location is somewhat depending on the RANS/PVTM parameters. It is seen that the RANS/PVTM results from Case 4 give the best correlation for the tip vortex vertical location. It should be noted that some of the PVTM vortex vertical location results have sporadic movement of the tip vortex between one and two chord length behind the trailing edge. This is likely caused by misidentification of the vortex identification routine. For the tip vortex spanwise location, the results from Case 5 give the best correlation (but the vertical location correlation for Case 5 is not as good).

4.5.6 Tip vortex swirl velocity

Comparisons of the tip vortex swirl velocity at four and six chords behind the wing are given in Figs. 4.13-4.14, respectively. Overall, the RANS/PVTM method predicts the swirl velocity outside the vortex core very well, but the comparison of the peak vortex velocity to the test data is fair. The peak velocity prediction is about 33% less than that of the test data at four and six chords behind the wing. The correlation of the velocity gradient inside vortex core at both four and six chords for the RANS/PVTM is better than that of the full RANS results. This is due to the fact that the RANS/PVTM approach preserves the vorticity better than the full RANS approach.

Chapter V

Coupled RANS/PVTM/CSD Results: Rotary Wing Case

In this chapter, the RANS/PVTM methodology is coupled to a CSD code to analyze a rotary wing case and the results are compared with hover test data. The following parameters are compared with the experimental data: rotor loading, vortex parameters (core size, location, trajectory, and swirl velocity). As a reference, a free wake hover calculation using CAMRAD II is included in some of the comparisons.

5.1 Experimental test description

An experiment to measure the detailed evolution of the rotor tip vortex in hover condition was conducted at the DLR Institute of Flight Systems in Braunschweig, Germany [5.1]. The test was performed in a limited and enclosed space (rotor preparation hall), thus the rotor was operating in both ground effect and recirculation flow (see Fig. 5.1). In the current study, the effects of these complex flow conditions are not simulated thus the rotor system is assumed to operate in an unconfined area. The rotor system used in this Hover Tip Vortex Structure Test (HOTIS) is the same as in the HART II test [5.2]. Summary of the rotor and blade properties is given in Table 5.1. The flow velocity was measured using a stereoscopic particle image velocimetry (3D-PIV) system.

5.2 RANS/PVTM rotor model

The RANS/PVTM rotor model is developed using the HART II blade properties [5.2]. Four disconnected RANS domains are used to model the four bladed rotor system (see Fig. 2.1). Each RANS domain has 239×151×69 grid points (Fig. 5.2), and the grid points extend to about a half chord down stream and about one chord in other directions. For each RANS domain, the motion of each grid point is governed by the motion (three rotational and three translational deformations) of the quarter chord line of each blade, calculated from the CSD analysis. The

PVTM domain is a multi-level (six levels) domain with coarsening cell size away from the rotor (a representative PVTM domain with 2 levels is shown in Fig. 2.2b). The finest resolution for the PVTM cell is $d = 0.2c$, and the resolution for the PVTM cell size is defined by $d \times 2^{(L-1)}$, where L is the PVTM level.

5.3 CSD rotor model

The structural model of the rotor is based on CAMRAD II [2.3] and is provided by NASA Langley researchers. The CSD model solves multi-body dynamics equations using Finite Element representation of the rotor system. Each blade is modeled using five structural elements, representing the deformation of the quarter chord line. The rotor trim is also handled using CAMRAD II. As a reference, a fully coupled trimmed calculation using CAMRAD II with free wake is preformed (five revolutions of the rotor wake is retained for this free wake calculation).

5.4 RANS/PVTM results: untrimmed

Using a prescribed blade motion (blade pitch angle at $0.75R$ of 10°), the results from the RANS/PVTM (static memory model) approach is presented in Figs. 5.3-5.4 with three rotor revolutions of PVTM wake. To initialize the RANS variables, the simulation starts with only RANS simulation of the four-bladed rotor without releasing any PVTM wake for a quarter revolution (see Fig. 5.3). Without the PVTM wake and associated induced inflow, it is seen that the rotor thrust coefficient, C_T, increases drastically to about two times the thrust of the rotor with the PVTM wake. After the initial ¼ revolution, the simulation starts releasing PVTM wake. With the induced inflow from the PVTM wake, the rotor thrust rapidly decreases over the first revolution and slowly increases in the second and third revolution. The rotor torque, C_Q, is almost constant over the initial RANS startup and the first three revolutions with PVTM wake. The vorticity isosurface after three revolutions of the PVTM wake is shown in Fig. 5.4. It is seen that the startup wake (the first two revs.) is combined into a super-vortex below the rotor, and the strength of the tip vortex of any blade is preserved well before combining with the super-vortex. This shows a potential of RANS/PVTM approach to maintain the strength and compactness of tip vortices over one rotor revolution.

5.5 CSD/RANS/PVTM results: coupled trimmed

Fully coupled trim CSD/RANS/PVTM results are presented in the section. The information transfer between CSD and RANS/PVTM modules occurs once every rotor revolution (loose coupling). As a reference, CAMRAD II (with five free wake revolutions), CII-FW, results are included in some of the comparisons. The following results are provided - (i) trim convergence, (ii) vorticity field, (iii) tip vortex swirl velocity, and (iv) tip vortex location and trajectory.

5.5.1 Trim convergence

Using the static PVTM model, the convergence of the trim parameter (θ_{75}) is presented in Fig. 5.5. The results include 17 resolutions of PVTM wake and involve 11 coupled trim loops. The first eight revs. of RANS/PVTM simulation is completed without retrimming to obtain a reasonable initial condition for the rotor wake system. The trim parameter, θ_{75}, from the coupled CSD/RANS/PVTM is about 1° higher than the DLR data and about 0.3° higher than the result from CII-FW. This may be because the analyses do not model the ground and recirculation effects. Figure 5.6 shows the variations in individual blade and rotor loading of the coupled results. The rotor thrust, C_T, (individual blade - Fig. 5.6a; and rotor system – Fig. 5.6b) from the coupled trim results converges to the thrust condition of the HOTIS test. However, the rotor torque, C_Q, from the coupled result is 42.6% higher than the CII-FW result and is 63.2% higher than DLR data (CII-FW torque is 14.4% higher than DLR data). This higher torque may be caused by the following factors: higher θ_{75}, not modeling the ground and recirculation effects, and grid resolution near the blade surface to capture friction forces.

The comparison of the sectional blade loading from the coupling iterations between CFD (RANS/PVTM) and CSD modules is presented in Fig. 5.7. Results from CII-FW and CII-LI (linear inflow model) are also included as references. It is observed that the blade sectional loadings (M^2C_N, M^2C_C, and M^2C_M) are converged after about nine loose coupling iterations. Comparison of the sectional normal force with CII-FW illustrates that the coupled results yield 40-60% higher normal force near the tip of the blade ($0.95R$). This may be due to the differences in tip vortex parameter such as velocity profile and core size between the free-wake analysis and the PVTM approach. The blade sectional drag is much higher for the coupled results than the CII-FW result. Again, the factors that contribute to the higher torque value also affect the blade sectional drag. Blade sectional moments from the coupled results compared well with CII-FW result for the inboard section of the blade (r/R= 0.3-0.7).

The convergence of the "delta load" during the CSD-CFD coupling iterations is given in Fig. 5.8. It is seen that all of the delta loadings ($\Delta C_N M^2$, $\Delta C_D M^2$, and $\Delta C_M M^2$) are converged after about nine loose coupling iterations. The changes in delta loading are large in the very first coupling iterations and are reducing during subsequent iterations, and the changes are negligible during the last coupling iteration.

5.5.2 Vorticity field

With the coupled RANS/PVTM wake (static PVTM model) and CSD loose coupling, the vorticity field is shown in Fig. 5.9a. In addition to the vorticity isosurface showing the location of the tip vortex, Fig. 5.9a also shows virtual velocity measurement planes that rotate with the rotor for identifying tip vortex parameters (at 10, 20, 30,…, 150° wake ages). The tip vortex parameter identification procedure can be found in Appendix D. It is observed in Fig. 5.9a that during the first 150° wake age, the variation in the location of the tip vortex is small but the deviation from the mean value increases with wake age. This phenomenon is also reported in Ref. [5.1]. After 150° of wake age the variation in the locations of the tip vortex is noticeable from Fig. 5.9a. It should be noted that the tip vortex passes through RANS domains of the following blade and the strength of this tip vortex stays constant during and after emerging from the following blade RANS domains. As a comparison, the tip vortex geometry result from the CAMRAD II (free wake) calculation is shown in Fig. 5.9b. Overall the wake geometry from the coupled RANS/PVTM and CII-FW results is in good agreement in the first 270° of wake age. After that wake age the variation in wake geometry of the coupled RANS/PVTM wake is much higher than the CII-FW result. This is probably due to the differences in the solution schemes since free wake analysis uses non-linear iterative time stepping while the PVTM analysis uses explicit RK time stepping.

5.5.3 Tip vortex swirl velocity, core size, and circulation

Tip vortex swirl velocity is extracted from the virtual velocity measurement planes in Fig. 5.9a (see Appendix D for details). The tip vortex swirl velocity results (average of about 60 velocity measurement snapshots from the coupled RANS/PVTM wake) are presented in Fig. 5.10a for the wake age of 10°-150°. As the wake age increases, the swirl velocity peak and profile increases slightly over the range of wake age because the strength of the tip increases as it rolls in vorticity

from the vortex sheet. The comparison of swirl velocity from the coupled RANS/PVTM wake and DLR data is given in Fig. 5.10b. The data from DLR shows that the peak swirl velocity reduced significantly as the wake age increases from 20°→ 80° (36%) and from 80°→ 140° (38%). The reduction in swirl velocity is due to the effect of viscosity in and around the core of the tip vortex. This viscous effect is not modeled in the current PVTM methodology. At 140° wake age, the coupled RANS/PVTM result yields a higher swirl velocity peak than the DLR data. Comparison of the tip vortex circulation in Fig. 5.11a shows that the PVTM result has larger tip circulation than the DLR data (possibly due to the absence of the viscosity model). The tip vortex core size comparison is presented in Fig. 5.11b. The predicted core size from the PVTM simulation is about 50% higher than the test data. It should be noted that the predicted tip vortex core size is different than the PVTM cell size of 0.2c. A higher resolution PVTM cell size may improve the prediction of the core size.

5.5.4 Tip vortex location and trajectory

The trajectory of the tip vortex from DLR data and coupled RANS/PVTM results are presented in Fig. 5.12. The coupled results include instantaneous as well as averaged locations of the tip vortex at 10° wake age interval. The DLR data show greater variation in the trajectory than the coupled RANS/PVTM results. The variation in the trajectory in the simulation is caused primarily by the discrete nature of the vortex particle approach that creates unsteadiness in velocity field, loading, and finally the location of the vortex particle. The comparison of the averaged tip vortex trajectory (0°-150° wake age) from the coupled results, CII-FW, and DLR data is shown in Fig. 5.13. It is seen that the RANS/PVTM wake trajectory is not as steep as the DLR data and CII-FW results, however the difference is within one chord length over the 150° wake age. The radial and vertical locations of the tip vortex are compared in Fig. 5.14. The radial location from PVTM result correlates well with that from DLR data, while the vertical location correlation is not as good. Overall, the differences in vertical and radial locations of the tip vortex between the PVTM result and DLR data is within 0.5c-0.7c.

5.5.5 Dynamic PVTM results

Using the converged RANS/PVTM solution from Section 5.5.1 as initial conditions, the dynamic PVTM model (with the vortex diffusion and stretching models) is used to simulate the rotor for

another two rotor revolutions. The CSD coupling (retrim) is performed every 45° to speedup the coupling convergence. The vorticity field from the dynamic PVTM wake is shown in Fig. 5.15. Comparing the vorticity field from Figs. 5.15 (dynamic PVTM with stretching model) and 5.9a (static PVTM without stretching model) suggests that the dynamic PVTM yields more coherent tip vortex almost up to one rotor revolution (a half rev. for the static PVTM). In addition the tip vortex is seen to be located at the center of the virtual velocity measurement planes (locations of these planes are set for the static PVTM results), suggesting that the change in tip vortex location is small. The comparison on runtime for the dynamic PVTM and static PVTM is provided in Table 5.2. It is seen that the dynamic PVTM run much slower than the static PVTM, due to the dynamic memory model that requires extra CPUs time to allocate and search the memory for vortex particle in the linked list. The breakdown of runtime for dynamic PVTM is presented in Fig. 5.16, which shows that about 60% of runtime is used for inter-CPUs communication by Message Passing Interface (MPI) routines (N=1000). Tip vortex trajectory results, shown in Fig. 5.17, suggests that the dynamic PVTM with vortex stretching model improves correlation of the trajectory with the DLR data. This is confirmed by the correlations of the radial and vertical location of the tip vortex in Fig. 5.18. The radial location result track DLR data very well during the first 60° wake age, while the slope of the vertical location (dynamic PVTM: after 90° wake age) is very close to that of DLR data. However, comparison between the static and dynamic PVTM results (Figs 12a and Fig. 17a) shows larger scattering of the trajectory of the tip vortex between the wake age of 10°- 150°. This may be caused by the larger number of particles in dynamic PVTM producing higher level of unsteadiness in flow velocity and blade loading. For dynamic PVTM, the swirl velocity results are presented in Fig. 5.19. It is seen that the swirl velocity does decrease as the wake age increases (this trend is observed in DLR data, but not in the static PVTM results without the vortex stretching model in Fig. 5.10). Comparisons of the swirl velocity in Fig. 5.20 show good correlations of the tip vortex profile outside the vortex core. The core radius of the dynamic PVTM results is much larger than static PVTM results and DLR data. The significant reduction in peak velocity is observed in the both DLR data and dynamic PVTM results, but the peak velocity of the young vortex for the PVTM results (10° wake age, right after it is released from the RANS domain) is about half of that in DLR data (20° wake age). The accuracy of the PVTM result is limited by the accuracy of the RANS domain to preserve tip vortex strength before releasing into the PVTM domain.

Chapter VI

Concluding Remarks

This report summarizes the development and validations of a novel RANS/PVTM/CSD coupling framework, which is applied to simulate wake flow for fixed and rotary wing cases. The method employs conventional RANS solver to resolve the flow field near the bodies (rotor blades or wing) and gridless PVTM to provide accurate prediction of the evolution of the far field wake flow. For rotary wing cases, the RANS/PVTM methodology is loosely coupled to a CSD code that provides blade motion and trim analysis. The coupled RANS/PVTM/CSD framework requires proper information exchange between the modules. The results from this coupled framework are validated against several experimental data sets (a fixed-wing wind tunnel test and a hover test).

The improvements on PVTM module were made by adding the models to simulate the effects of diffusion and vortex stretching. In addition, the vortex reorientation model and efficient memory usage model are introduced to enhance the numerical stability and efficiency of the PVTM module.

For the fixed wing case, the results from RANS/PVTM method showed good correlation with the experimental test data. Comparisons of the pressure distribution and sectional loads were very good. The location of the tip vortex was also correlating well with the test data, while the correlations of other vortex parameters (core size and swirl velocity) were fair.

The validation of the RANS/PVTM/CSD methodology for the rotary wing case in hover condition was good overall. The results showed the convergence of the coupled trim parameters (C_T, θ_{75}, $C_N M^2$, $C_C M^2$, and $C_M M^2$). Rotor torque from the coupled simulation is about 50% higher than the test data (this was possibly caused by not modeling the ground effect and flow recirculating effect). The correlations of tip vortex locations were good, while that of the swirl velocity were fair. The tip vortex trajectory results were not as steep as the hover data but the difference was within one chord length over 150° wake age. The correlations on vortex

trajectory and swirl velocity are improved significantly when the vortex stretching model was used in the PVTM simulation.

The accuracy of the PVTM results was seen to be highly dependent on the accuracy of the RANS domains to capture the location and maintain the strength of the tip vortex before releasing into the PVTM domain. Improvements in the RANS domains such as higher grid resolution (near the tip vortex region), higher order schemes with low numerical dissipation may significantly improve the correlations in the future.

References

Chapter I

[1.1] Chow, J., Zilliac, G, and Bradshaw, P., "Turbulence Measurements in the Near Field of a Wingtip Vortex," *NASA TM 110418*, 1997

[1.2] Chigier, N.A. and Corsiglia, V.R., "Tip Vortices – Velocity Distributions," *NASA TM X-62087*, 1971

[1.3] Leishman, J. G., "Principles of Helicopter Aerodynamics," Cambridge University Press, NY, 2002

[1.4] Johnson, W., "Helicopter Theory," Dover Publications, NY, 1980

[1.5] McCluer, M. and Dearing, M. "Measuring Blade-Vortex Interaction Noise Using the YO-3A Acoustics Research Aircraft." 22nd European Rotorcraft Forum, Brighton, UK, September 1996

[1.6] Rossow, V. J., "Inviscid modeling of aircraft trailing vortices," NASA SP409. 1977

[1.7] Smith, S. C. and Kroo, I. M., "Induced Drag Computations on Wings with Accurately Modeled Wakes," *Journal of Aircraft*, Vol. 34, No. 2, pp. 253–255, 1997

[1.8] Rossow, V., "Classical Wing Theory and the Downward Velocity of Vortex Wakes," *J. of Aircraft*, Vol. 43, No. 2, pp. 381-385, 2006

[1.9] Stumpf, E., "Study of Four-Vortex Aircraft Wakes and Layout of Corresponding Aircraft Configurations," *J. of Aircraft*, Vol. 42, No. 3, pp.722-730, 2005

[1.10] Chatelain, P. et al.: Billion vortex particle direct numerical simulations of aircraft wakes, *Computer Methods in Applied Mechanics and Engineering*, Vol. 197,pp. 1296-1304, 2008

[1.11] Opoku, D. G., Triantos, D. G., Nitzsche, F., and Voutsinas S. G., "Rotorcraft Aerodynamic and Aeroacoustic Modeling Using Vortex Particle Methods," *Proceedings of the International Council of the Aeronautical Sciences*, pp. 299.1-299.11, 2002

[1.12] Lee, D. J., and Na S. U., "Numerical Simulations of Wake Structure Generated by Rotating Blades Using a Time Marching Free Vortex Blob Method," *European J. Fluid Mechanics – B/Fluids*, 17(4), pp. 1-13, 1998

[1.13] Baeder, J. D., Duraisamy, K., and Sitaraman, J., "High Resolution Wake Capturing Methodology for Improved Rotor Aerodynamic Computations," *Proceedings of the American Helicopter Society Annual Forum*, Dallas, TX, 2005

[1.14] Potsdam, M., Yeo, H. and Johnson, W., "Rotor Airloads Prediction using Loose Aerodynamic/Structural Coupling," *Proceedings of the American Helicopter Society Annual Forum,* Baltimore, MD, 2004.

[1.15] Brown, R. E., "Rotor Wake Modeling for Flight Dynamic Simulation of Helicopters," *AIAA Journal*, Vol. 38, No.1, pp. 57-63, 2000.

[1.16] Anusonti-Inthra, P., "Development of Rotorcraft Wake Capturing Methodology Using Fully Coupled CFD and Particle Vortex Transport Method," *Proceedings of the 62nd AHS Annual Forum*, Phoenix, AZ, 2006

[1.17] Sitaraman, J., "CFD Based Unsteady Aerodynamic Modeling for Rotor Aeroelastic Analysis", PhD. Thesis, Dept. of Aerospace Engineering, University of Maryland, 2003

Chapter II

[2.1] Winckelmans, G. S., "Topics in Vortex Methods For the Computation of Three- and Two-dimensional incompressible unsteady flows," PhD. Thesis, California Institute of Technology, 1989

[2.2] Cottet, G. and Koumoutsakos, P. D., "Vortex Methods: Theory and Practice," Cambridge University Press, 2000

[2.3] Johnson, W., "Rotorcraft Aerodynamic Models for a Comprehensive Analysis," *Proceedings of the American Helicopter Society Annual Forum*, Washington D.C., 1998

[2.4] Potsdam, M., Yeo, H. and Johnson, W., "Rotor Airloads Prediction using Loose Aerodynamic/Structural Coupling," *Proceedings of the American Helicopter Society Annual Forum,* Baltimore, MD, 2004

Chapter III

[3.1] Kreyszig, E., "Advanced Engineering Mathematics," *John Wiley & Sons Inc.*, New York, 1998.

[3.2] Subramaniam, S., "A New Mesh-Free Vortex Method," Ph.D. Thesis, Florida State University, 1996

[3.3] Gharakhani, A., "A Higher Order Vorticity Redistribution Method for 3-D Diffusion in Free Space," Sandia Report, Sandia National Laboratories, SAND2000-2505, 2000

[3.4] Manfield and Knio, "Dynamic LES of Colliding Vortex Rings Using 3D Vortex Method," *J. of Comp. Physics*, Vol. 152, 1999

Chapter IV

[4.1] McAlister, K. and Takahashi, R.K., "NACA0015 Wing Pressure and Trailing Vortex Measurements," *NASA-TP-3151*, 1991

Chapter V

[5.1] van der Wall, B.G. and Richard, H., "Hover Tip Vortex Structure Test (HOTIS) – Test Documentation and Representative Results," German Aerospace Center (DLR) Institute Report, IB 111-2008/16, May 2008

[5.2] van der Wall, B.G., Burley, C.L., Yu, Y.H., Pengel, K., Beaumier, P., "The HART II Test - Measurement of Helicopter Rotor Wakes", Aerospace Science and Technology, Vol. 8, No. 4, p. 273-284, 2004

Appendix A

Adaptive Time Step Methodology

Adaptive time stepping for the PVTM analysis is developed to control the error associated with time discretization especially for particle vortex locations. The location of each vortex particle is obtained by solving Eq. A.1.

$$x^{k+1} = x^k + \int u dt \tag{A.1}$$

where x^k is the initial location and u is the induced velocity. Let us define a measure of accuracy, A_m , as follows (m is the numbers of time sub-step)

$$A_m = (X\text{-}X_o)/(m\ dt), \quad m = 1, 2, .., M \tag{A.2}$$

An example of this measure of accuracy is shown in Fig. A1. From Fig. A1, it is seen that A_m is an exponential function of the number of time substep, m, as follows:

$$A_m = A_1 m^{-2} \tag{A.3}$$

From Eq. A.3, the numbers of required substeps, M, to achieved a desired accuracy, ε, is:

$$M = \sqrt{A_1 / \varepsilon} \tag{A.4}$$

Appendix B

A Two Vortex Particles Problem

This appendix involves the analysis of a system of two vortex particles. The particles have strength vectors and location vectors as follows:

$$\begin{aligned} \alpha_1 &= [0 \quad 1 \quad 0],\ x_1 = [\ 0.05 \quad 0 \quad 0] \\ \alpha_2 &= [0 \quad 0 \quad 1],\ x_2 = [-0.05 \quad 0 \quad 0] \end{aligned} \tag{B.1}$$

Using $\delta^2 = (0.1)^2/2$, the induced velocity between the two particles is:

$$u_{1\to 2} = -\frac{1}{4\pi}\frac{(x_2 - x_1)\times\alpha_1}{\left(|x_2 - x_1|^2 + \delta^2\right)^{3/2}} = [0 \quad 4.3316 \quad 0] \tag{B.2}$$

$$u_{2\to 1} = -\frac{1}{4\pi}\frac{(x_1 - x_2)\times\alpha_2}{\left(|x_1 - x_2|^2 + \delta^2\right)^{3/2}} = [0 \quad 0 \quad 4.3316]$$

The strain rate tensor, ∇u, can be calculated from adding Δx, Δy, Δz to the velocity evaluation location and re-evaluated the velocity. The strain rate tensor and its eigenvalues are:

$$\nabla u_{1\to 2} = \begin{bmatrix} 0 & -43.3179 & 0.8661 \\ -43.2942 & 0 & 0 \\ 0 & 0 & 0 \end{bmatrix},\ \text{eig}(\nabla u_{1\to 2}) = [43.3061\ -43.3061\ 0] \tag{B.3}$$

$$\nabla u_{2\to 1} = \begin{bmatrix} 0 & 0.8661 & 43.3179 \\ 0 & 0 & 0 \\ 43.2942 & 0 & 0 \end{bmatrix},\ \text{eig}(\nabla u_{2\to 1}) = [43.3061\ -43.3061\ 0]$$

The eigenvectors χ_0 associated with λ_0 (eigenvalue = 0) are shown in Fig. B.1. It should be noted that the sum of the eigenvalues is zero (continuity condition and divergence free condition). These eigenvectors represent the directions to which the strength of the vortex particle should be reoriented in order to obtain a conserved vorticity solution (see also Section 3.1.1). The direction of eigenvector χ_0 for $\nabla u_{1\to 2}$ is similar to α_1, and the eigenvector χ_0 for $\nabla u_{2\to 1}$ is pointing in the direction of α_2. This is true for any pair of vortex particles. Thus in general, the reorientation of

the vortex strength vector should be in the direction of the eigenvector, χ_0. To simplify the process for vorticity field with more than one particles, the vortex stretching term is modified from Eq. B.4 (direct differentiation of Eq. B.2) to B.5 to take into account the proper reorientation of each vortex particle. Equation B.6 is introduced to adjust the reorientation speed of the strength vectors.

$$\alpha^P \cdot \nabla u_i = \sum_i \frac{1}{4\pi} \frac{\alpha^P \times \alpha_i}{\left(\left|x^P - x_i\right|^2 + \delta^2\right)^{3/2}} + \frac{3\left(\alpha^P \cdot (x^P - x_i) \times \alpha_i\right)(x^P - x_i)}{\left(\left|x^P - x_i\right|^2 + \delta^2\right)^{5/2}} \tag{B.4}$$

$$\alpha^P \cdot \nabla u_i = \sum_i \frac{1}{4\pi} \frac{\left(\alpha^P \times \alpha_i\right) \times \alpha^P}{\left(\left|x^P - x_i\right|^2 + \delta^2\right)^{3/2}} \tag{B.5}$$

$$\alpha^P \cdot \nabla u_i = \sum_i \frac{5|\alpha_i|}{4\pi} \frac{\left(\alpha^P \times \alpha_i\right) \times \alpha^P}{\left(\left|x^P - x_i\right|^2 + \delta^2\right)^{3/2}} \tag{B.6}$$

Using Eqs. (B.4-B.6), the vortex trajectory of this two vortex particle system is shown in Fig. B.2. It should be noted that the two vortex particles realign themselves properly after several time steps using Eqs (B.5 and B.6), and the total vorticity is conserved ($|\alpha_1^N| = |\alpha_1^0|$, $|\alpha_2^N| = |\alpha_2^0|$). The distance between the two vortex particles is presented in Fig. B.3. It is seen that the distance between the vortex particles is increasing unboundedly when Eq. B.5 and B.6 are used. To mitigate this unbounded drifting (associated with explicit time integration scheme), an attraction term is introduced in the velocity calculation (Eq. B.2) as follows:

$$u(Y) = \sum_i -\frac{1}{4\pi}\left(\frac{(Y - x_i) \times \alpha_i + 0.05(Y - x_i)\left|(Y - x_i) \times \alpha_i\right|}{\left(\left|Y - x_i\right|^2 + \delta^2\right)^{3/2}}\right) \tag{B.7}$$

Using Eqs. (B.5) and (B.7), the distance between the two vortex particles is similar to that obtained using Eq. (B.4), see Fig. B.3.

It is recognized that Eq. (B.7) is not derived from any physical phenomena, and the following section serves to identify the source(s) of the modification introduced in Eq. (B.7). One possible source is the accumulated error from the time integration routine (explicit Rouge-Kutta fourth order). As a comparison the following time integration routines are used and the results are compared in Fig. B.4 (using Eq. (B.2) and (B.6), and a different initial vortex strength and location from the previous section).

(a) Explicit Rouge-Kutta (6^{th} order)

(b) Implicit (preditor-corrector) Adam-Bashford (2^{nd}, 3^{rd}, and 4^{th} order)

The comparison shows no improvement using the higher order explicit integration schemes, but the introduction of the implicit time integration routines can actually improve the "particle drifting" problem. With these results, it can be concluded that the "particle drifting" problem can be solved using higher order implicit integration schemes with a sufficiently small time step. However, in practice using the implicit time integration routine increases the memory requirement by a factor of two, three, or four depending on the required order of accuracy. This requirement is impractical when the system involves very large number of particle (100000+). In addition, the time step required is extremely small making the simulation very computationally expensive.

Thus, for engineering purposes, a modification is introduced to Eq. (B.2) to include the attraction term as shown in Eq. (B.8) as a way to reduce the discretization error from the explicit time integration routine used (RK4). This attraction term is used only for calculating velocity from particle to another particle, and not in the induced velocity calculation for coupling with the RANS domains.

$$u(Y) = \sum_i -\frac{1}{4\pi}\left(\frac{(Y - x_i)\times\alpha_i + \eta \frac{(Y-x_i)}{|Y-x_i|}\left|(Y - x_i)\times\alpha_i\right|}{\left(\left|Y - x_i\right|^2 + \delta^2\right)^{3/2}} \right) \tag{B.8}$$

where the attraction coefficient, η, is a variable controlling the time discretization error. It is assumed that η is a function of the time step, Δt, and the optimal values of η can be determined by running the simulation adjusting η such that the "particle drifting" is negligible (with RK4 scheme for various Δt). As a function of Δt, the optimal attraction coefficients, η_1 and η_2, are shown in Fig. B.5. A trajectory of a two particles system with and without the attraction term is shown in Fig. B.6. It is observed that the inclusion of the attraction term, η_1, significantly reduced the "particle drifting" problem, however the distance between the particles is still increasing. A small offset is added to η_1 resulting in η_2 to make the "particle drifting" problem negligible (see Figs. B.5- B.7).

Appendix C

Single Bladed Rotor Cases

This appendix presents results for single bladed rotor cases that demonstrate the effects of some PVTM modeling methods and parameters including (i) dynamic PVTM methodology, (ii) PVTM stretching model, and (iii) high resolution PVTM.

C.1 Dynamic PVTM

The single-bladed hover results using the static PVTM and dynamic PVTM methodology are shown in Figs. C.1-C.2. The vorticity fields presented in Figs. C.1 show that the static PVTM and dynamic PVTM results are equivalent. The rotor loading comparison in Fig. C.2 confirms that the rotor loading is the same using the two approaches. The effect of the attraction term (Appendix B) is presented in Fig. C.3. The tip vortex from PVTM wake with the attraction term is much more compact and coherent than the PVTM result without the attraction term.

C.2 PVTM stretching model

With the vortex stretching methodology (Section 3.6), the vortex particle releases from a single-bladed rotor is shown in Fig. C.4 (color representing the characteristic length, L_c). The figure shows the characteristic length of the vortex sheet at 2 azimuthal positions. It is observed that the vortex particles near the tip vortex undergo splitting due to vortex stretching very quickly after the release (about 5°-10° wake age) the rest of the vortex sheet reaches the threshold for splitting after approximately 20°-45° wake age. The splitting of the vortex particle in the vortex sheet continues after the initial splitting. Comparison of the particle field with and without vortex stretching model is presented in Fig. C.5. The resulting particle field with the vortex stretching model is seen to be much more uniform, especially in the vortex sheet near the tip vortex. Comparisons of rotor loading seen in Fig. C.6 shows that the PVTM results with the

vortex stretching model yield a similar rotor loading without the stretching model. Computational efficiency of the PVTM with vortex stretching model is summarized in Table C.1. With the vortex stretching model, both the numbers of particles and the runtime increase by about 300% from the baseline on stretching case.

C.3 High resolution PVTM wake

With the development of the dynamic PVTM methodology using the dynamic memory model, a simulation with high resolution PVTM wake is possible. The differences in particles released in one time step at various PVTM resolutions can be seen in Figs. C7-C.8. By observing the clustering of the vortex particles near the tip vortex, it is seen the high resolution PVTM wake result in Fig. C.8b provides better tip vortex profiles (location, strength distribution) than the low resolution PVTM wake. The high resolution PVTM wake also affects the resolution of the coupling methodology between the RANS and PVTM domains. For example, coupling a RANS domain to PVTM domain (or other RANS domains) involves a conversion from the RANS vorticity field (Fig. C.9) into a particle representation of the field (Fig. C.10-C.11). A high resolution PVTM conversion (Fig. C.11) yields four times as many particles than a lower resolution PVTM conversion (Fig. C.10), but again provides better vorticity profile. Comparison of vorticity field, rotor loading, and computational efficiency of various PVTM wake resolution after one rotor revolution are presented in Figs. C.12 and C.13, and Table C.2, respectively. Overall the high resolution PVTM wake improves the vorticity profile (without changing the rotor loading), while increasing the numbers of vortex particles and the runtime.

Appendix D

Rotor Tip Vortex Parameter Identification

This appendix outlines the procedure to identify the tip vortex parameters, i.e. core size, swirl velocity, and location. Starting with the 3D induced velocity recorded in a measurement plane, the 3D velocity is projected onto the measurement plane to yield a 2D velocity field, and the 2D velocity is processed to calculate the vorticity perpendicular to the measurement plane as shown in Fig. D.1. The vorticity is calculated using a fourth order central difference scheme, and a 2-D gaussian filter is applied to the processed vorticity results to reduce the numerical noise. An estimate of the location of the tip vortex, X_{tip}^{2}, can be found by searching for the maximum vorticity in the measurement plane. Using this estimated location as a starting point, a more sophisticated scheme is used to obtain more accurate location of the tip vortex, X_{tip}^{1}, using the velocity profile search. The scheme identifies the "I index" of the tip vortex by searching the vertical velocity, V_I, for the mid point between minimum and maximum velocity and its derivative, dV_I/dI, for the maximum value of the derivative as shown in Fig D.2. Similarly, the "J index" of the tip vortex is identified by searching the horizontal velocity, U_J, and its derivative, dU_J/dJ. The final location of the tip vortex, X_{tip}, is simply the average between X_{tip}^{1} and X_{tip}^{2}. Once the location of the tip vortex is identified, the horizontal (U) and vertical (V) swirl velocities are obtained using 1D interpolation in the appropriate direction. The final swirl velocity, V_θ, is the average between the horizontal and vertical swirl velocities (Fig. D.3).

Tables

Table 4.1: RANS/PVTM case metric

Cases	Δt^*	CFD grid boundary		PVTM cell resolution		PVTM redistribution methods	
		Wrap around direction (chord)	Down stream direction (chord)	Level 0 (chord)	Level 1 (chord)	Stretching model	Diffusion model
0	0.02	1	0.5	0.1	0.4		
1	0.02	1	0.5	0.05	0.2		
2	0.02	1	0.5	0.05	0.2		X
3	0.02	1	1	0.05	0.2		
4	0.02	1	1	0.05	0.2		X
5	0.01	1	0.5	0.1	0.4		
6	0.01	1	0.5	0.05	0.2		
7	0.01 (adaptive)	1	0.5	0.05	0.2		

*non-dimensinalized by c/a, (c: wing chord, a: speed of sound)

Table 4.2: Number of vortex particles and calculation time for the RANS/PVTM calculations using 8 CPUs

Cases	CFD-PVTM Total Time Steps	PVTM vortex particles		Calculation time of the last time step		
		Level 0	Level 1	CFD (%)	PVTM (%)	Total (sec.)
0	9000	1355	76	35.02	64.98	98.81
1	9000	5415	291	46.50	53.50	111.96
2	9000	5484	286	46.48	53.52	112.11
3	9000	4159	307	47.27	52.73	158.75*
4	9000	4171	295	47.02	52.98	170.17*
5	17000	1712	71	34.34	65.66	119.56*
6	17000	4978	290	31.51	68.49	87.54
7	17000	5046	296	33.51	66.49	85.19

*A different computing cluster is used, and this cluster is running about 20% slower

Table 4.3: Full CFD case parameters and calculation time using 4 CPUs

Cases	CFD Total Time Steps	Δt^*	CFD grid boundary		Calculation time of the last time step
			Wrap around direction (chord)	Down stream direction (chord)	
0A	10000	0.02	6	6	73.78*

*A different computing cluster is used, and this cluster is running about 20% slower

Table 5.1: Properties of the HOTIS (HART II) model rotor

Property	Value
Number of blades	4
Radius	2.0m
Root cutout	0.44m
Chord	0.121m
Solidity	0.077
Airfoil	NACA23012mod
Linear twist	-8.0deg/R
Nominal speed	109 rad/s
Tip mach number	0.633

Table 5.2: PVTM runtime comparison

Model	Number of particles	Number of CPUs	Runtime RANS (%)	Runtime PVTM (%)	Runtime per time step (sec)
Static PVTM	101649	12	42.15	57.85	105.75
Dynamic PVTM	84578	8	4.61	95.39	1301.72

Table C.1: Comparisons of computational efficiency of static and dynamic PVTM (with and without vortex stretching)

Case	*d*/c	Particles	Run time (sec) Last time step	CPUs
Static PVTM	0.20	8183	66.27	4
Dynamic PVTM (no stretching)	0.15	16481	92.93	8
Dynamic PVTM (with stretching)	0.15	45585	330.55	8

Table C.2: Comparisons of computational efficiency of static and high resolution PVTM

Case	d/c	Particles	Run time (sec) Last time step	CPUs
Static PVTM	0.20	8183	66.27	4
Dynamic PVTM	0.20	11411	59.19	4
	0.15	16481	92.93	8
	0.10	29018	336.68	8

Figures

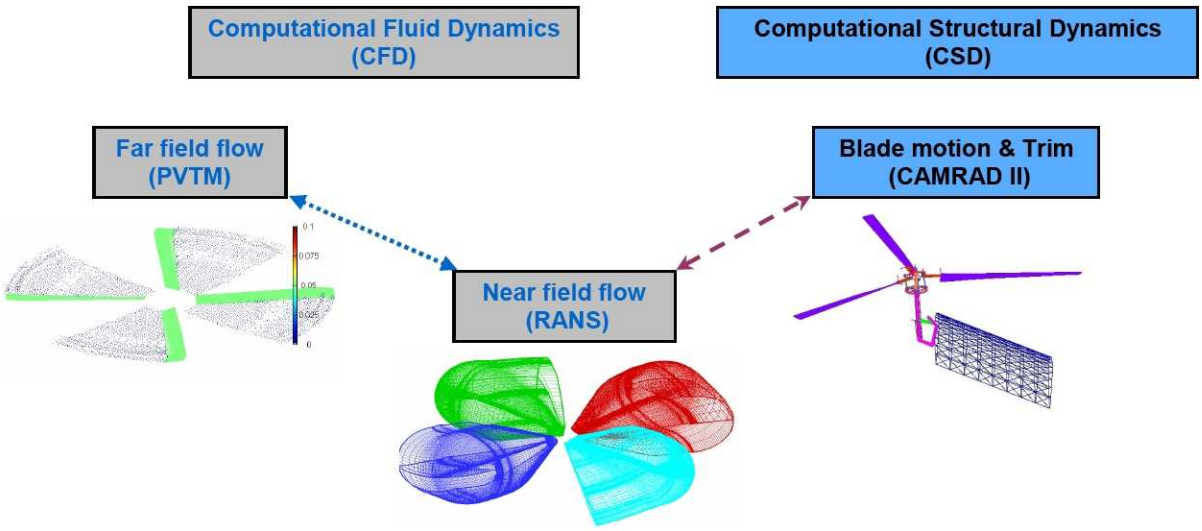

Figure 1.1: Overview of coupled PVTM/RANS/CSD methodology

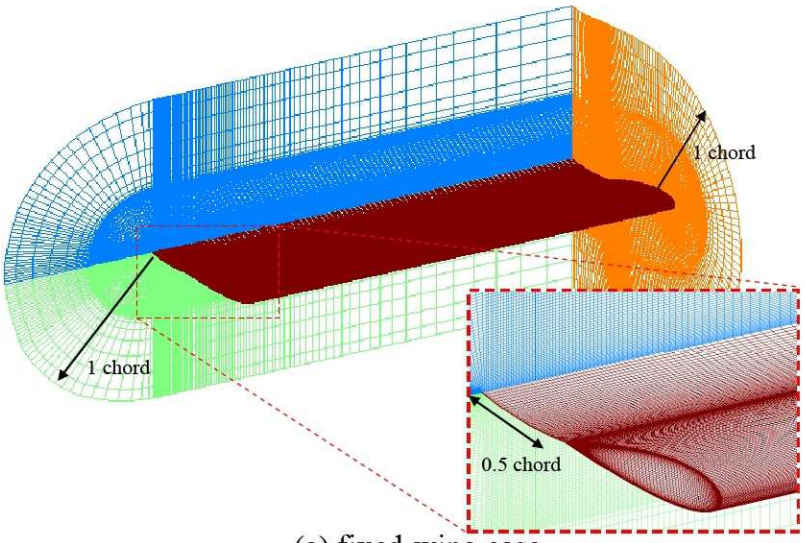

(a) fixed-wing case

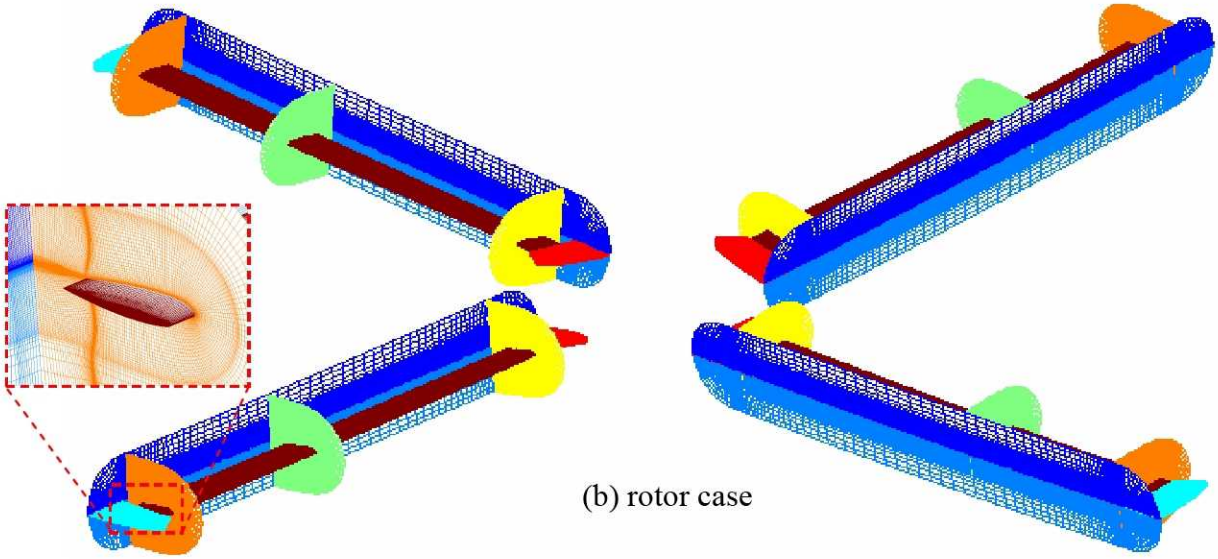

(b) rotor case

Figure 2.1: RANS grid for near filed flow calculation:
(a) fixed-wing case and (b) rotor case

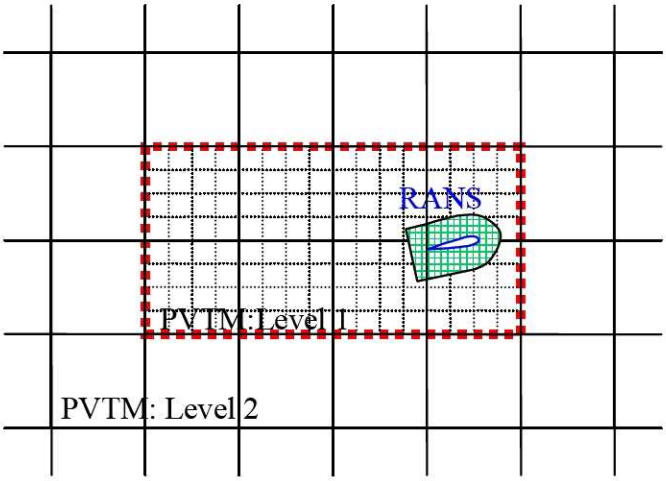

(a) fixed-wing case

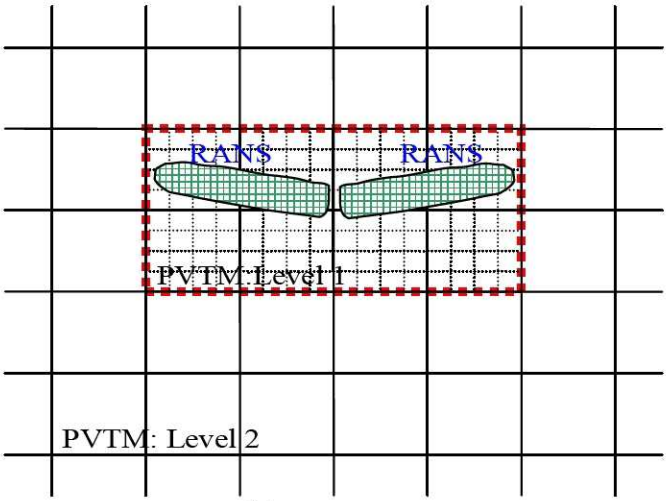

(b) rotor case

Figure 2.2: Two dimensional view of representative 3D multi-level PVTM domains: (a) fixed-wing case and (b) rotor case

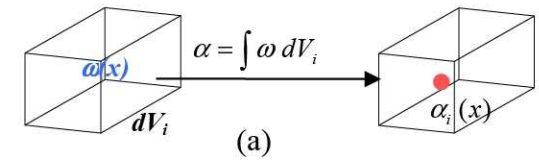

(a)

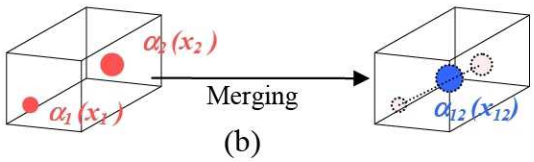

(b)

Figure 2.3: (a) Particle representation of a continuous vorticity field, (b) Merging of vortex particles in the same PVTM computational cell

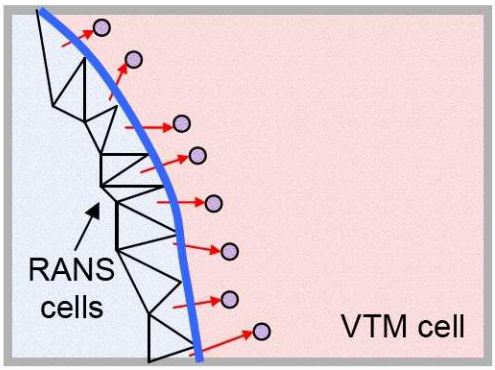

(a) released particles (convection)

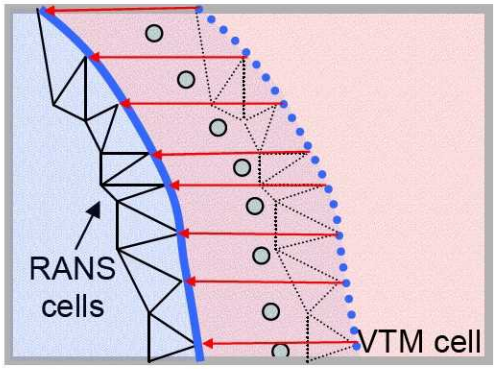

(b) released particles (grid movement)

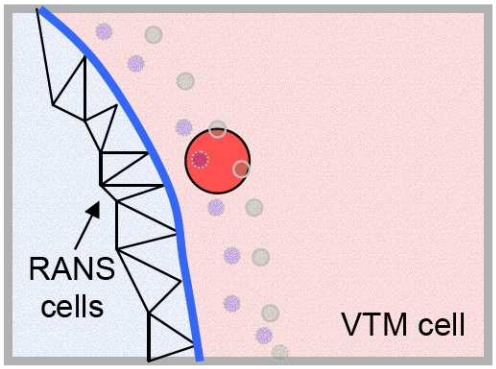

(c) released particle after merging

Figure 2.4: Vortex particle released from RANS domain: (a) from convection process, (b) from grid movement, and (c) after merging

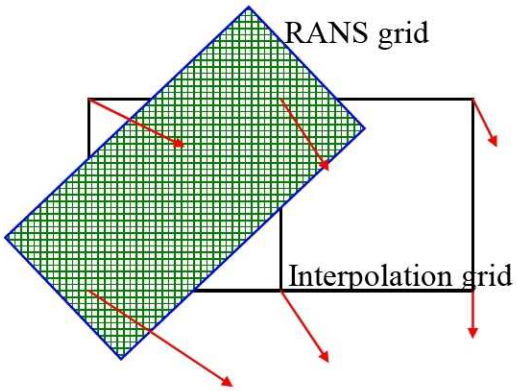

Figure 2.5: Induced velocity from PVTM domain on interpolation grid before using 3D linear interpolation to calculate induced inflow on RANS grid

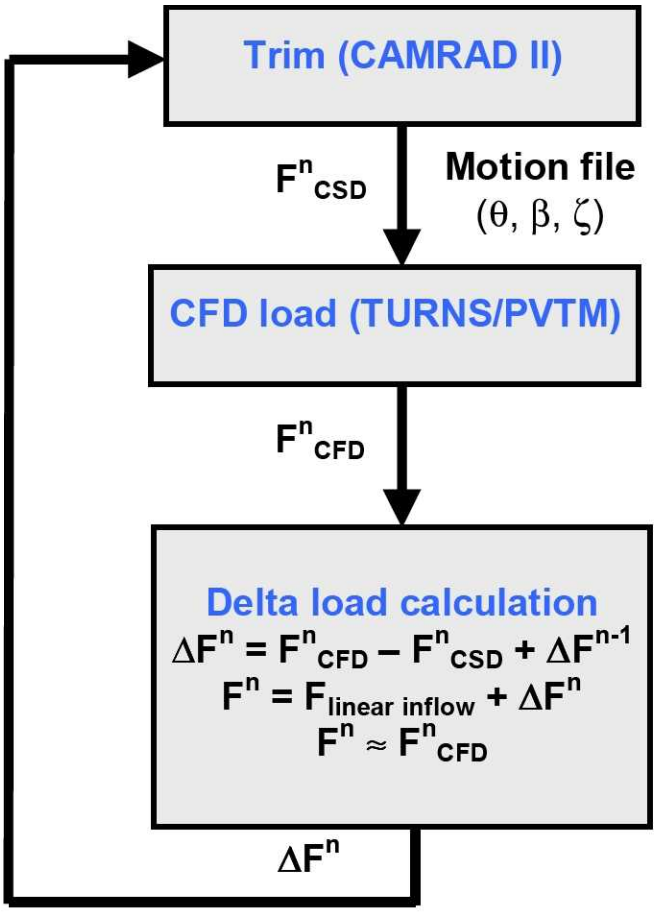

Figure 2.6: Loose coupled trim procedure for coupling RANS/PVTM to CAMRAD II

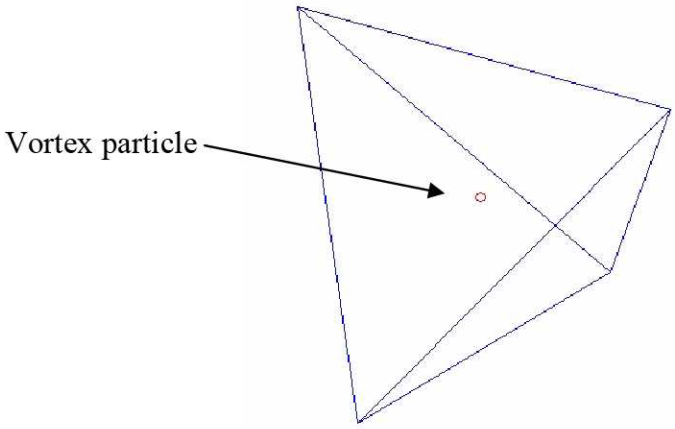

Figure 3.1: Interpolation basis points for calculating induced velocity within RK scheme and local strain tensor

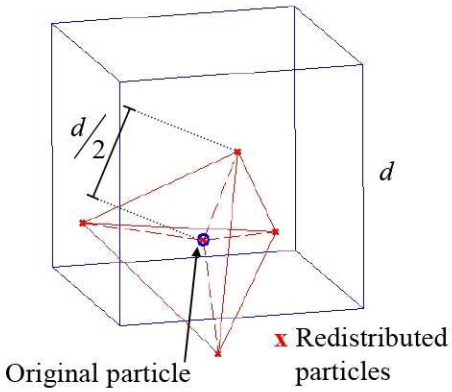

Figure 3.2: Vortex redistribution model than simulate diffusion process

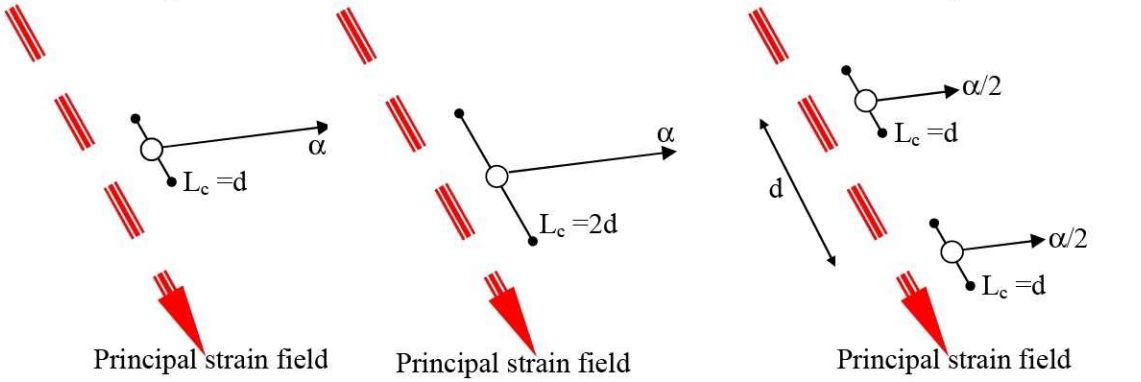

(a) $t = t_o$ (b) $t = t_o + k\mathrm{d}t$ (before split) (c) $t = t_o + k\mathrm{d}t$ (after split)

Figure 3.3: Vortex stretching from invariant strain tensor after k time steps

$$\left(\frac{L_c^k}{L_c^0} = (1.0 + \hat{\varepsilon})^k = 2\right)$$

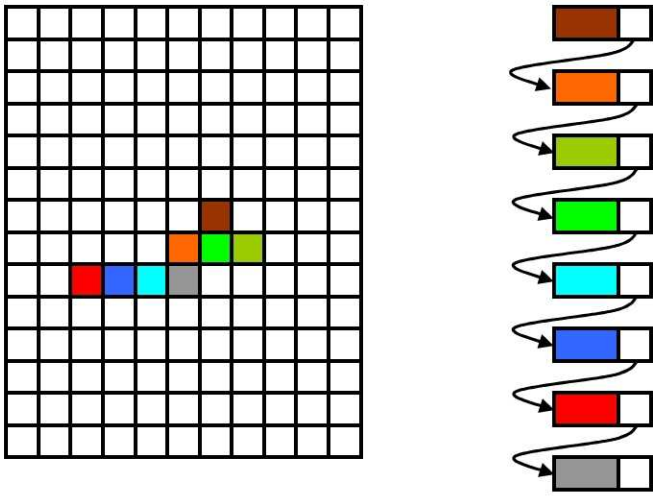

(a) static memory model (Static PVTM) (b) dynamic memory model (Dynamic PVTM)

Figure 3.4: Memory map for PVMT implementation with (a) static and (b) dynamic memory models

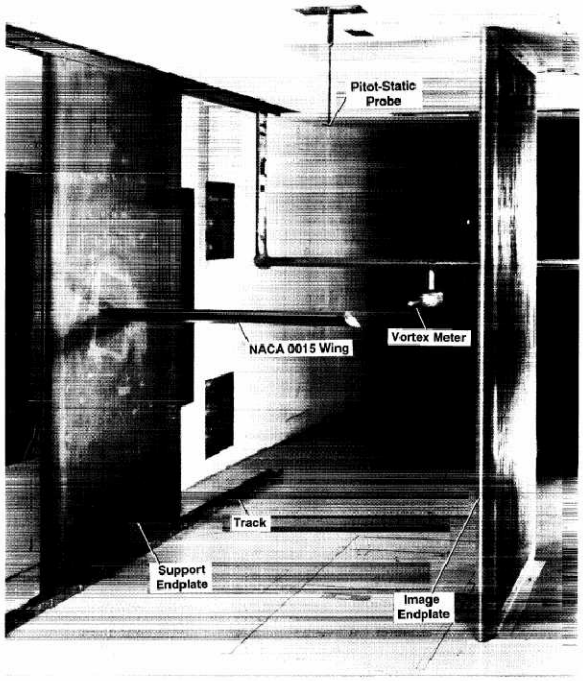

Figure 4.1: Experimental set up for the NACA 0015 wing in wind tunnel tests (from Ref. [4.1])

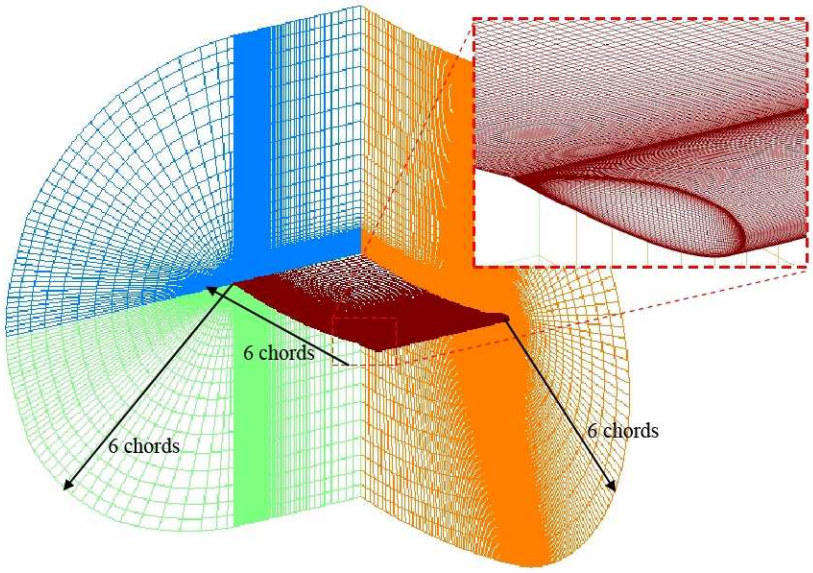

Figure 4.2:Grid for full RANS calculation of the square tip wing (5M grid points)

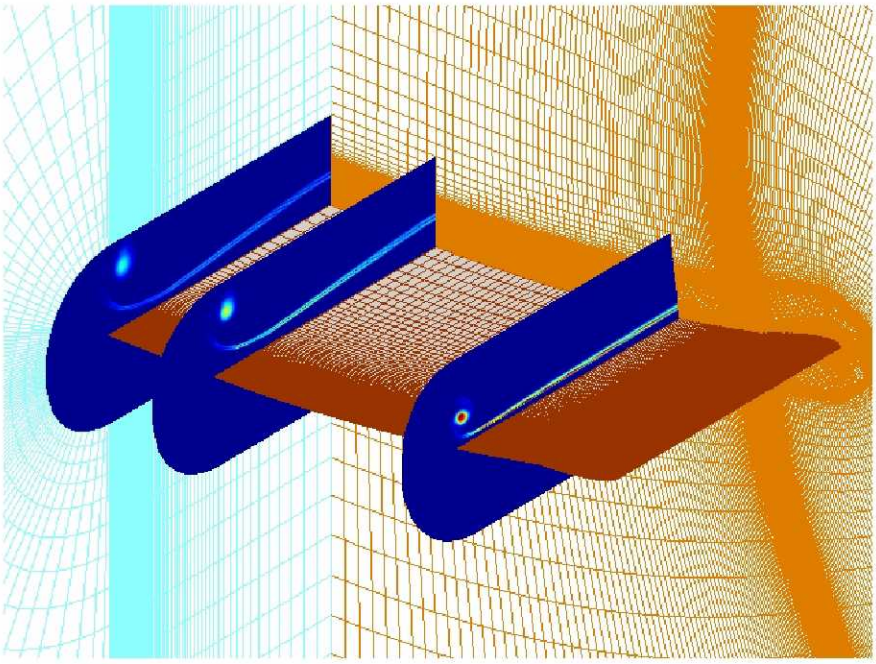

Figure 4.3: Vorticity profile calculated using full RANS calculation for square tip wing

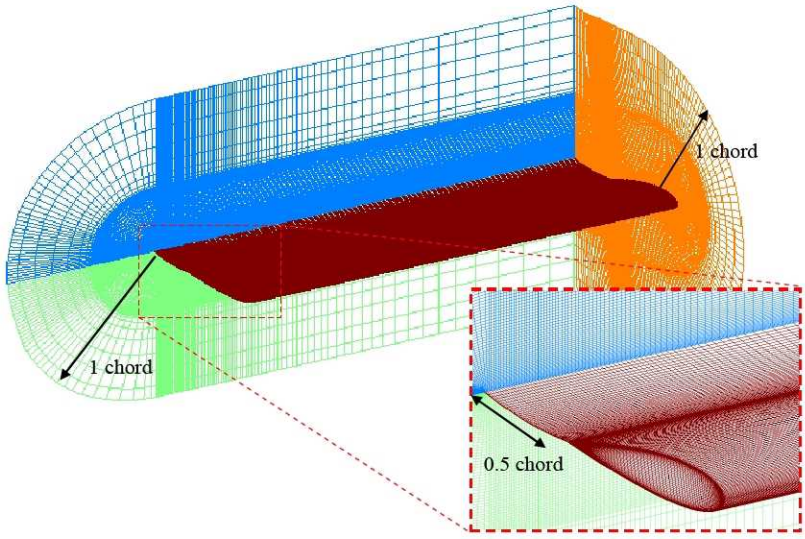

Figure 4.4: RANS grid for coupled RANS/PVTM calculation of the square tip wing (2.5M grid points).

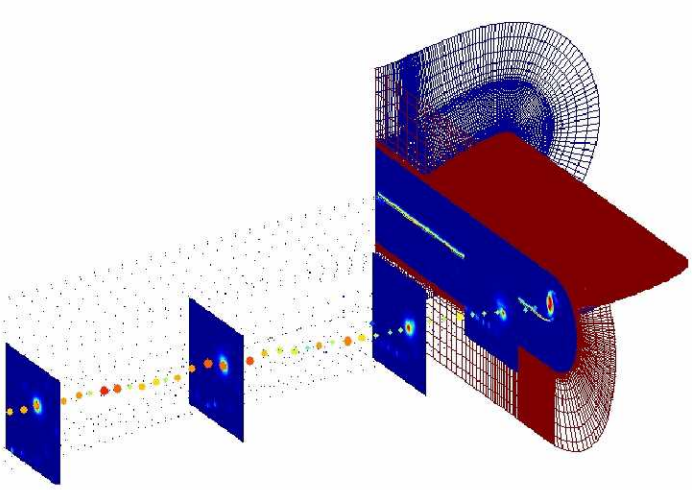

(a)

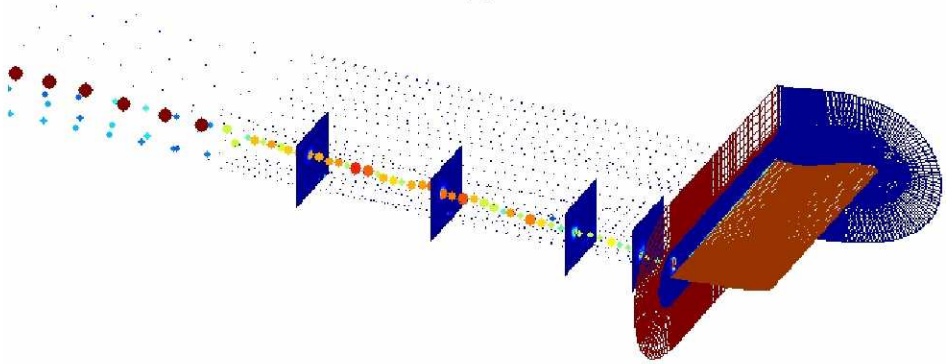

(b)

Figure 4.5: Vorticity profile calculated using coupled RANS/PVTM method showing velocity planes and vortex particles in the PVTM domain.

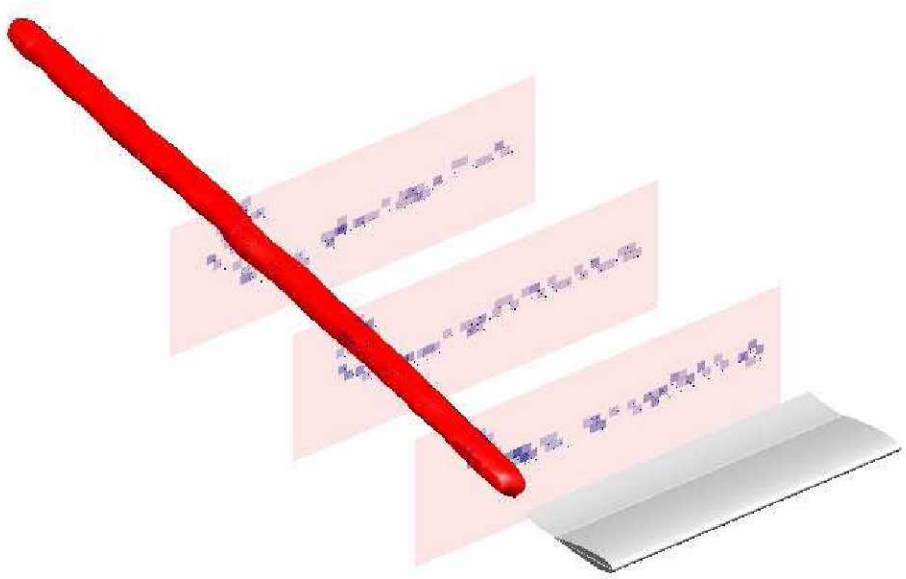

Figure 4.6: Vorticity isosurface and particle trace on three vertical planes of the wake behind a square tip wing simulated using the coupled RANS/PVTM method

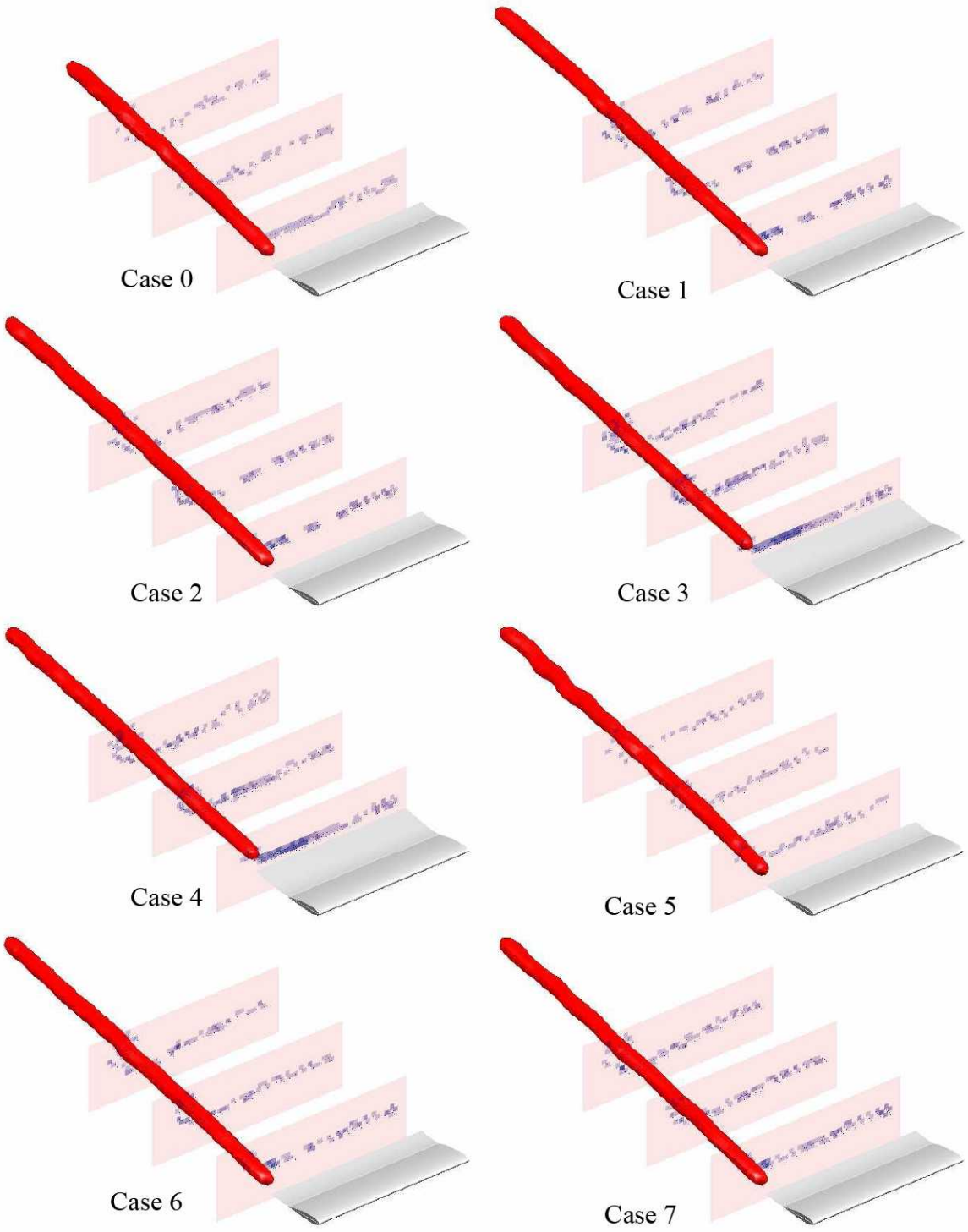

Figure 4.7: Vorticity isosurface and particle trace on three vertical planes of the wake behind a wing simulated using RANS/PVTM method

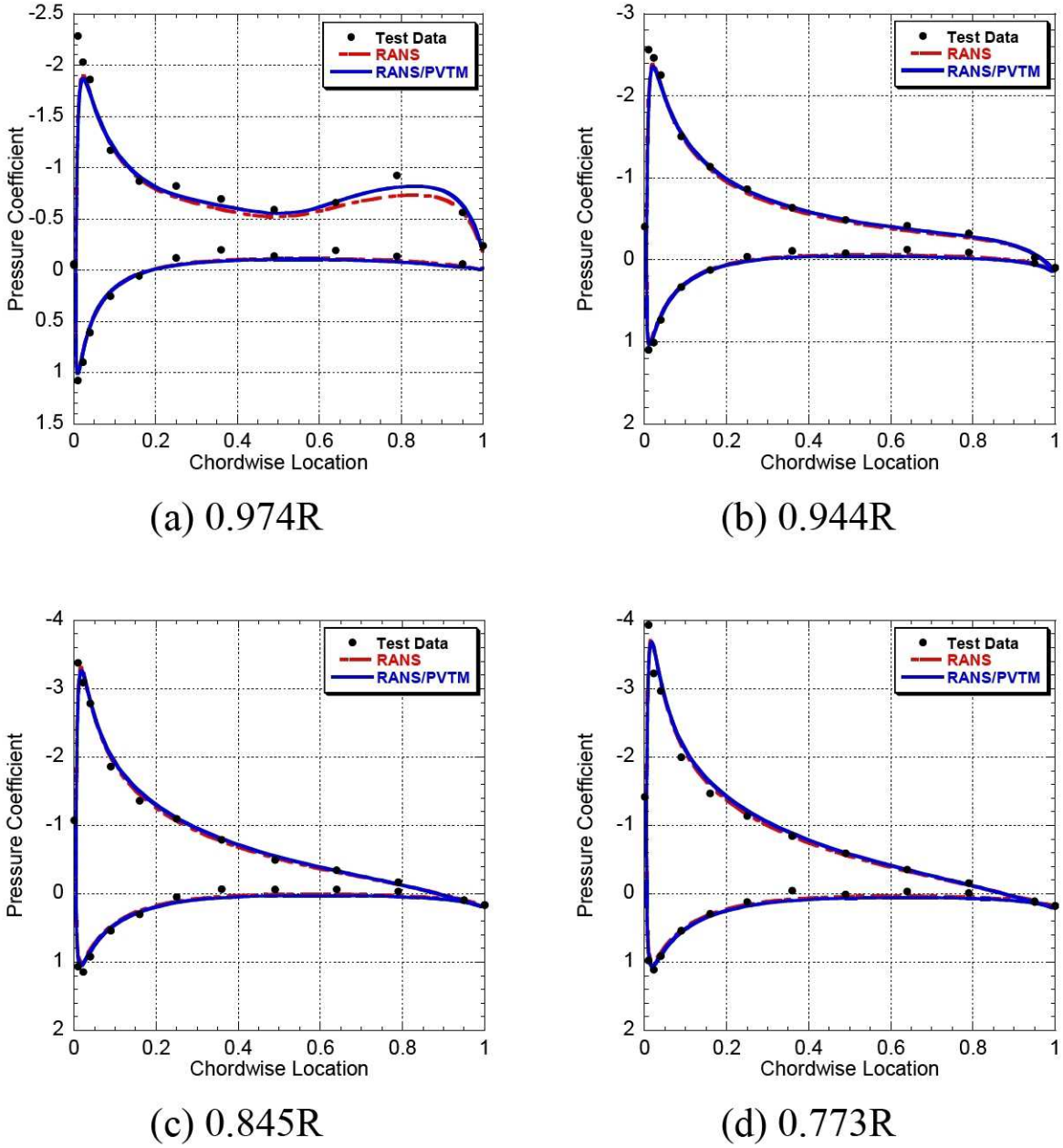

Figure 4.8: Airfoil surface pressure distributions near the wing tip (case 7)

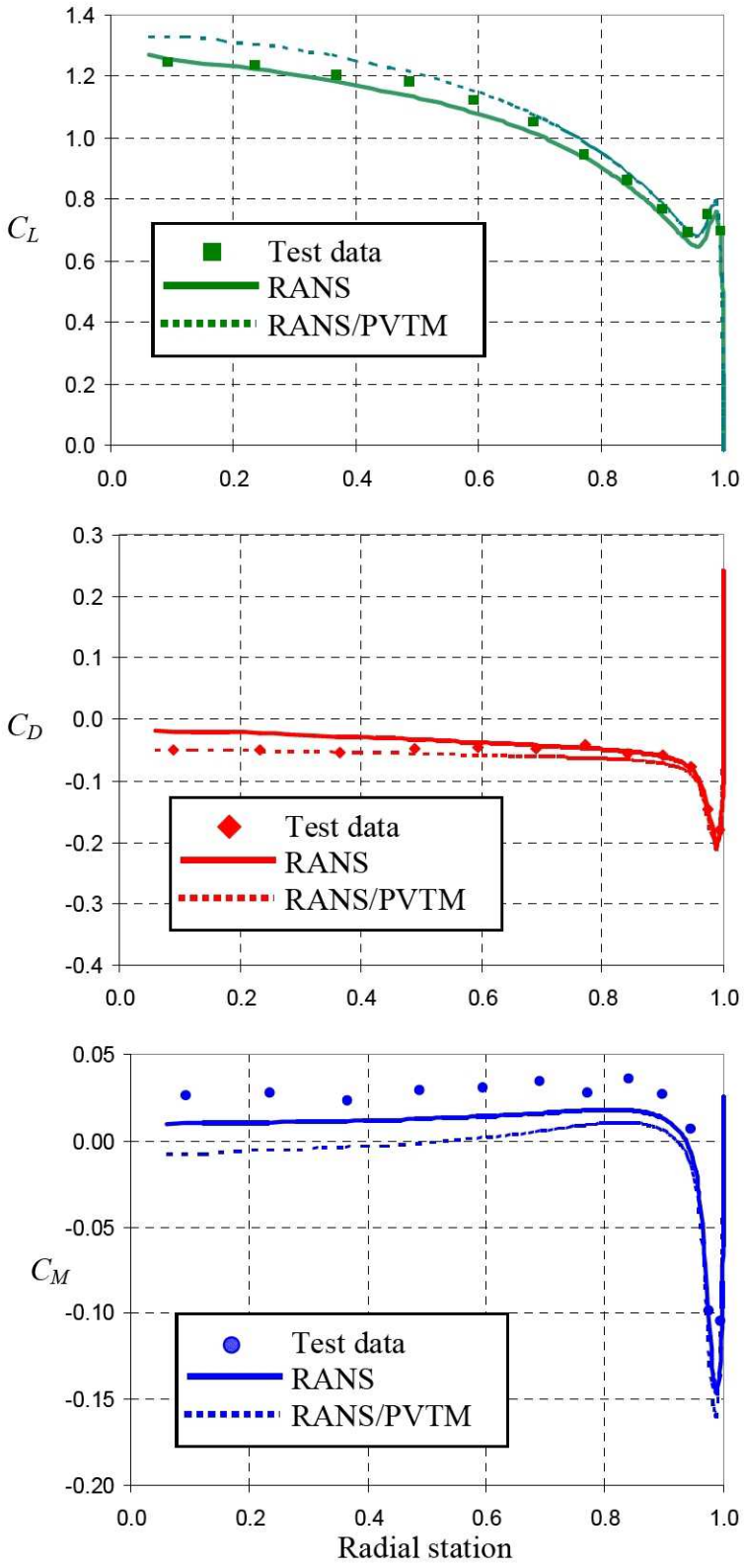

Figure 4.9: Sectional lift, drag, and moment coefficients along wing span (case 7)

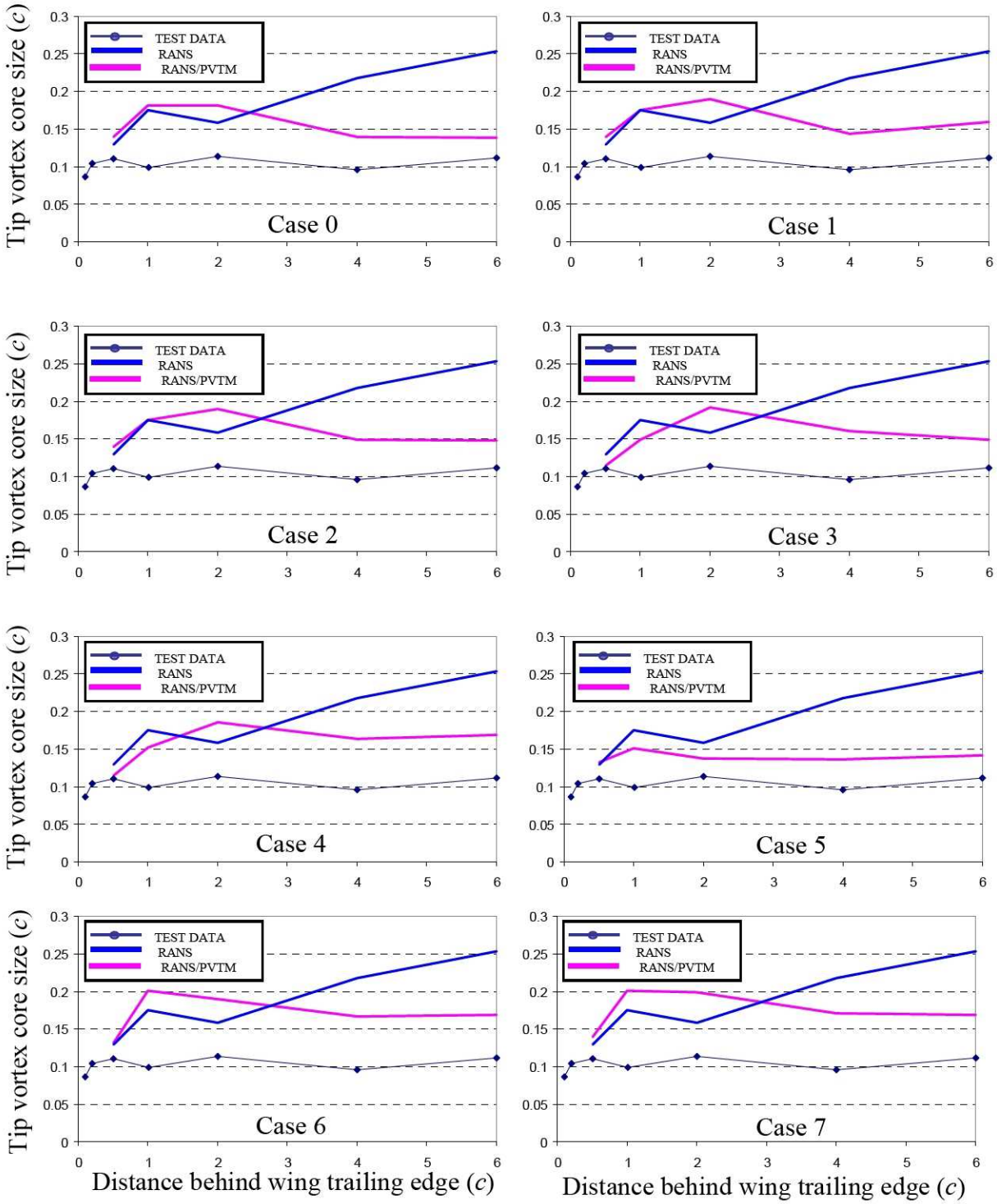

Figure 4.10: Comparison of tip vortex core size

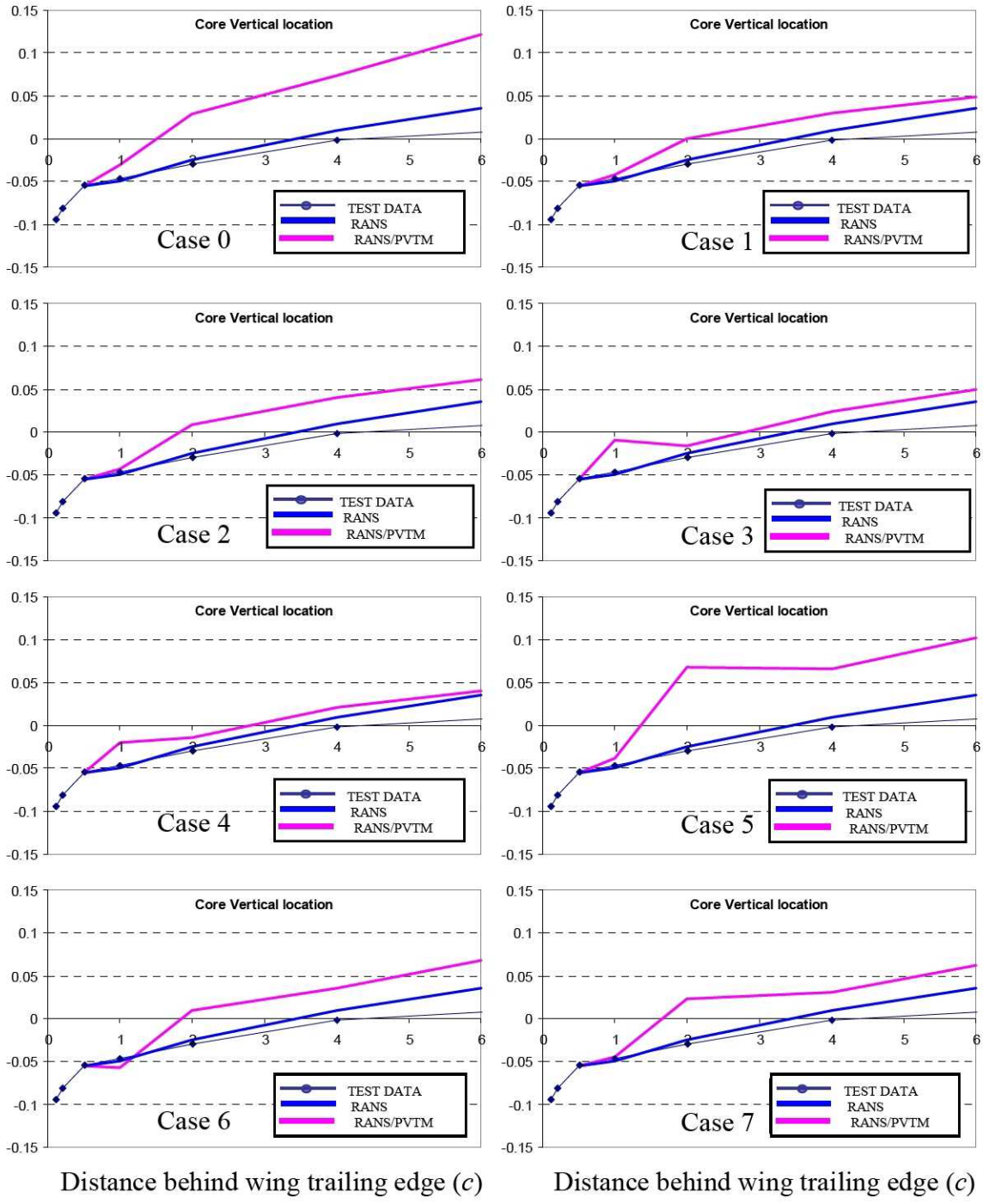

Figure 4.11: Comparison of tip vortex core vertical location

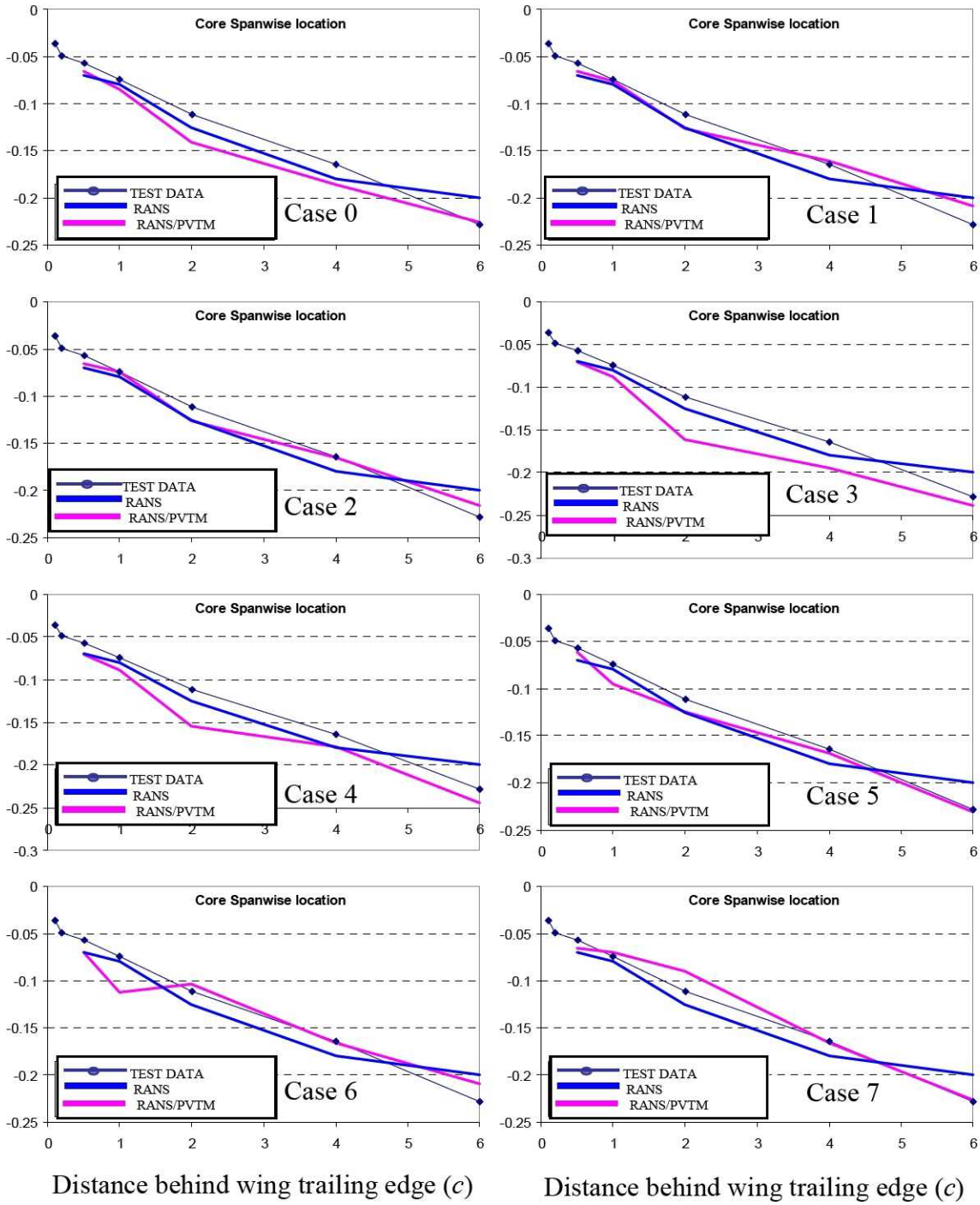

Figure 4.12: Comparison of tip vortex core spanwise location

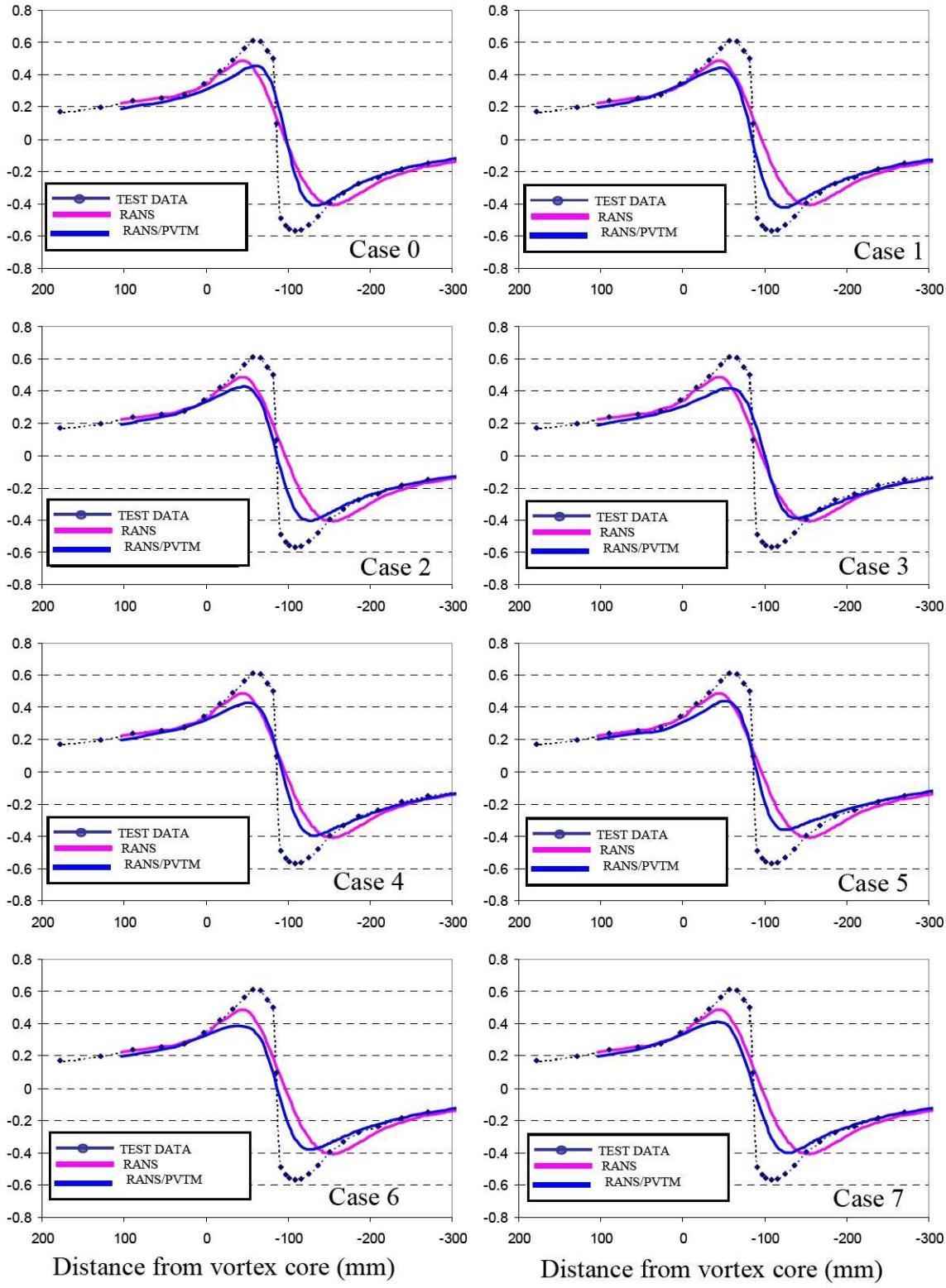

Figure 4.13: Comparison of tip vortex swirl velocity (V_z/V_∞) at 4 chords behind the wing

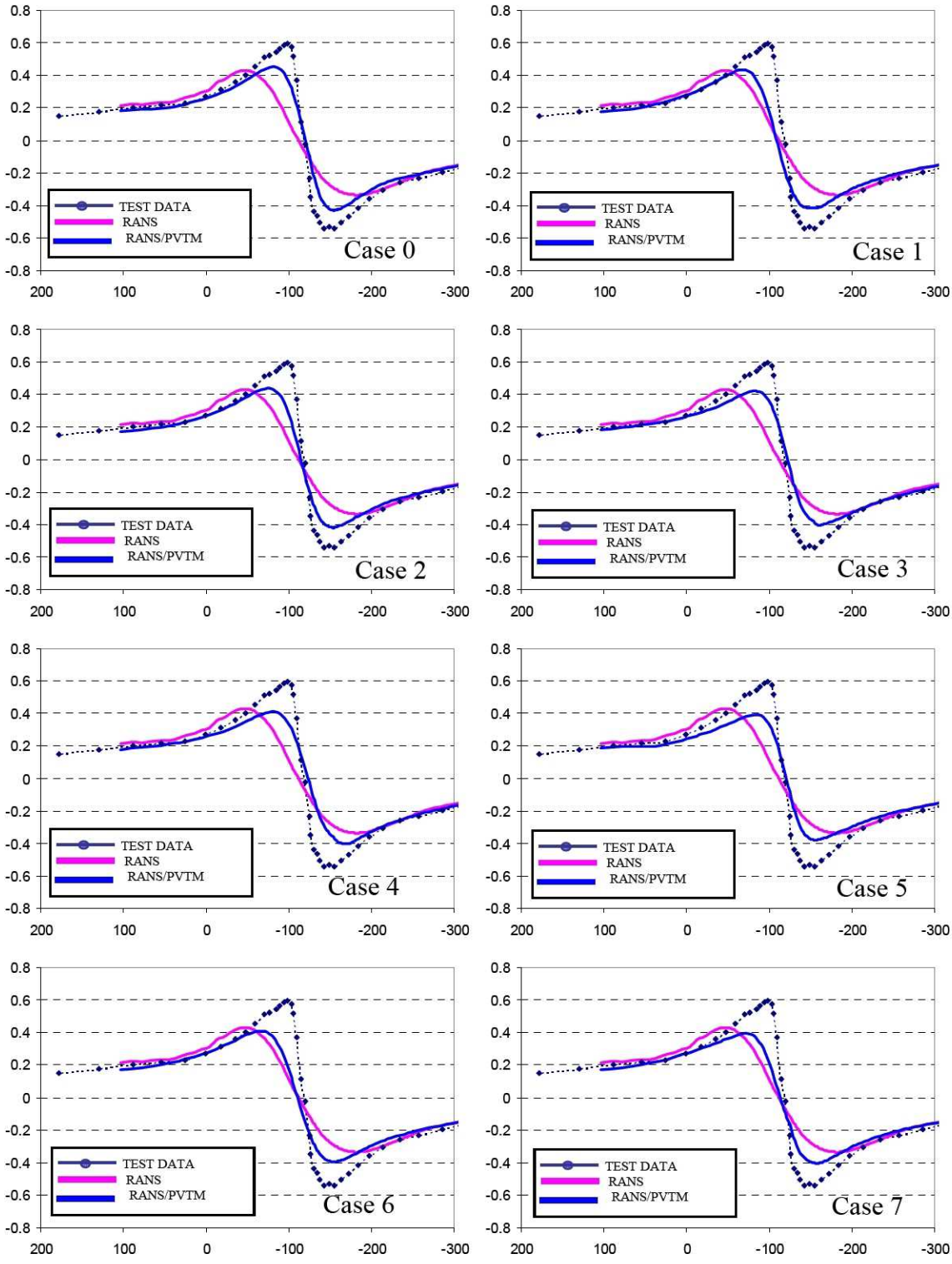

Figure 4.14: Comparison of tip vortex swirl velocity (V_z/V_∞) at 6 chords behind the wing

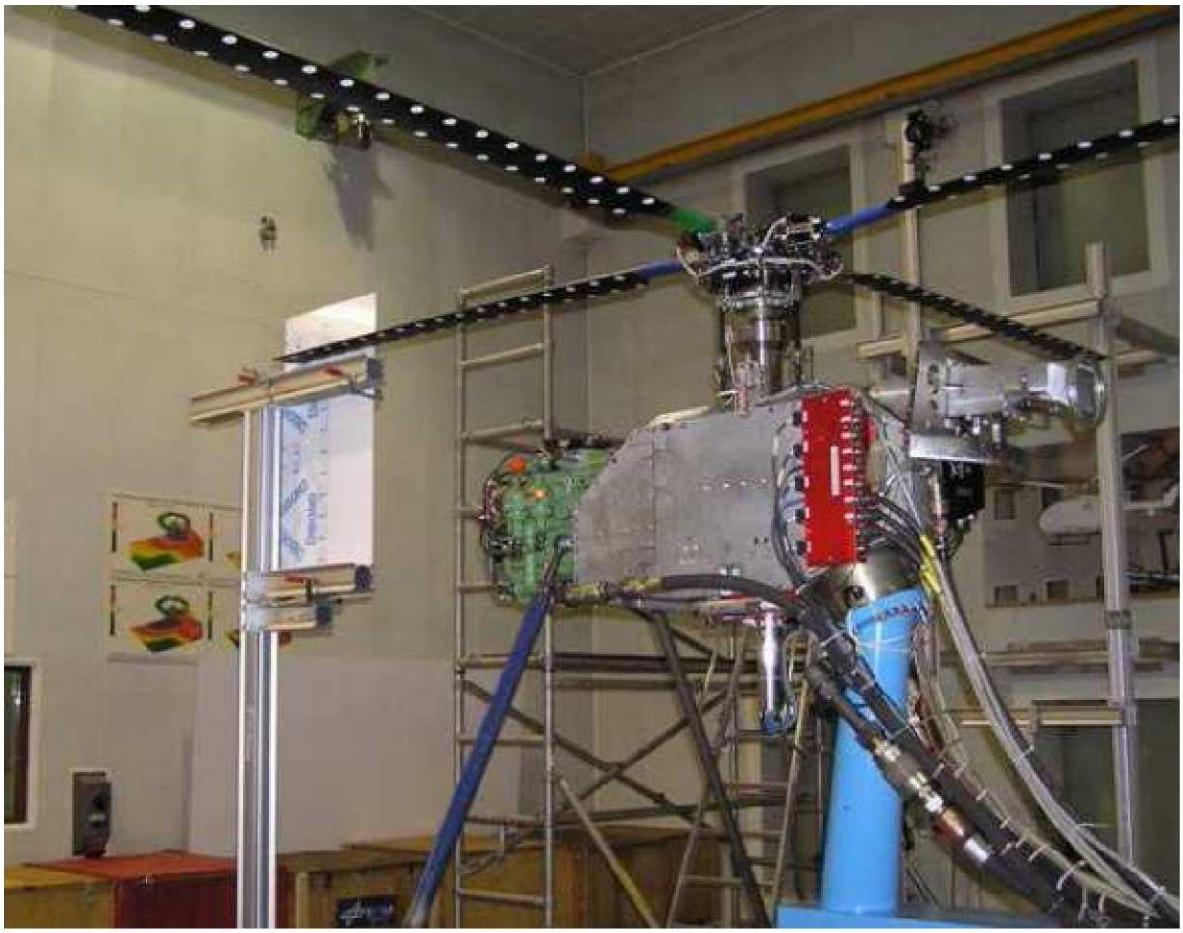

Figure 5.1: HOTIS test configuration (from Ref. [5.1])

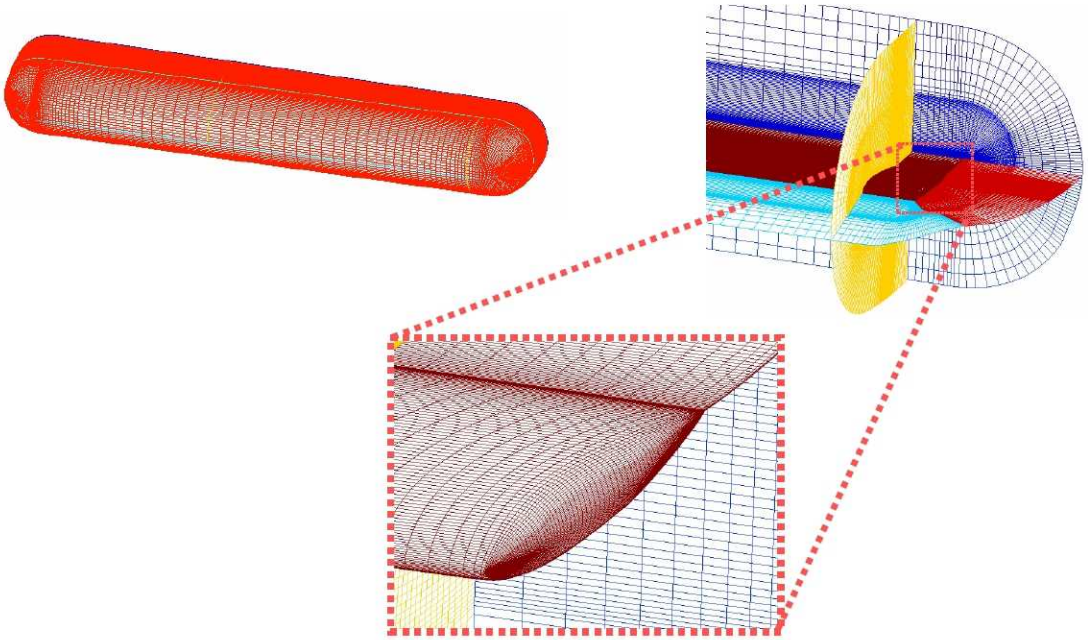

Figure 5.2 RANS grid for one of HOTIS blades

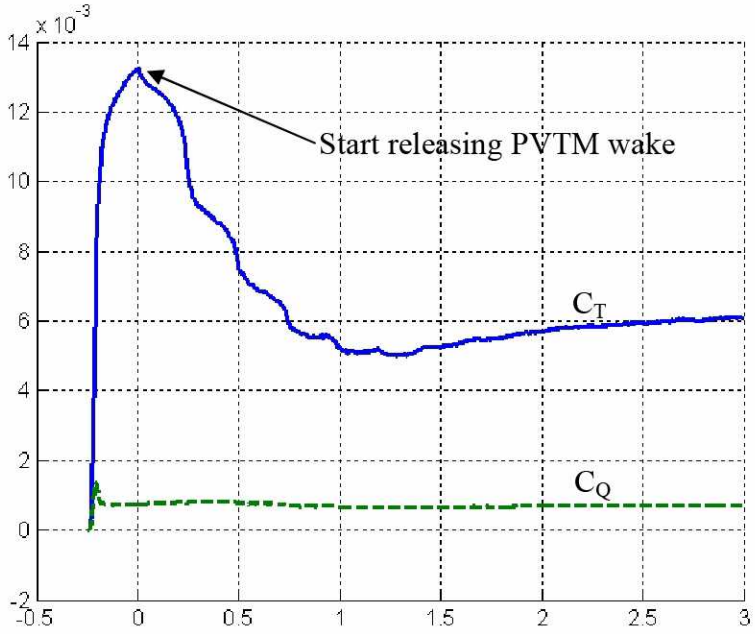

Figure 5.3: Rotor loading (untrimmed HOTIS, 3 revs)

Figure 5.4: Vorticity isosurface of the PVTM vorticity field (untrimmed HOTIS, 3 revs)

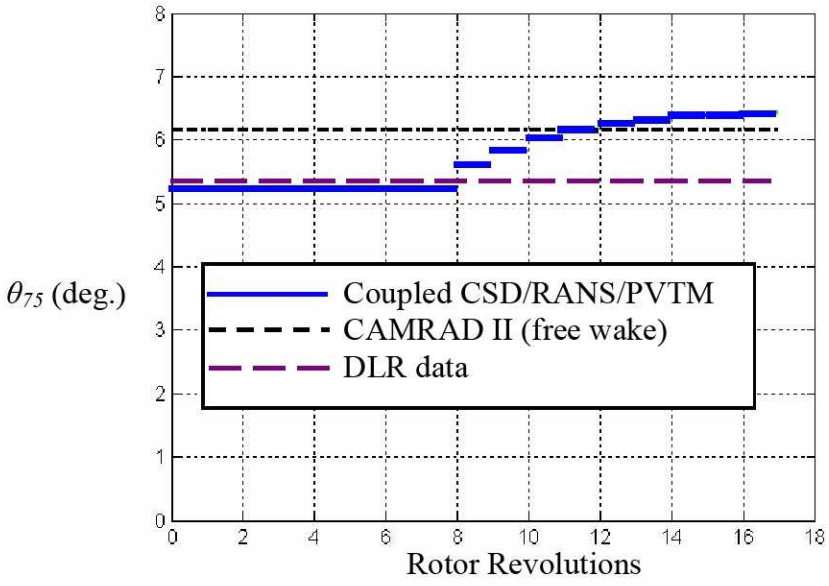

Figure 5.5: Variation of trim parameter, θ_{75}, for loose coupling results for HOTIS rotor

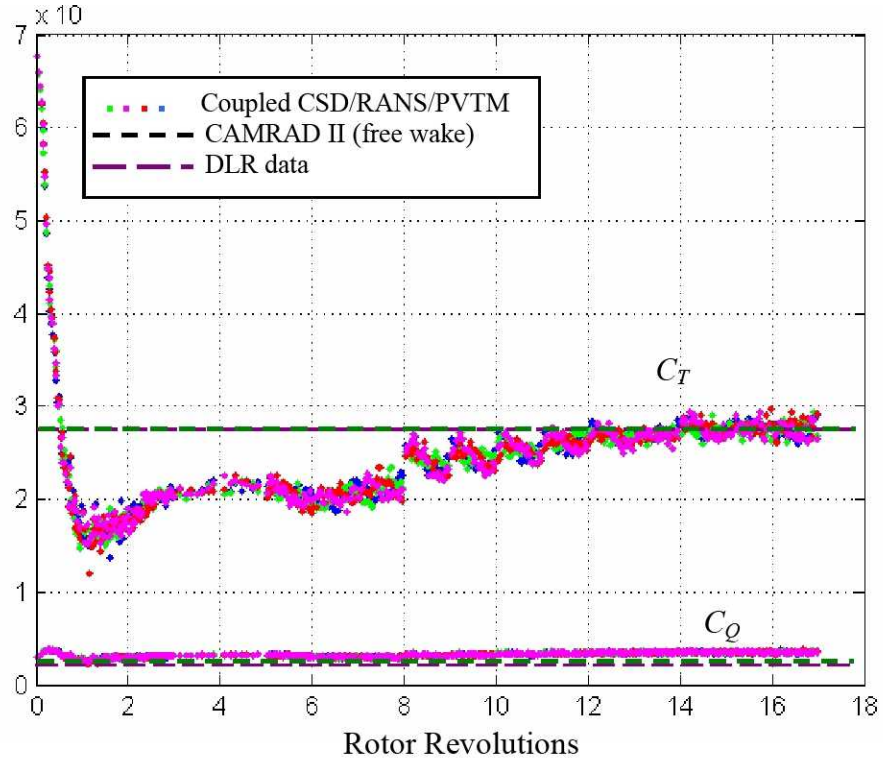

(a) Individual blade

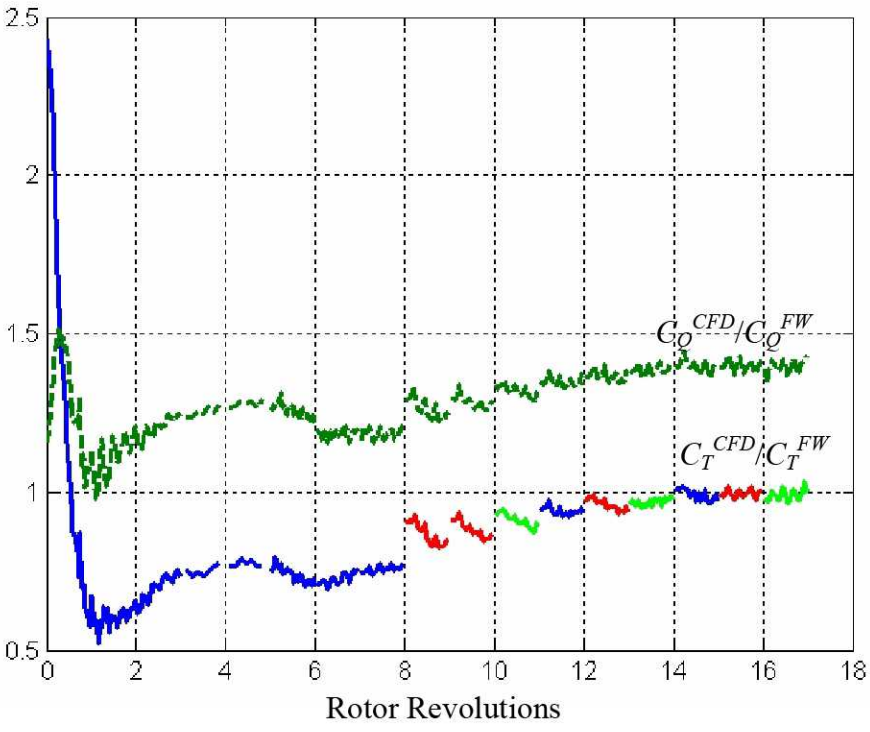

(b) Rotor system

Figure 5.6: Variation in CFD loadings (C_T and C_Q) for HOTIS rotor in hover

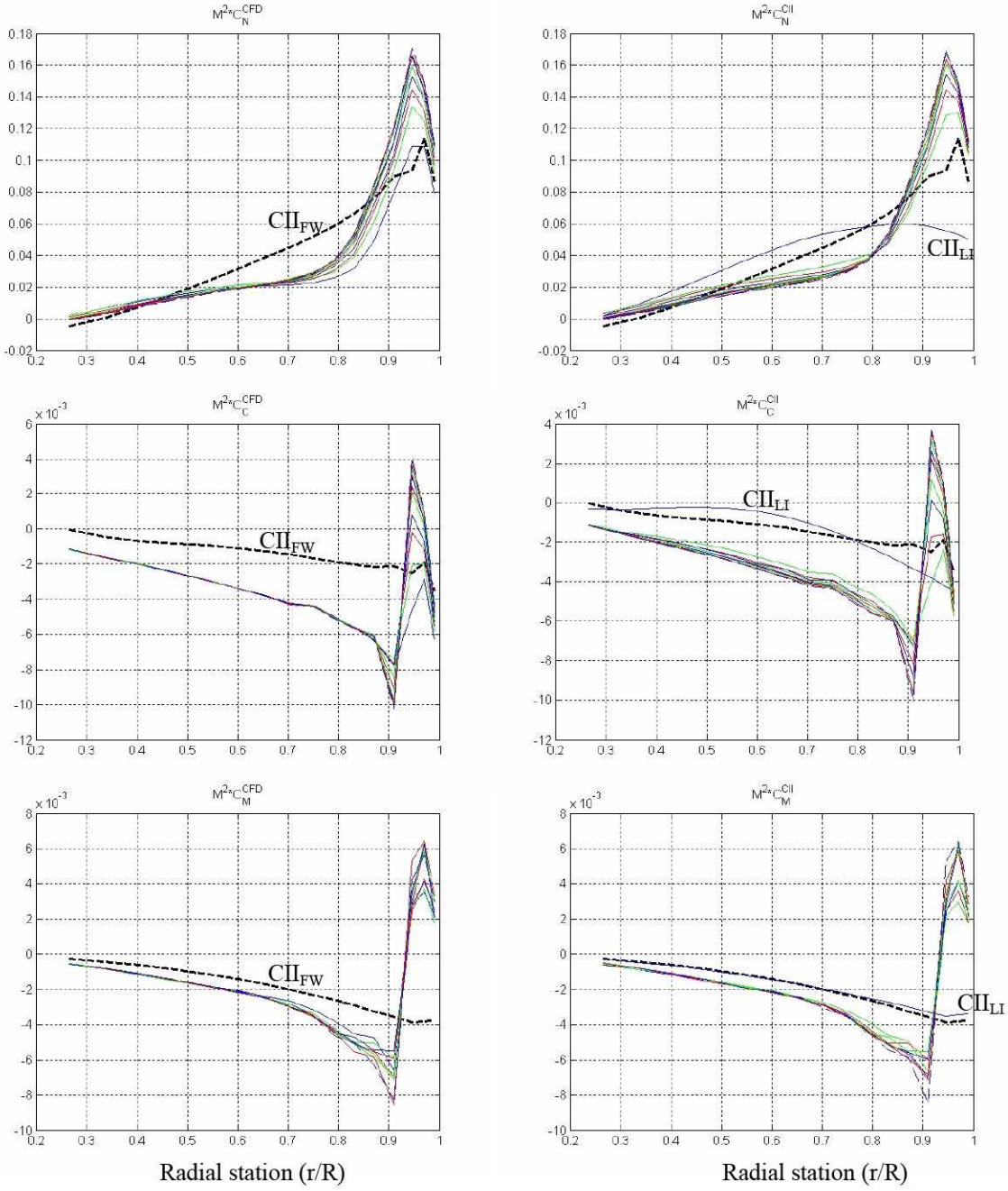

Figure 5.7: Comparisons of blade loading from CFD and CSD analyses during 9 trim iterations [Free wake (FW) and linear inflow (LI) values are added for completeness]

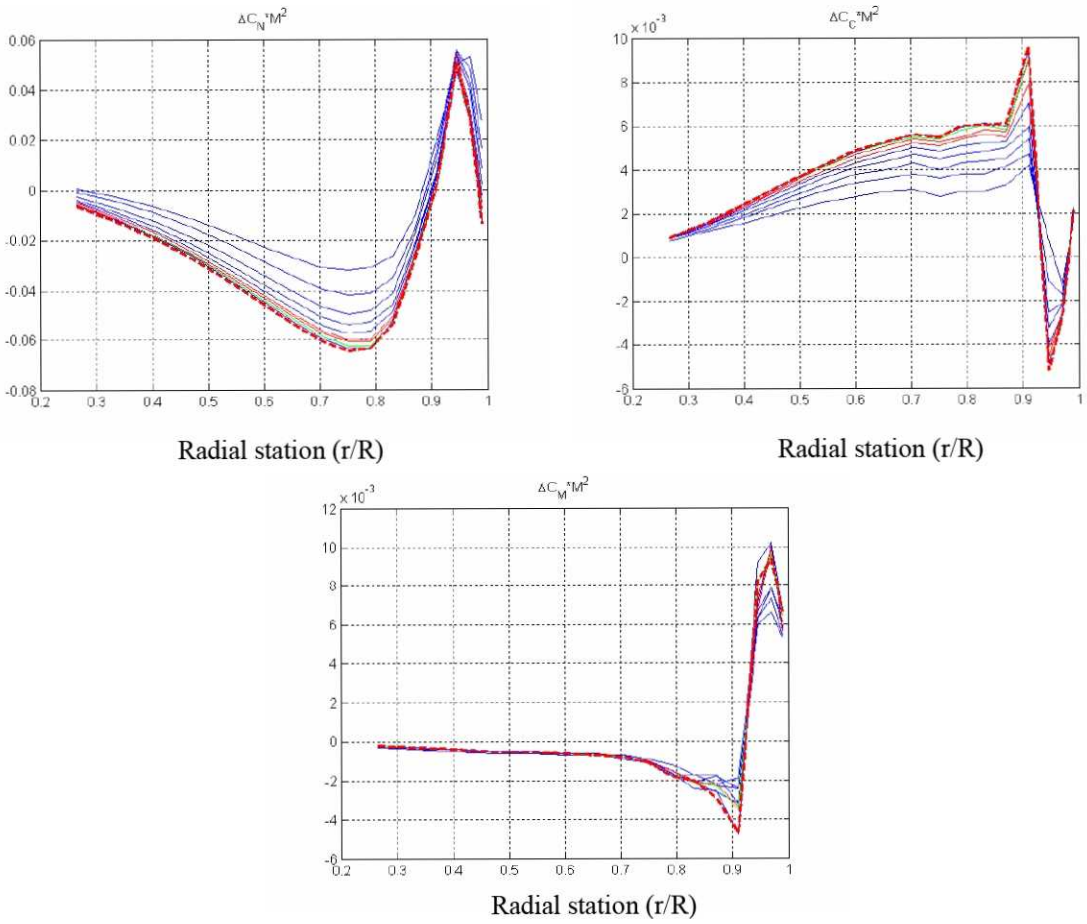

Figure 5.8: Comparisons of "Delta loading" during nine trim iterations (e.g. $\Delta C_N = C_N^{CFD} - C_N^{LI}$)

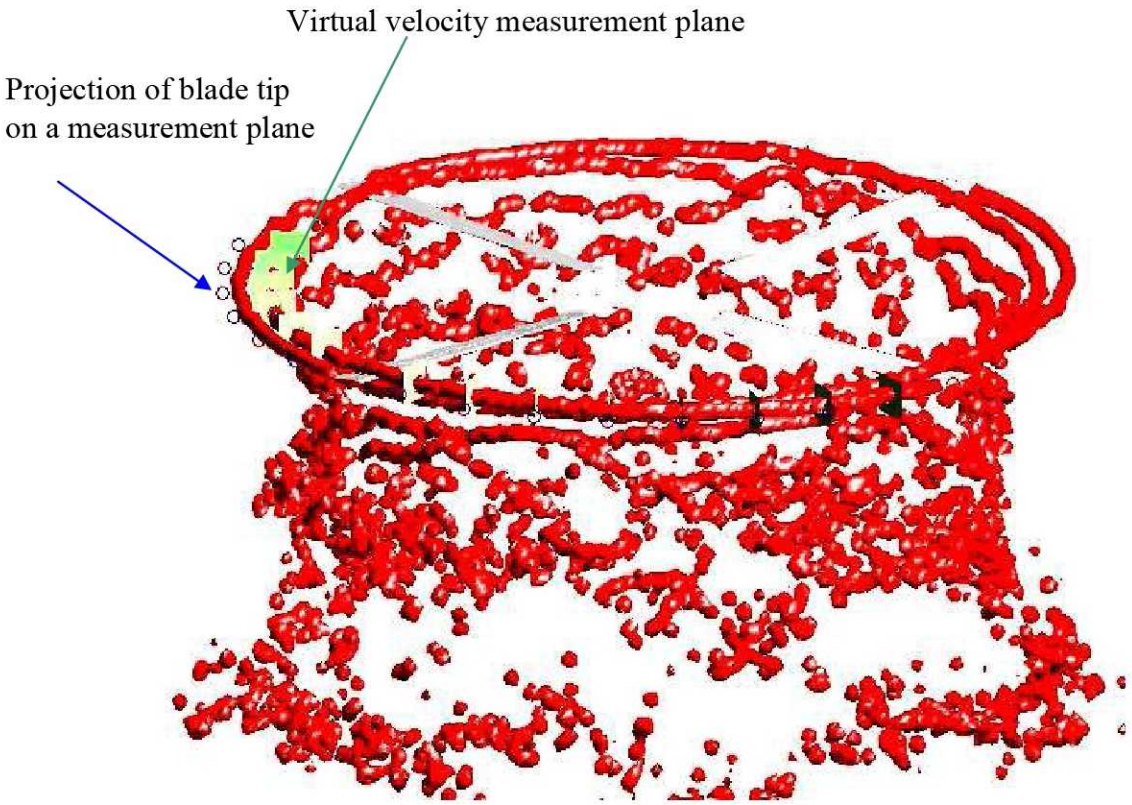

(a) Coupled RANS/PVTM/CSD result

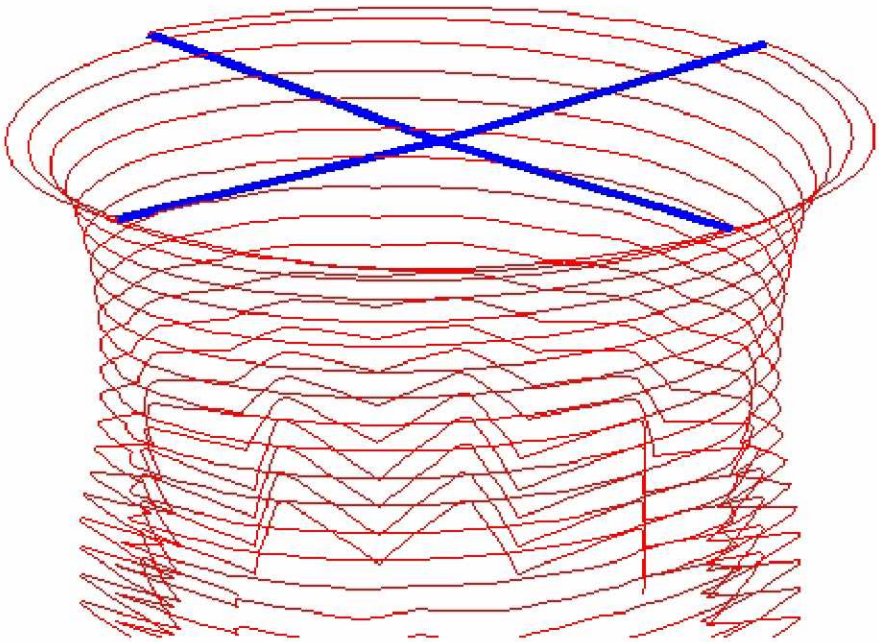

(b) CAMRAD II (free wake) result

Figure 5.9: Vorticity field from the converged HOTIS results

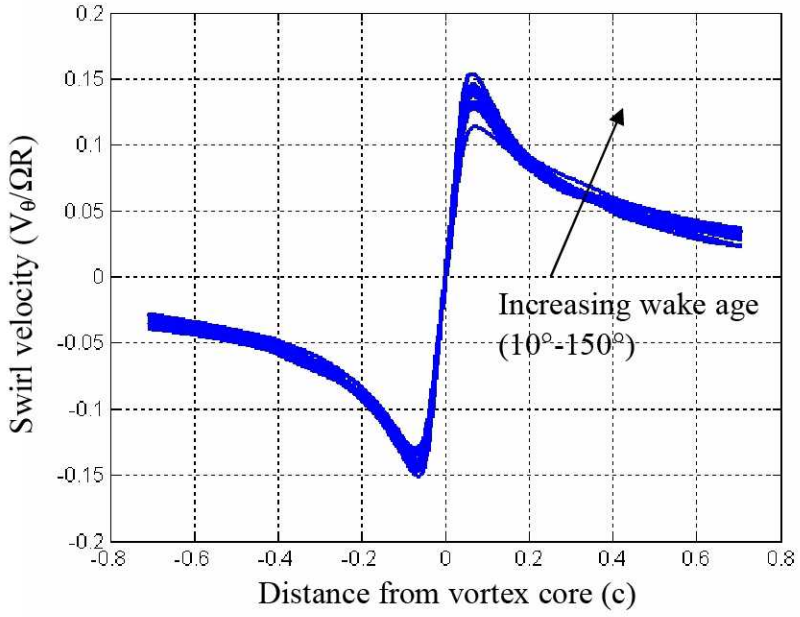

(a) PVTM results

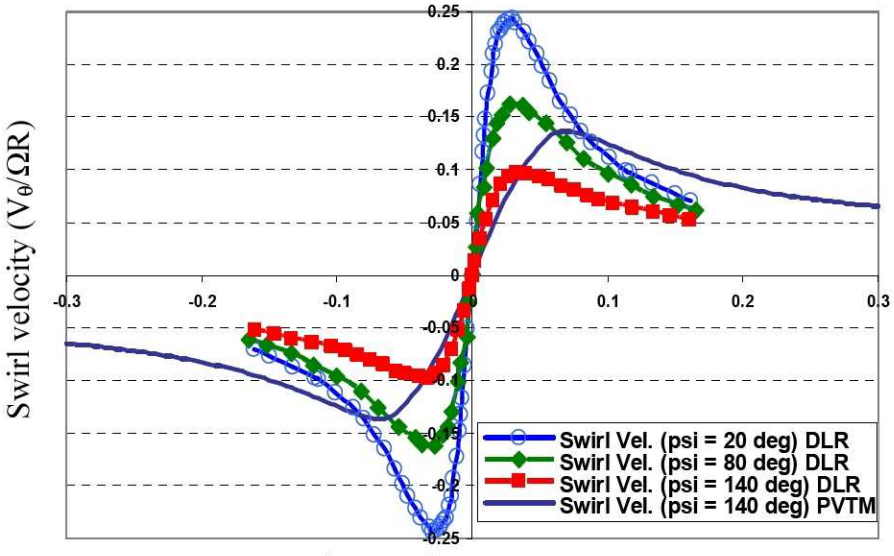

(b) Comparison with DLR data

Figure 5.10: Tip vortex swirl velocity: (a) converged RANS/PVTM/CSD results and (b) comparison with DLR data

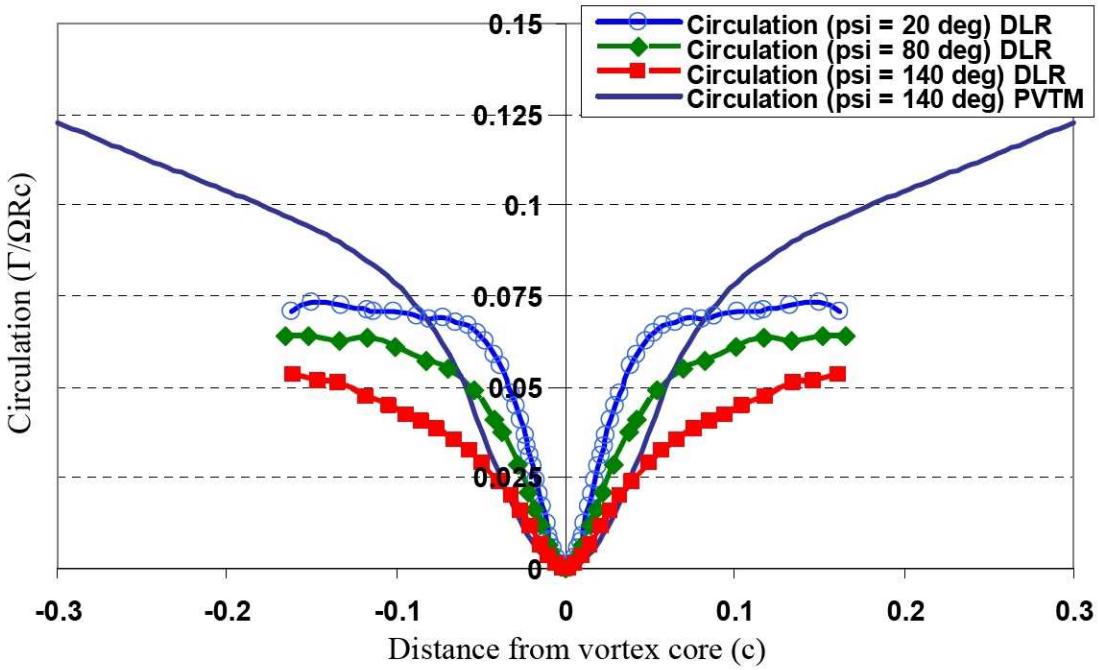

(a) tip vortex circulation ($\Gamma = \int V_\theta dl = \int V_\theta r\, d\theta$)

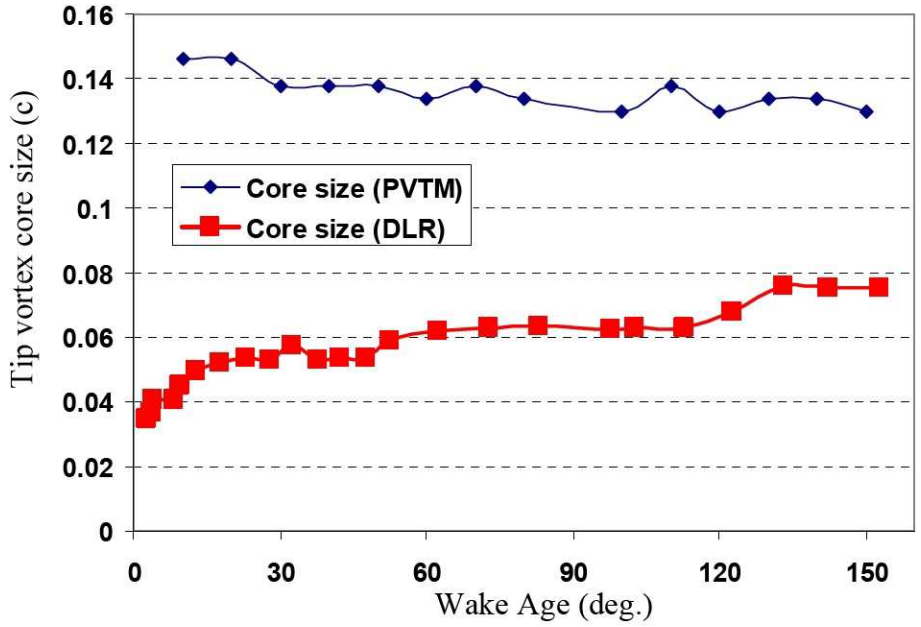

(b) tip vortex core seize

Figure 5.11: Comparisons of (a) tip vortex circulation and (b) tip vortex core size

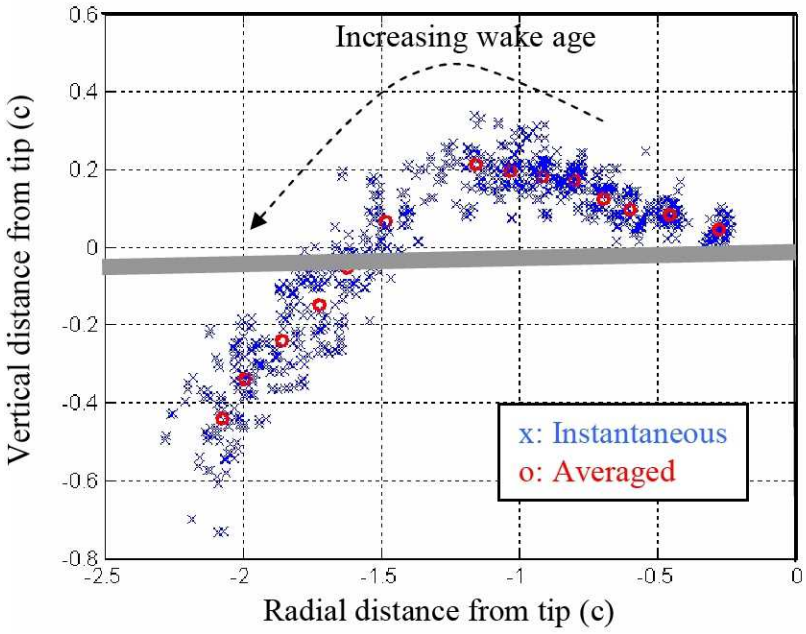

(a) RANS/PVTM/CSD result

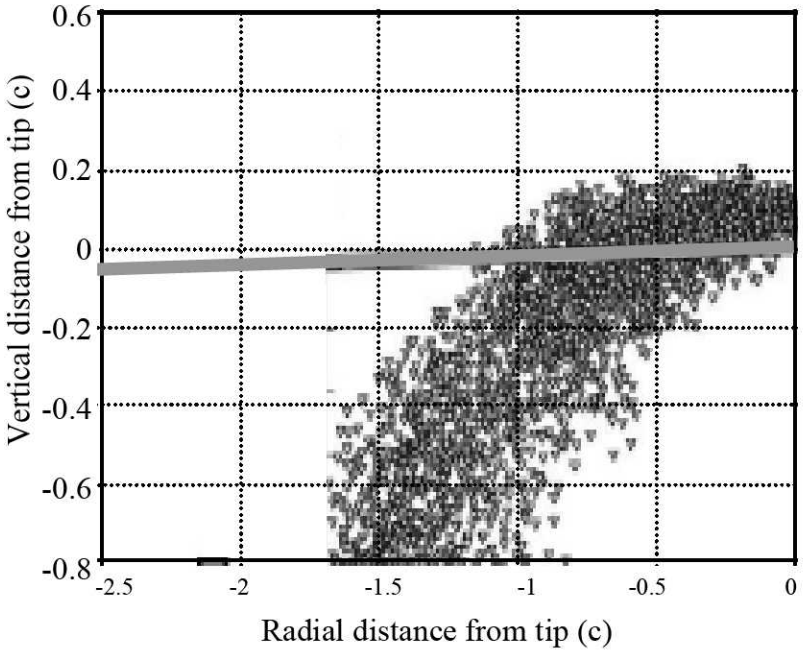

(b) DLR data (from Ref. [5.1])

Figure 5.12: Tip vortex trajectory from (a) RANS/PVTM/CSD result and (b) DLR data

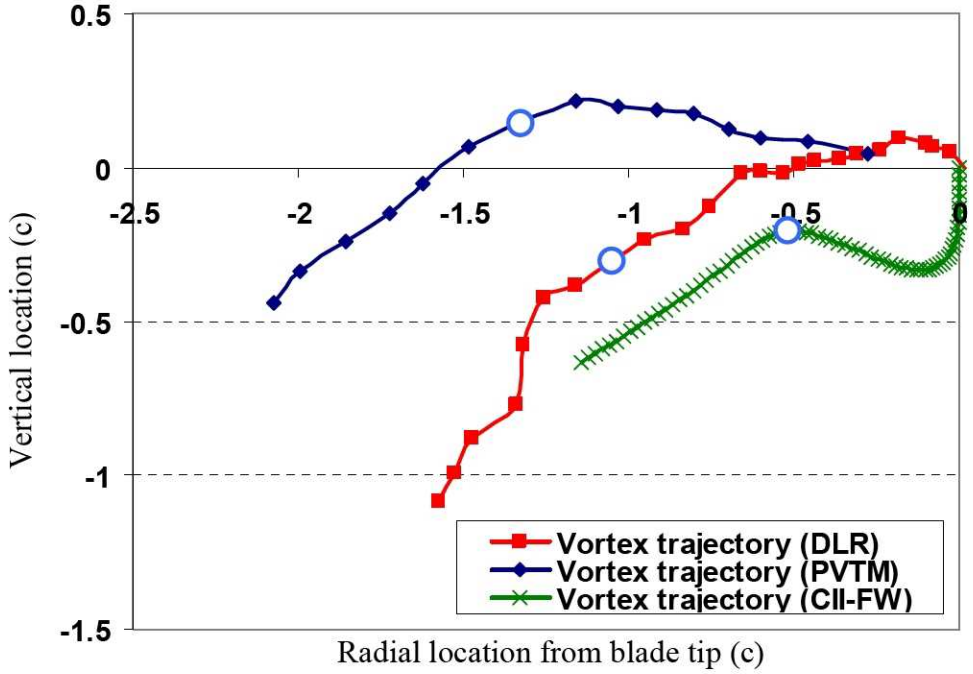

Figure 5.13: Comparison of tip vortex trajectory (0°-150° wake age, **O**: indicates the first blade passage of 90°)

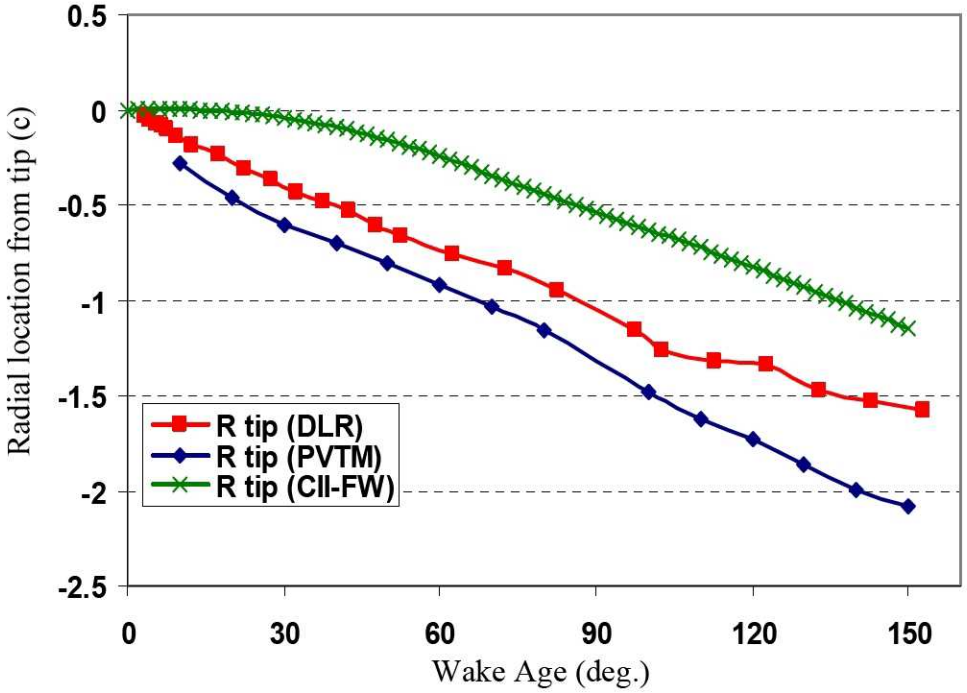

(a) Radial location from tip (c)

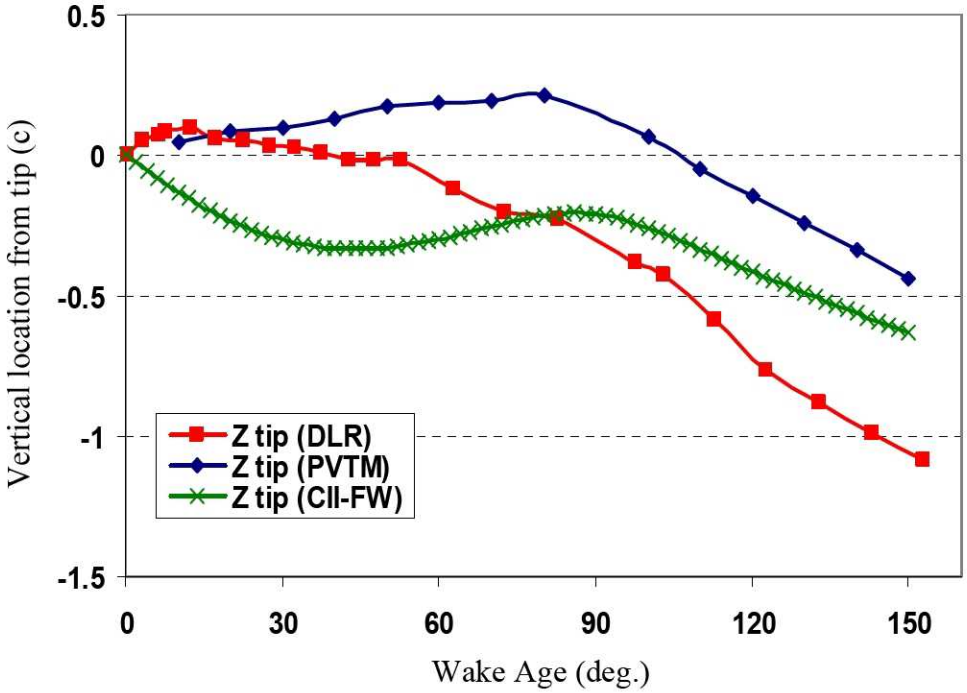

(b) Vertical location from tip (c)

Figure 5.14: Comparison of tip vortex location (0°-150° wake age)

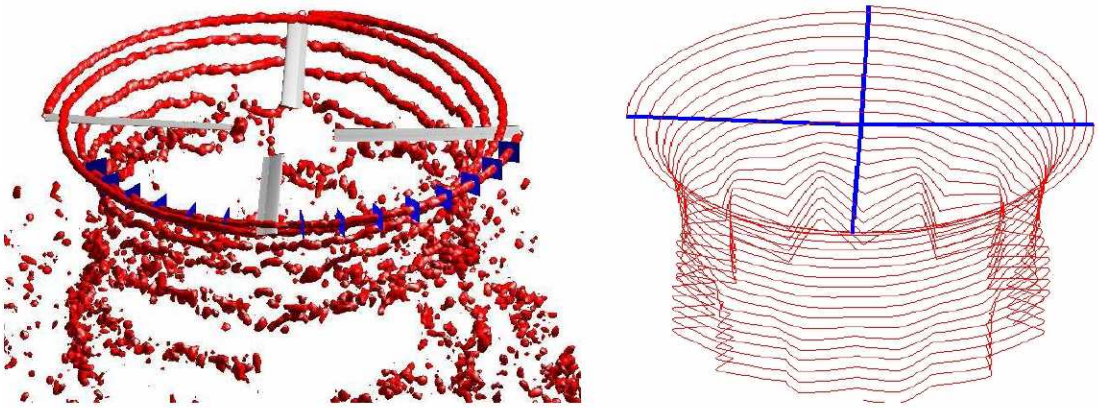

(a) Dynamic PVTM (b) CAMRAD II (free wake)

Figure 5.15: Comparison of vorticity field: dynamic PVTM and CII-FW

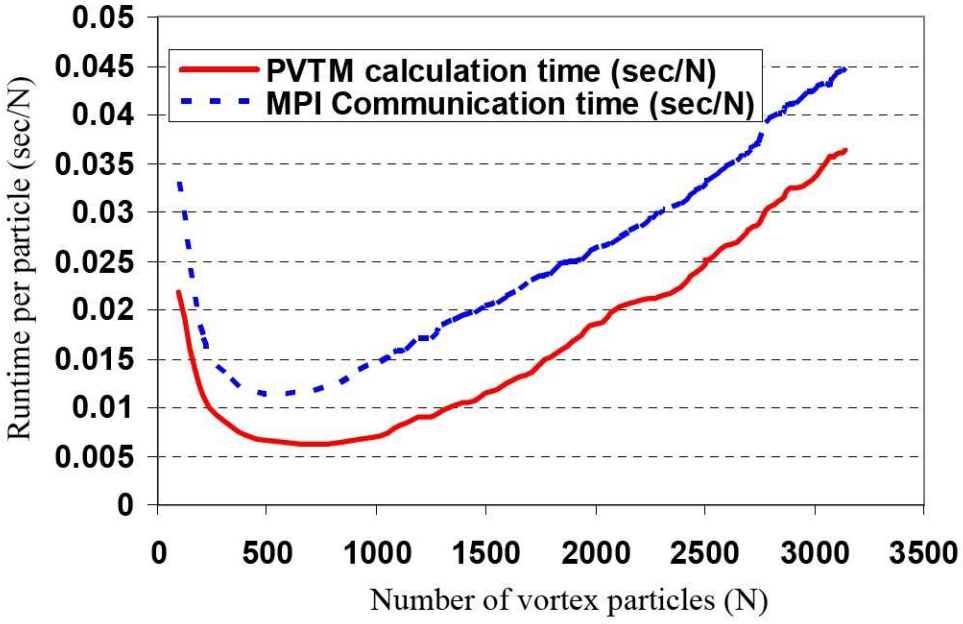

Figure 5.16: Runtime for dynamic PVTM

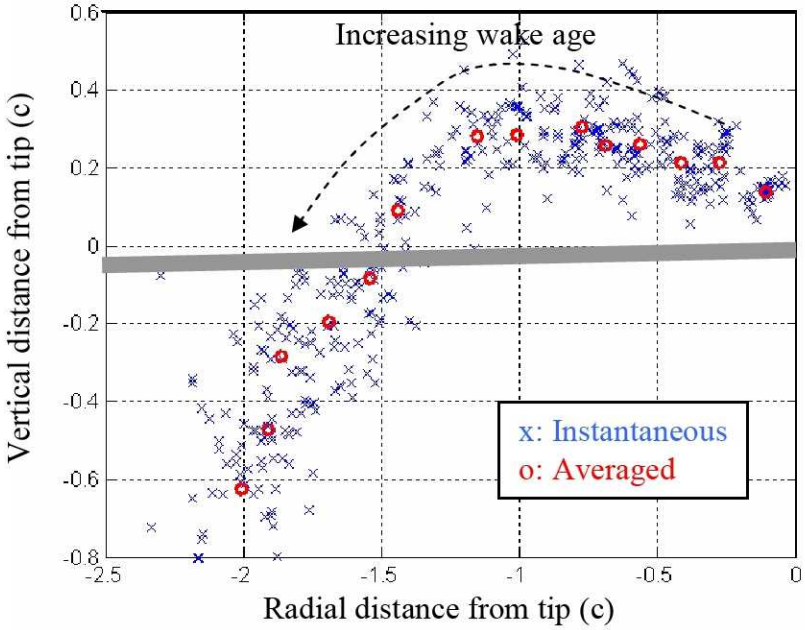

(a) Dynamic PVTM

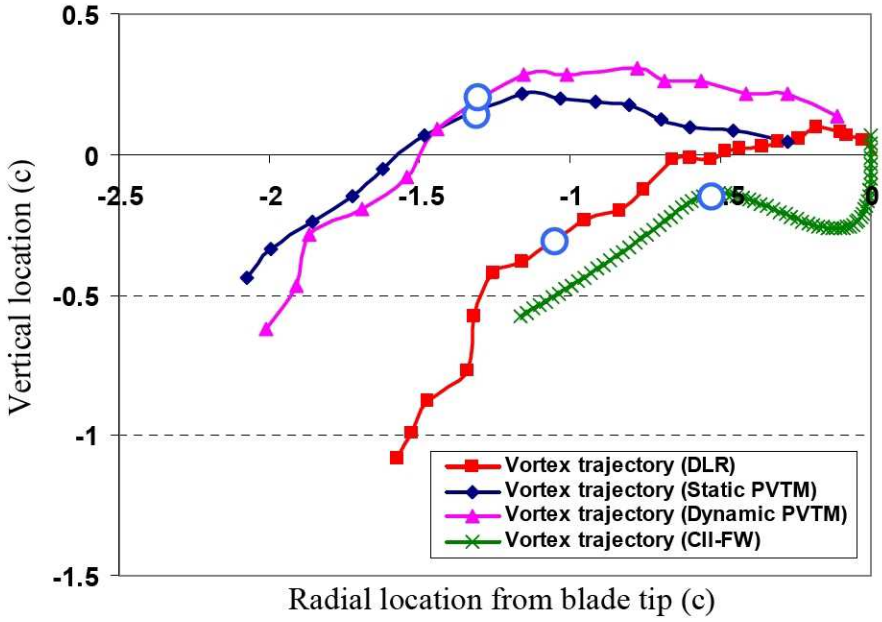

(b) Comparison with other results and data (O: indicates the first blade passage of 90°)

Figure 5.17: Tip vortex trajectory from RANS/PVTM/CSD result (dynamic PVTM)

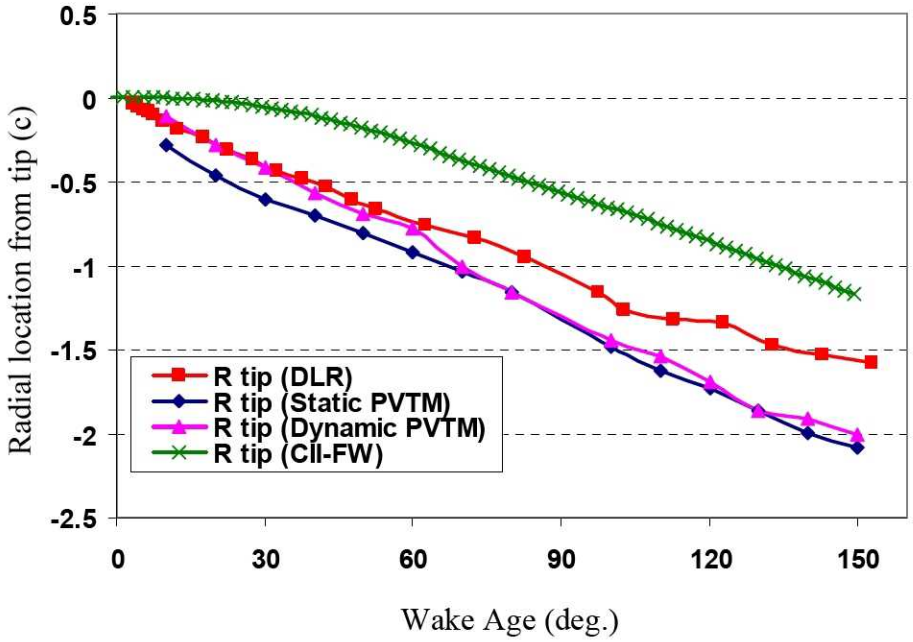

(a) Radial location from tip (c)

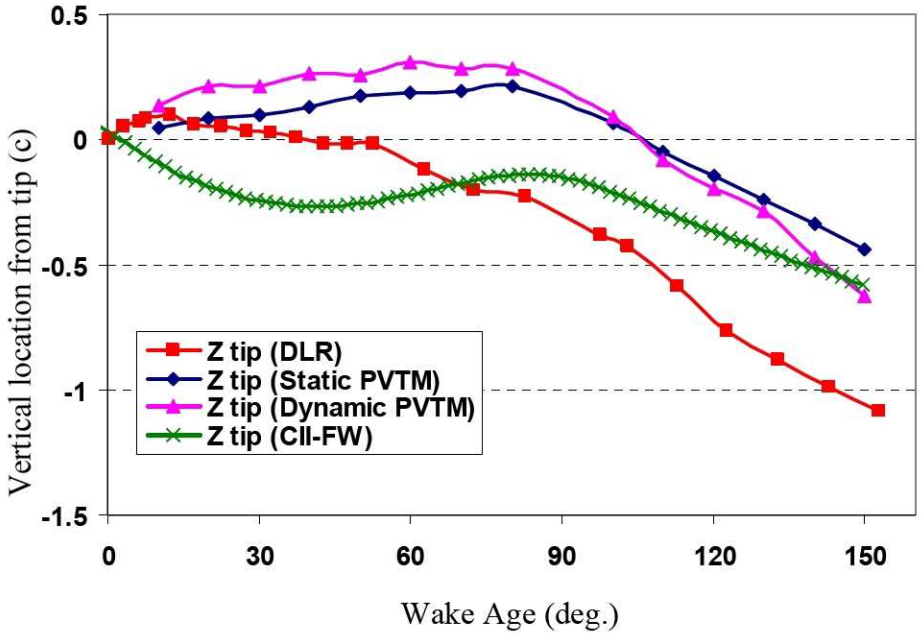

(b) Vertical location from tip (c)

Figure 5.18: Comparison of tip vortex location (Dynamic PVTM)

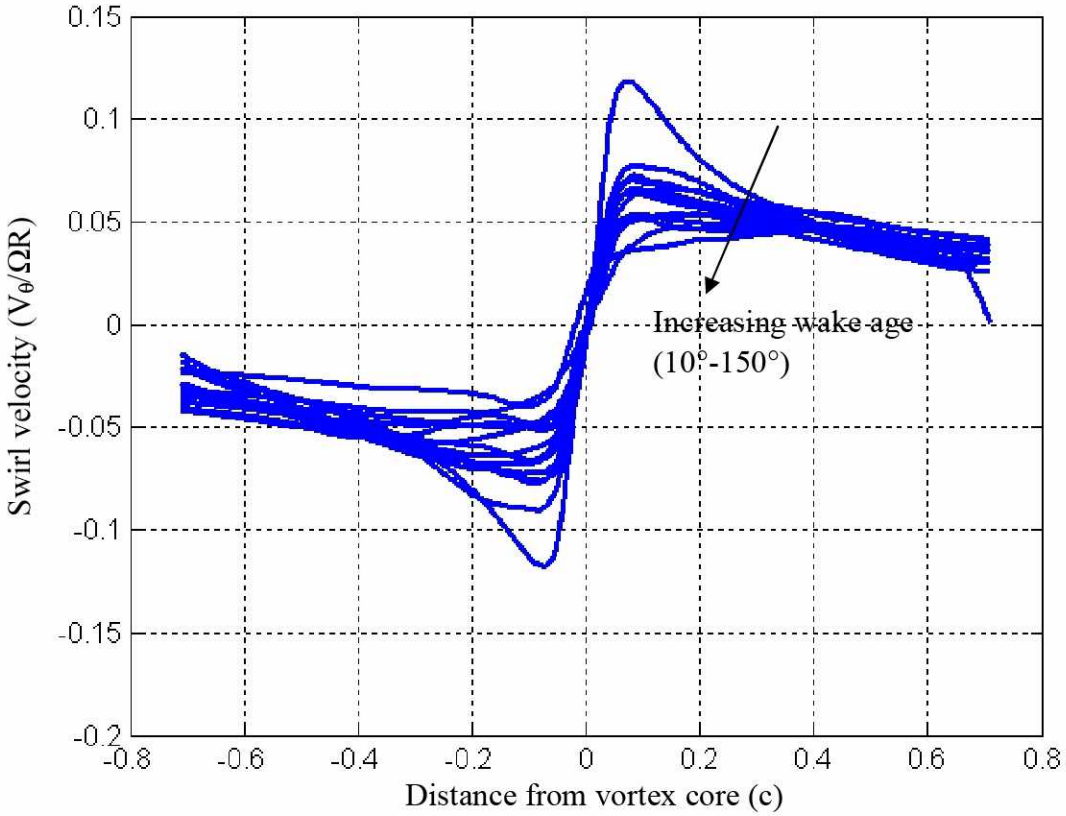

Figure 5.19: Tip vortex swirl velocity from converged RANS/PVTM/CSD result (Dynamic PVTM)

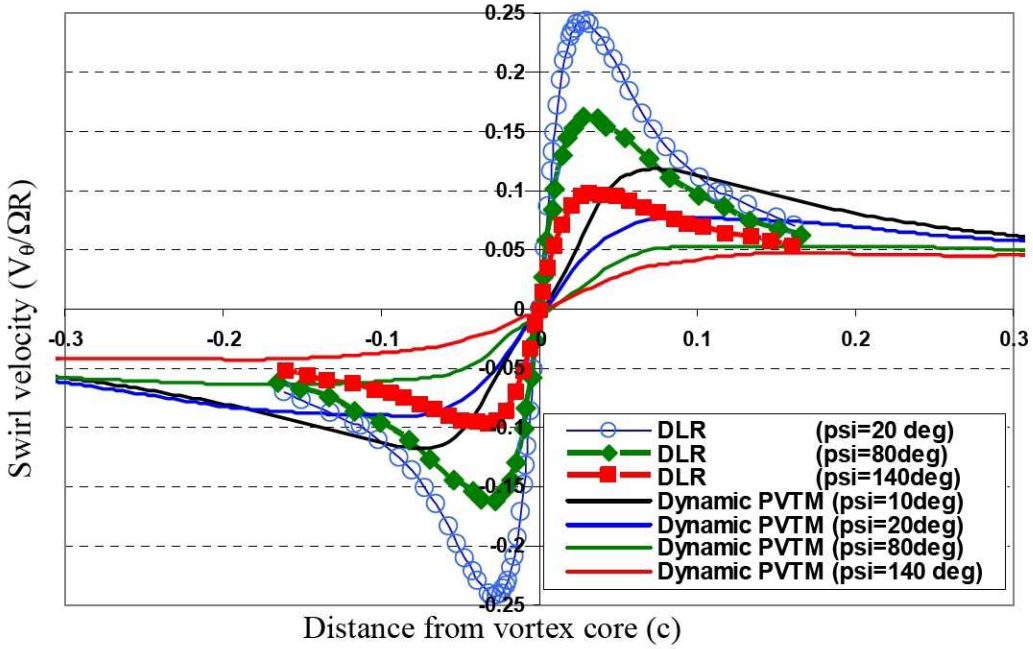

Figure 5.20: Comparisons of the tip vortex swirl velocity (Dynamic PVTM)

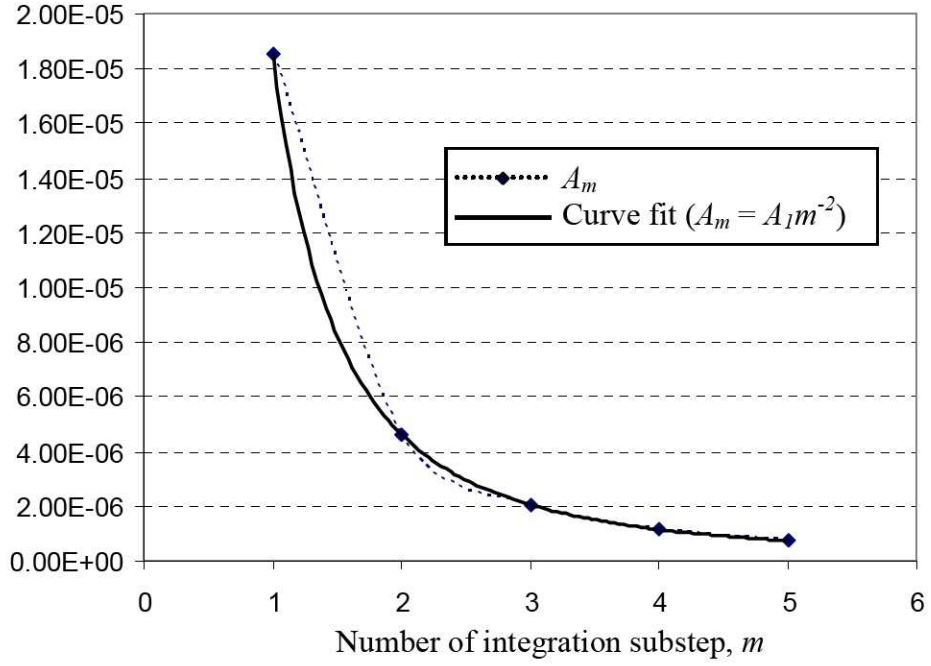

Figure A1: Measure of accuracy, A_m, as a function of number of sub-steps, m

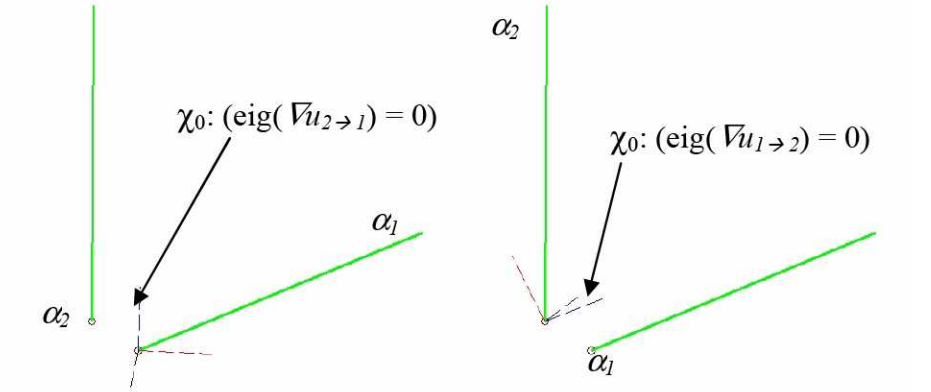

(a) $\nabla u_{2\to 1}$ (b) $\nabla u_{1\to 2}$

Figure B.1: Eigenvectors, χ_0 , associated with λ_0 for the two particles system

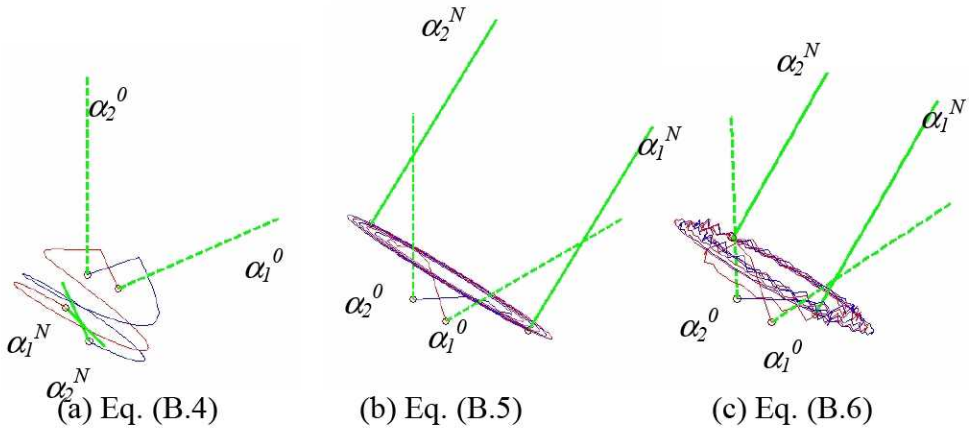

(a) Eq. (B.4) (b) Eq. (B.5) (c) Eq. (B.6)

Figure B.2: Trajectory for a system of two vortex particles using the stretching term from: (a) Eq. B.4, (b) Eq. B.5, and (c) Eq. B.6

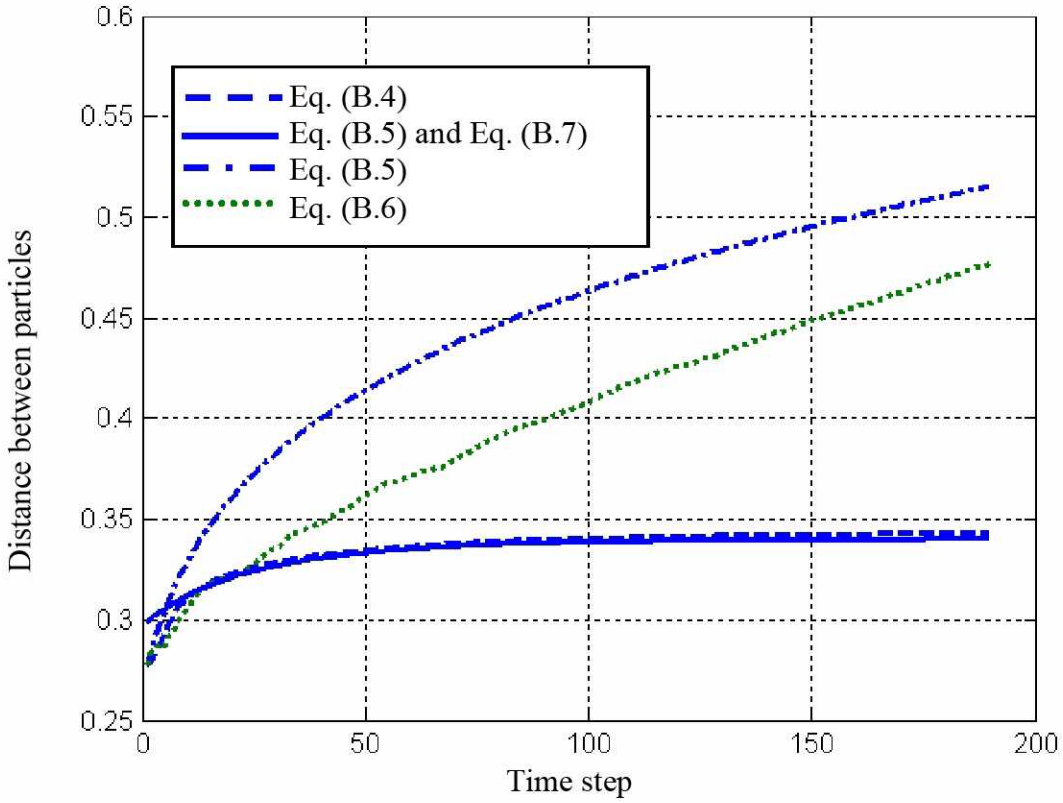

Figure B.3: Distance between the two vortex particles with various stretching model

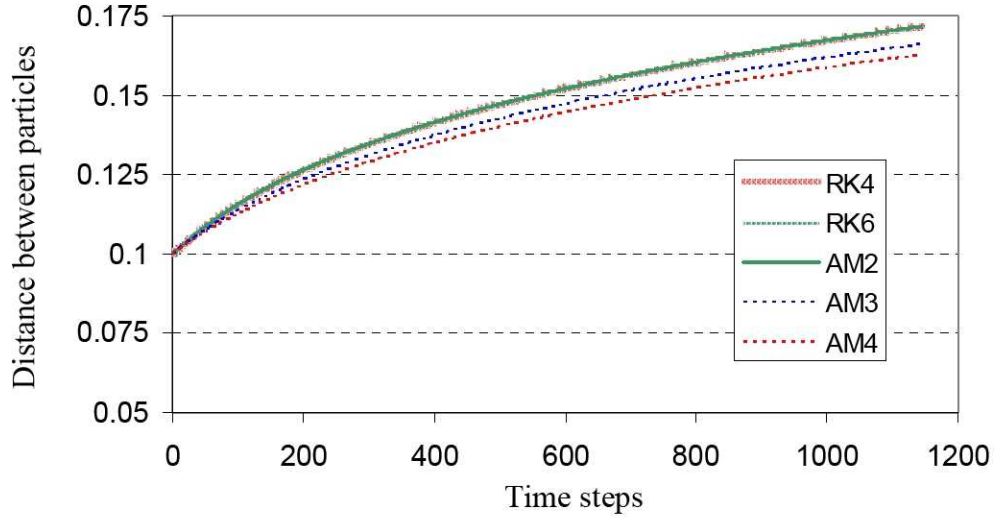

Figure B.4: Comparison of results using explicit and implicit time integration routines

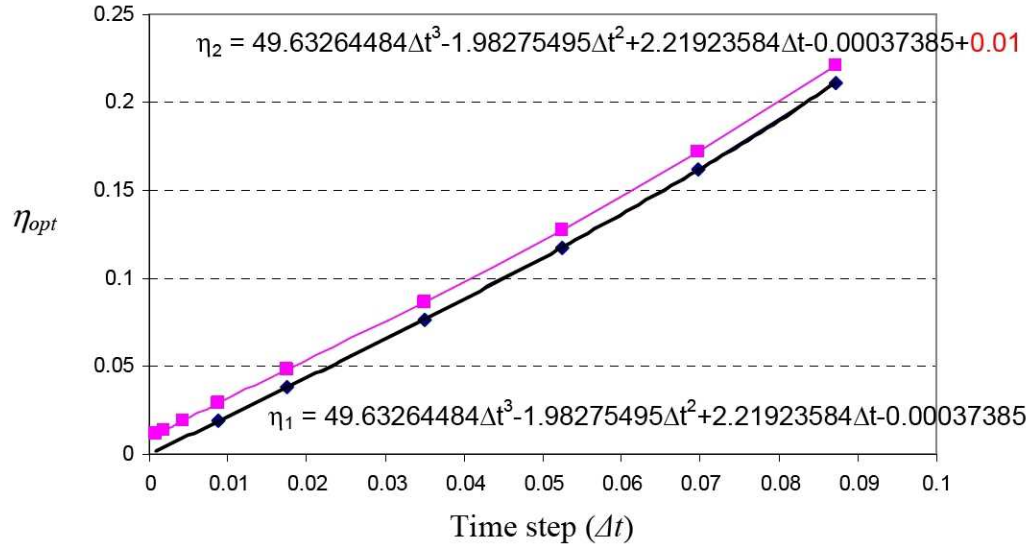

Figure B.5: Optimal attraction coefficient as a function of the time step

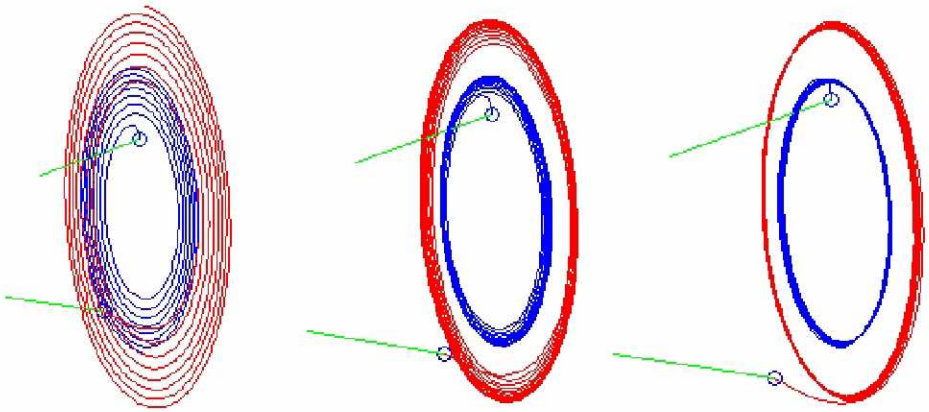

(a) RK6 (b) η_1 (c) η_2

Figure B.6: Trajectory of two vortex particle system: (a) RK6-no attraction term, (b) RK4-η_1 ,(c) RK4-η_2 ($\Delta t = 0.5\pi/180$)

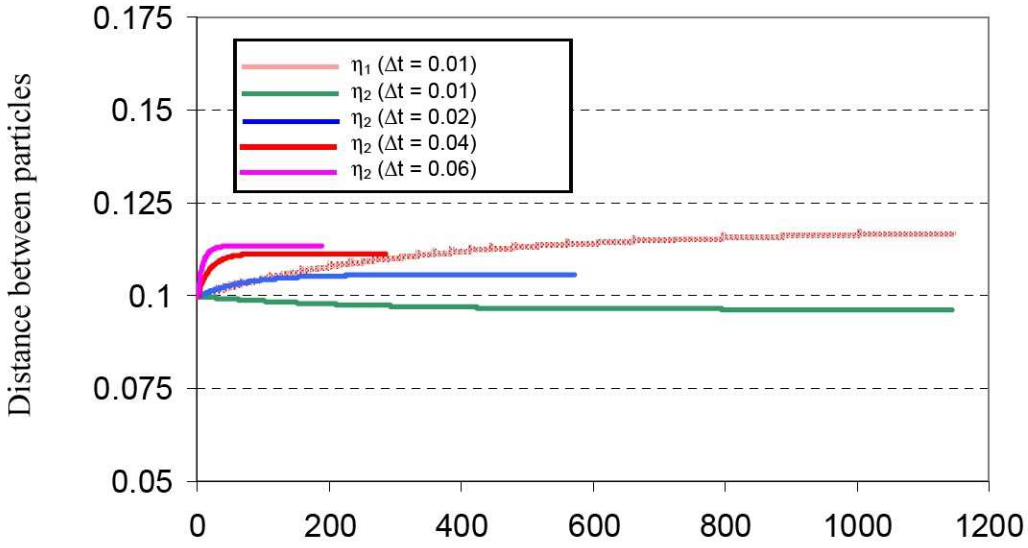

Figure B.7: Comparison of two-particle results with attraction term from η_1 and η_2

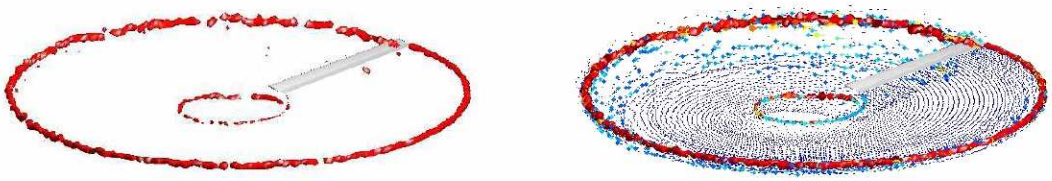

(a) Static PVTM (8178 particles)

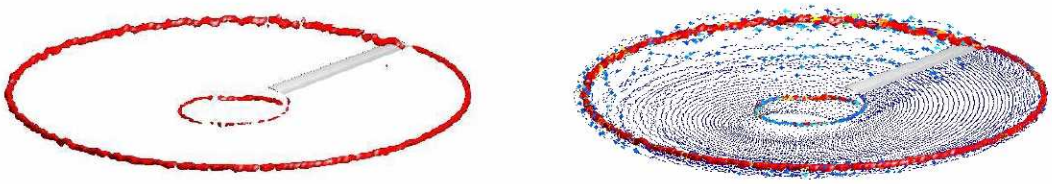

(b) Dynamic PVTM (11161 particles)

Figure C.1: Comparison of vorticity field after 1 rev.: (a) static PVTM and (b) dynamic PVTM (d = 0.2c)

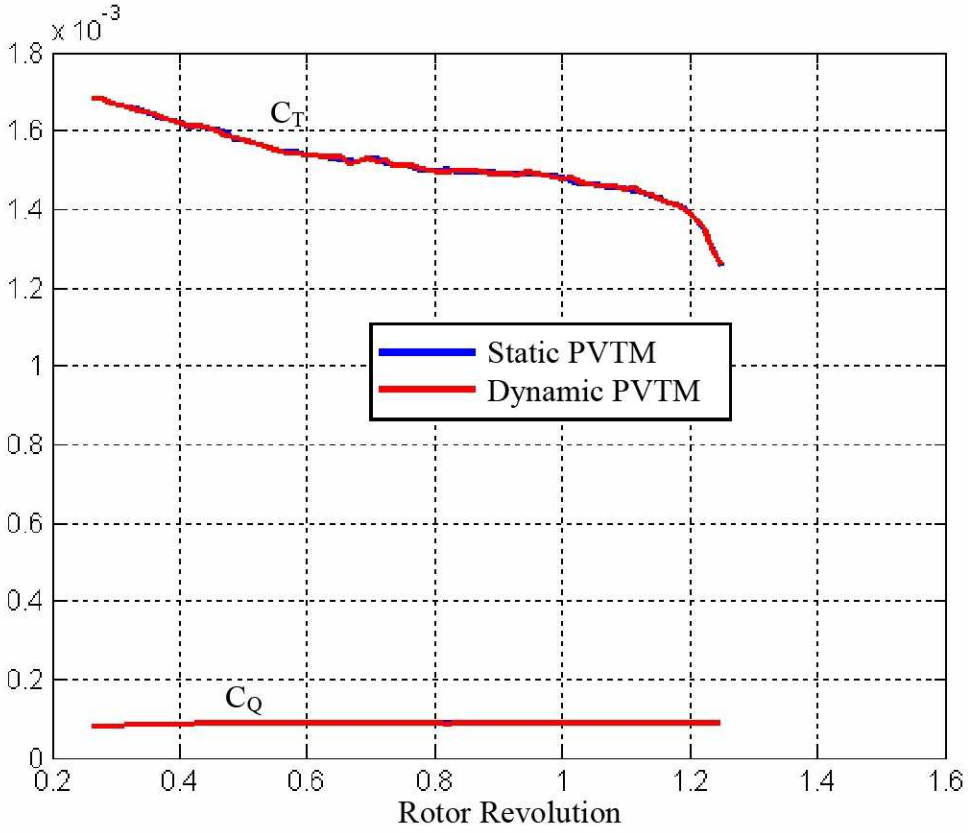

Figure C.2: Comparisons of the blade loading from static and dynamic PVTM

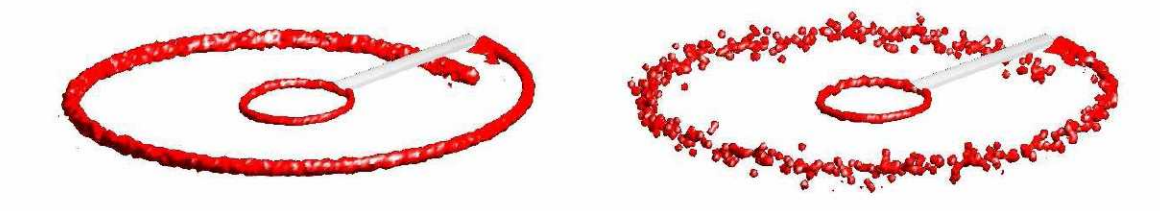

(a) with attraction term (b) without attraction term

Figure C.3: Comparisons of vorticity field from PVTM with and without attraction term

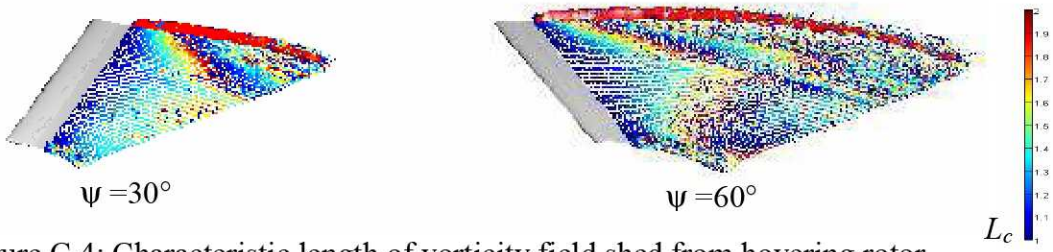

Figure C.4: Characteristic length of vorticity field shed from hovering rotor

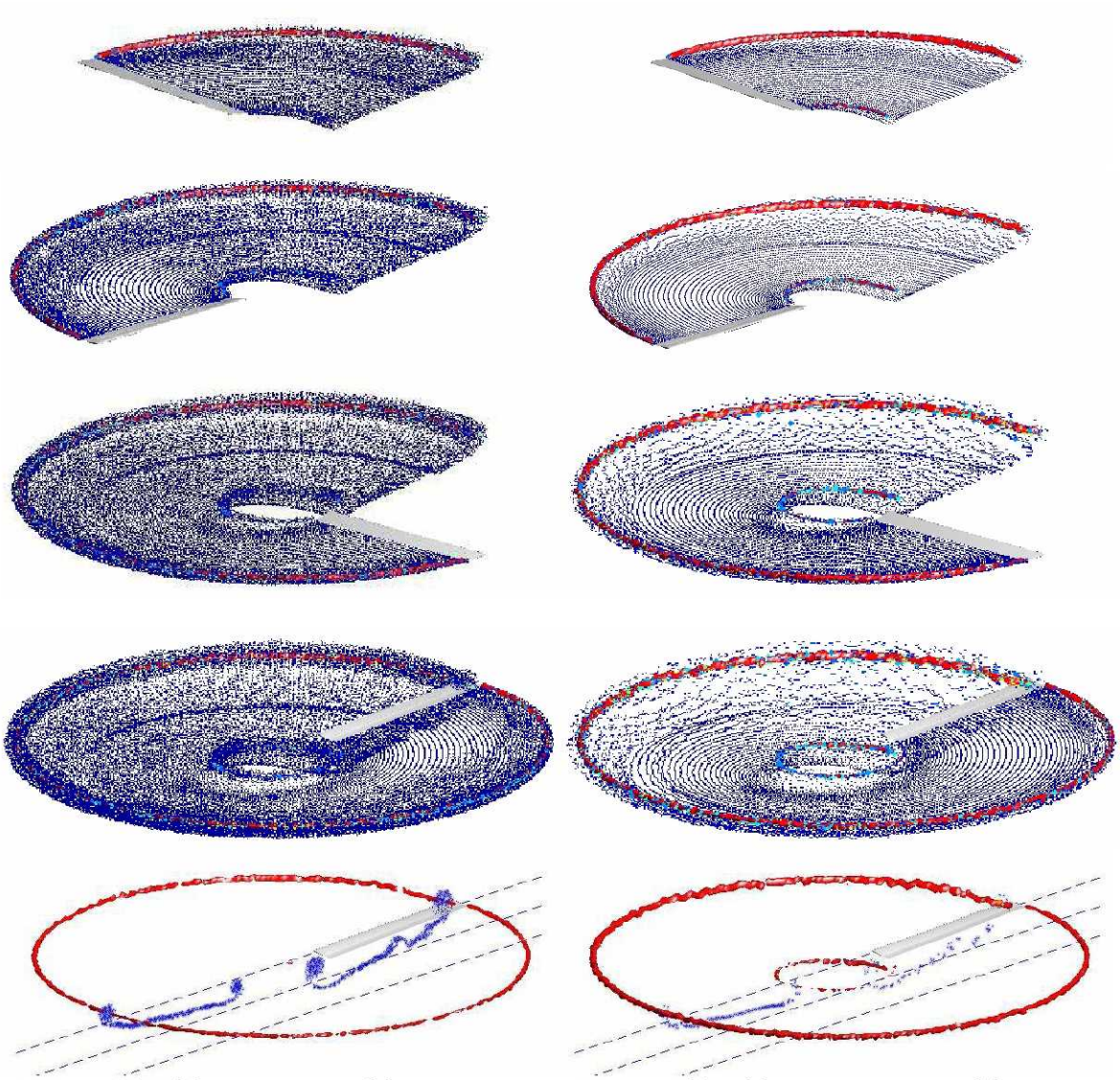

(a) with vortex stretching (b) without vortex stretching

Figure C.5: Evolution of vortex sheet and tip vortex shed from a hovering rotor with and without vortex stretching (d = 0.15c)

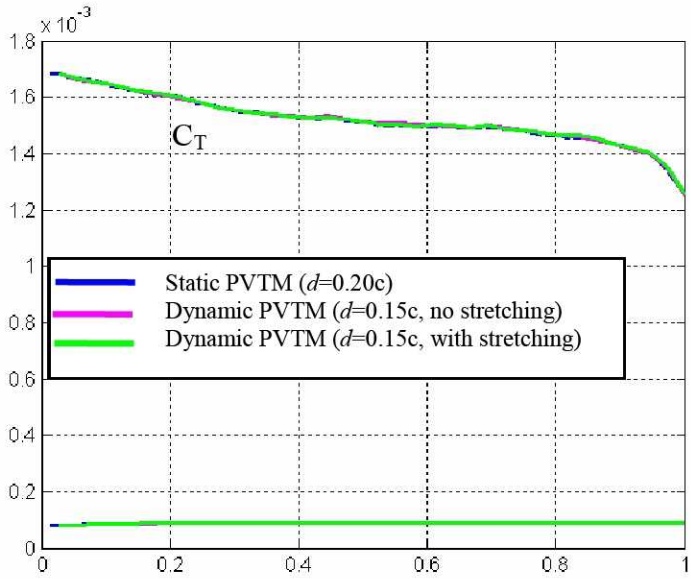

Figure C.6: Comparisons of the blade loading with and without stretching model

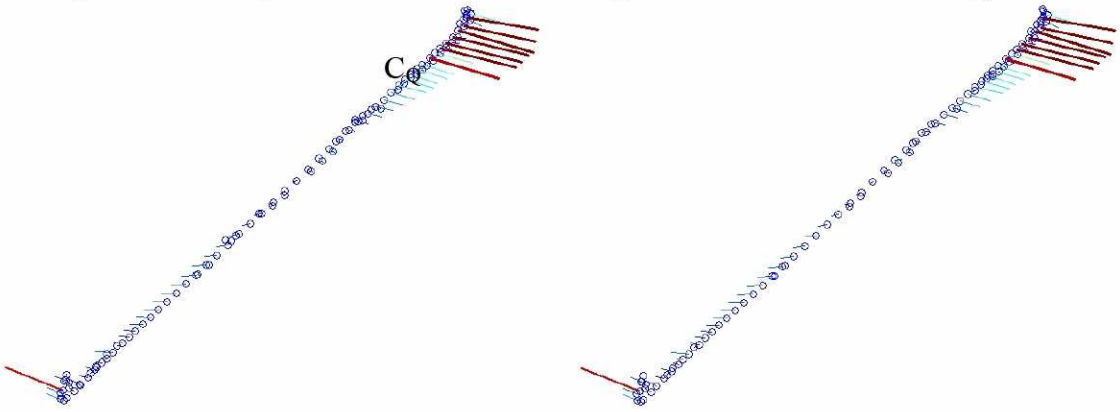

(a) Static PVTM (103 particles) (b) Dynamic PVTM (93 particles)

Figure C.7: Particles released at one time step from HOTIS rotor in hover (d = 0.2c)

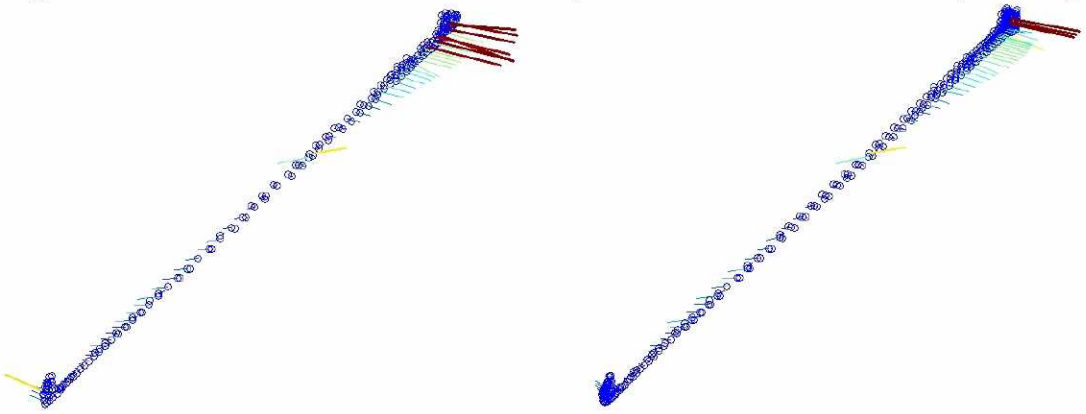

(a) d = 0.1c (191 particles) (b) d = 0.05c (306 particles)

Figure C.8: Particles released at one time step from HOTIS rotor in hover (dynamic PVTM)

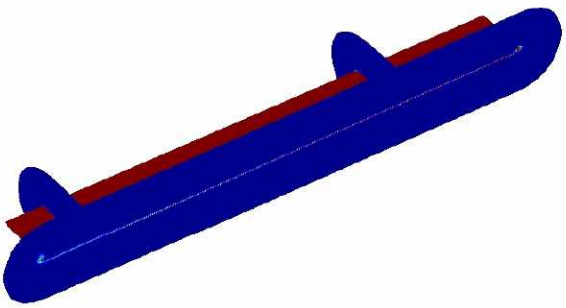

Figure C.9: Vorticity field in RANS domain before conversion

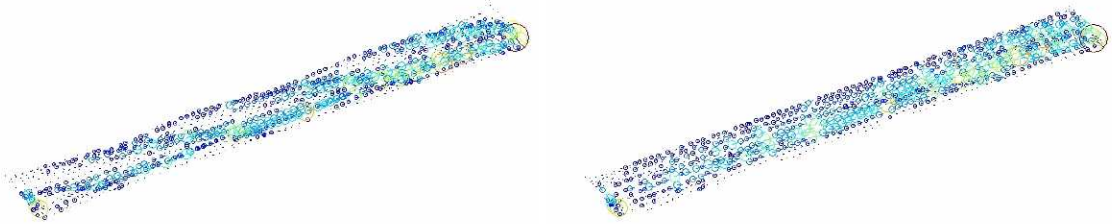

(a) Static PVTM (1001 particles) (b) Dynamic PVTM (902 particles)

Figure C.10: Particle vortex representation of the vorticity field after conversion (d = 0.2c)

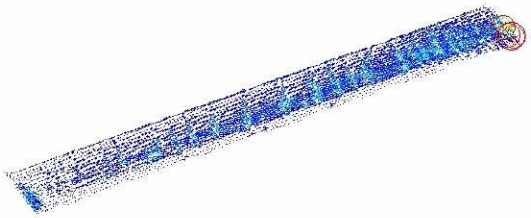

Dynamic PVTM (3999 particles)

Figure C.11: Particle vortex representation of the vorticity field after conversion (d = 0.1c)

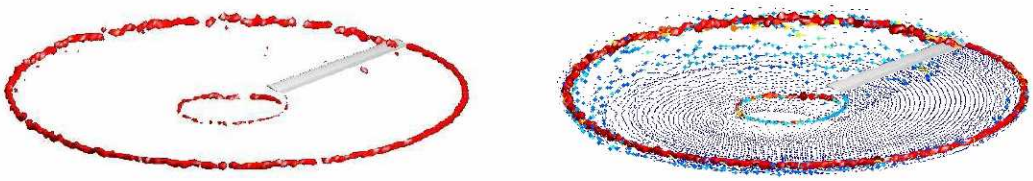

(a) Static PVTM (8178 particles, d = 0.2c)

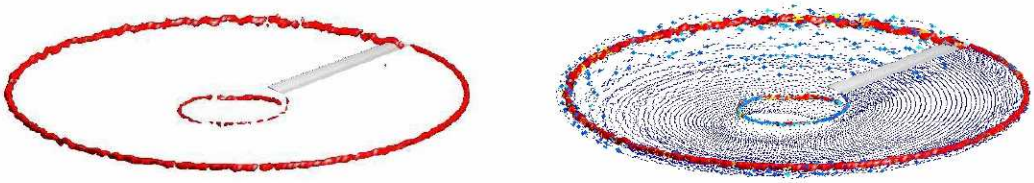

(b) Dynamic PVTM (11411 particles, d = 0.2c)

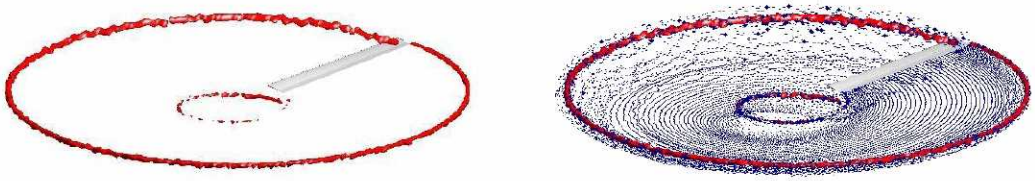

(c) Dynamic PVTM (16481 particles, d = 0.15c)

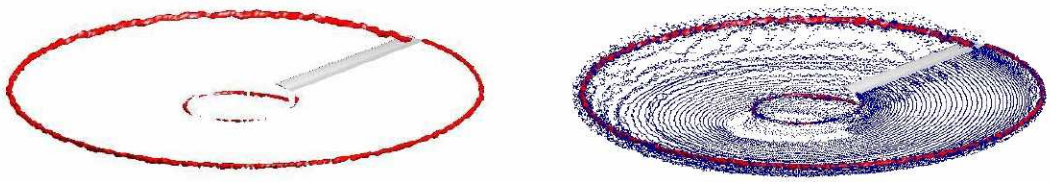

(d) Dynamic PVTM (29018 particles, d = 0.10c)

Figure C.12: Vortex particle field after 1 rotor revolution using static and dynamic PVTM implementations

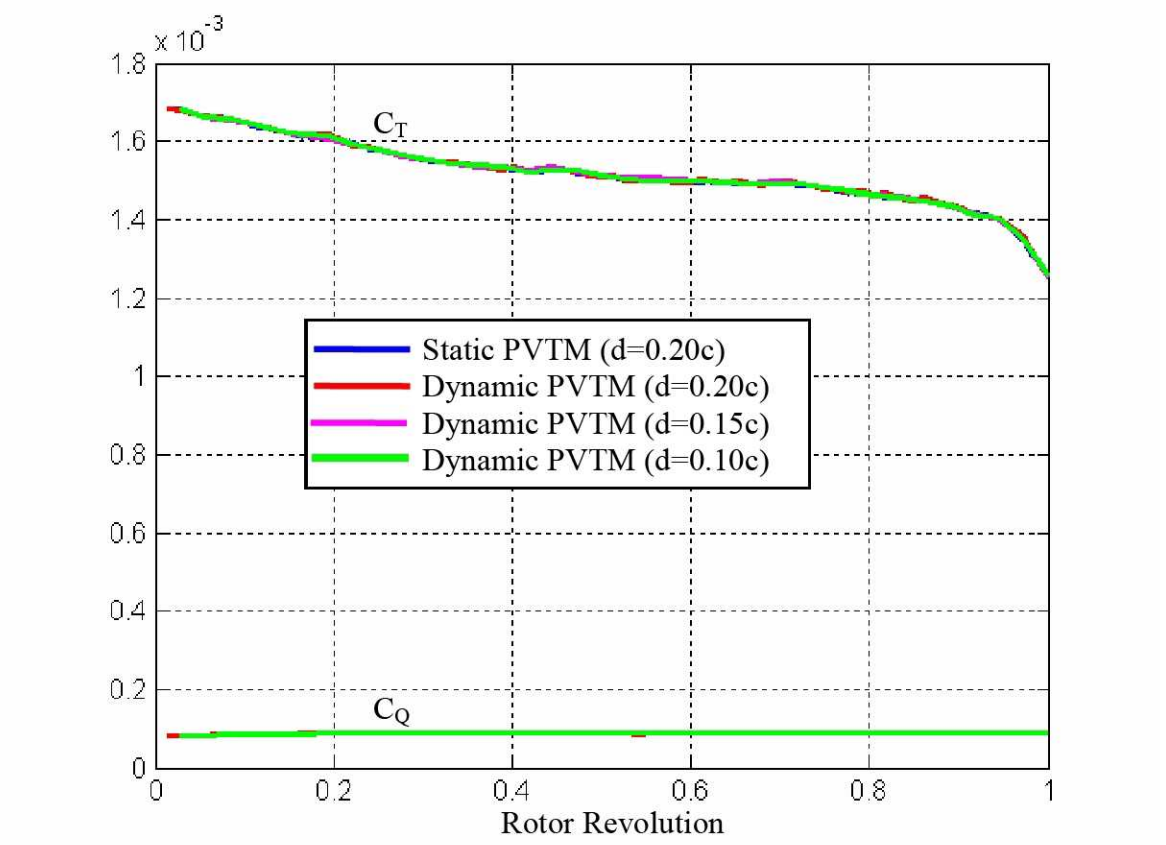

Figure C.13: Comparisons of the blade loading

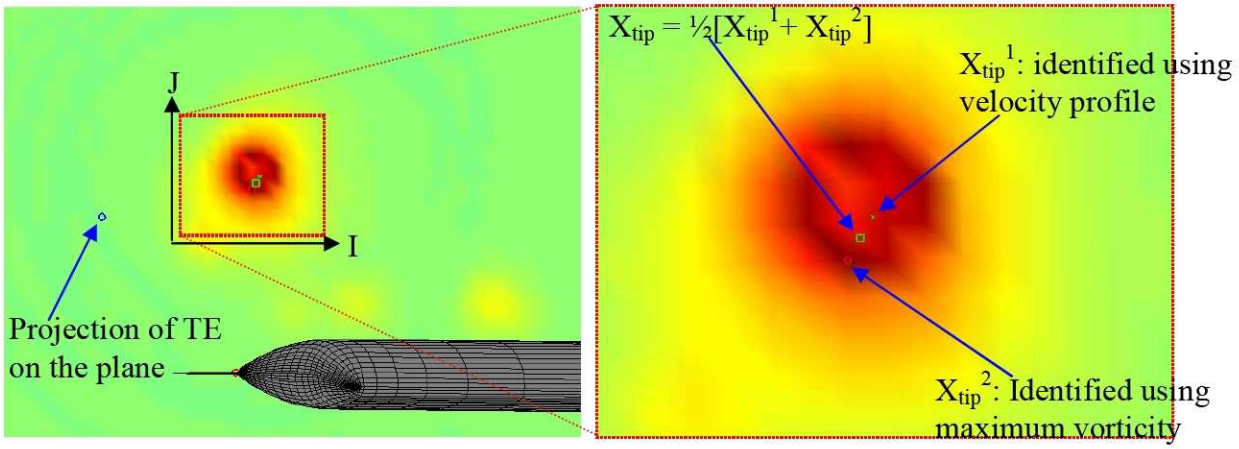

Figure D.1: Vorticity on the measurement plane with the wake age of 10°
(Vorticity strength is perpendicular to the measurement plane)

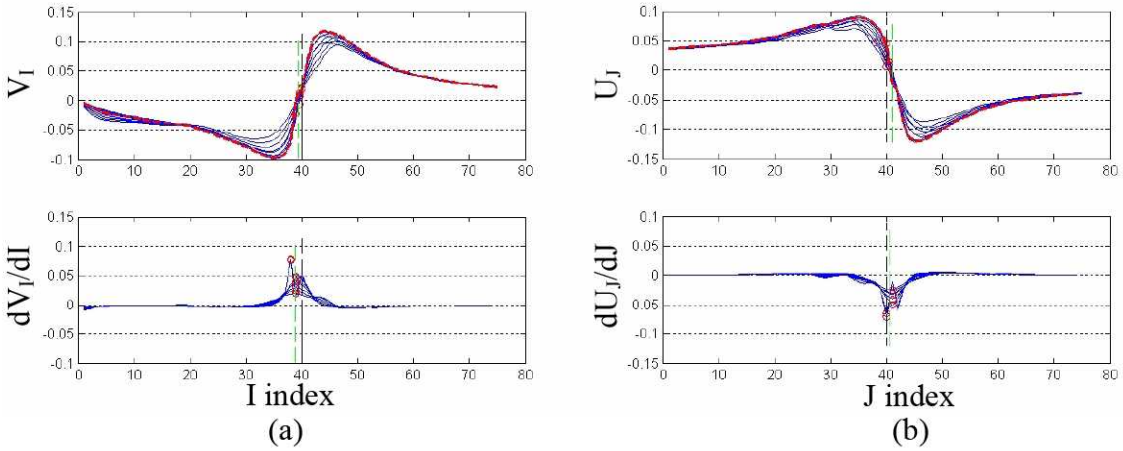

Figure D.2: Identification of tip vortex location using (a) vertical swirl velocity and (b) horizontal swirl velocity

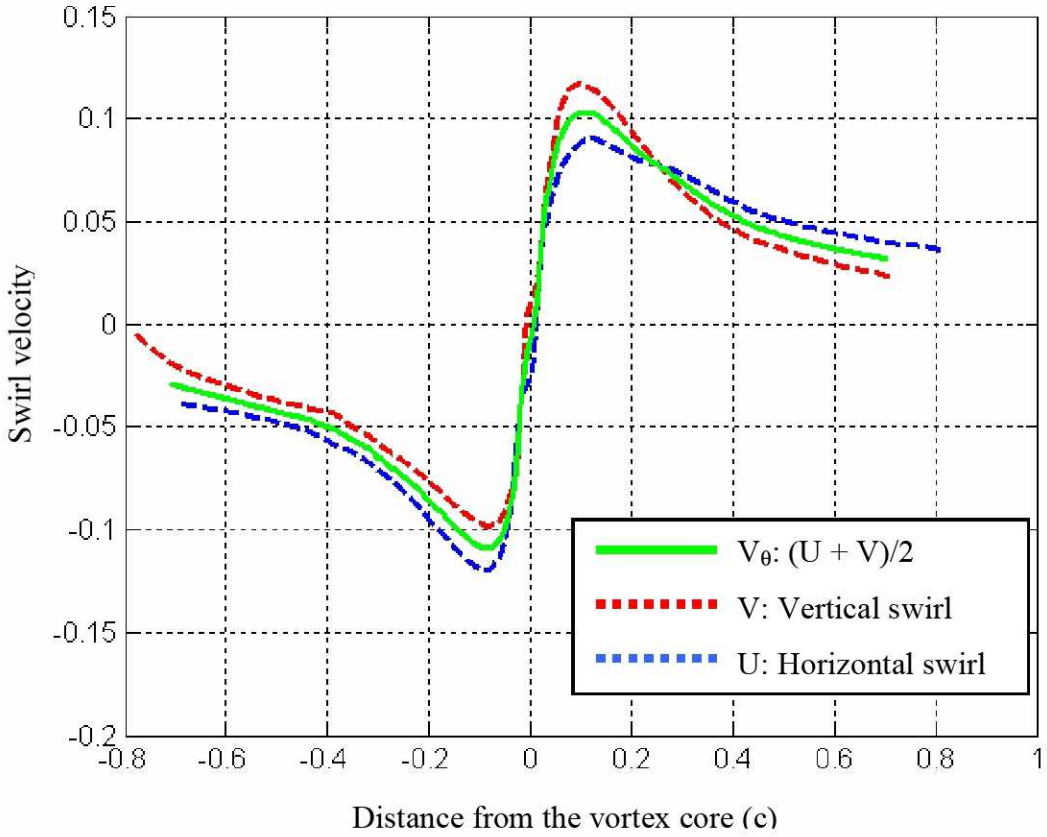

Figure D.3: Swirl velocity of the identified tip vortex

REPORT DOCUMENTATION PAGE

Form Approved
OMB No. 0704-0188

1. REPORT DATE *(DD-MM-YYYY)*	2. REPORT TYPE	3. DATES COVERED *(From - To)*
01- 05 - 2010	Contractor Report	February 2007 - April 2009

4. TITLE AND SUBTITLE
Developments and Validations of Fully Coupled CFD and Particle Vortex Transport Method for High-Fidelity Wake Modeling in Fixed and Rotary Wing Applications

5a. CONTRACT NUMBER
NNL07AA32C

5b. GRANT NUMBER

5c. PROGRAM ELEMENT NUMBER

6. AUTHOR(S)
Anusonti-Inthra, Phuriwat

5d. PROJECT NUMBER

5e. TASK NUMBER

5f. WORK UNIT NUMBER
877868.02.07.07.04.01

7. PERFORMING ORGANIZATION NAME(S) AND ADDRESS(ES)
NASA Langley Research Center
Hampton, VA 23681-2199

National Institute of Aerospace
100 Exploration Way
Hampton, VA 23666

8. PERFORMING ORGANIZATION REPORT NUMBER

9. SPONSORING/MONITORING AGENCY NAME(S) AND ADDRESS(ES)
National Aeronautics and Space Administration
Washington, DC 20546-0001

10. SPONSOR/MONITOR'S ACRONYM(S)
NASA

11. SPONSOR/MONITOR'S REPORT NUMBER(S)
NASA/CR-2010-216697

12. DISTRIBUTION/AVAILABILITY STATEMENT
Unclassified - Unlimited
Subject Category 71
Availability: NASA CASI (443) 757-5802

13. SUPPLEMENTARY NOTES
Langley Technical Monitor: Douglas M. Nark
An electronic version can be found at http://ntrs.nasa.gov

14. ABSTRACT

A novel Computational Fluid Dynamics (CFD) coupling framework using a conventional Reynolds-Averaged Navier-Stokes (RANS) solver to resolve the near-body flow field and a Particle-based Vorticity Transport Method (PVTM) to predict the evolution of the far field wake is developed, refined, and evaluated for fixed and rotary wing cases. For the rotary wing case, the RANS/PVTM modules are loosely coupled to a Computational Structural Dynamics (CSD) module that provides blade motion and vehicle trim information. The PVTM module is refined by the addition of vortex diffusion, stretching, and reorientation models as well as an efficient memory model. Results from the coupled framework are compared with several experimental data sets (a fixed-wing wind tunnel test and a rotary-wing hover test).

15. SUBJECT TERMS
Particle Vorticity Transport Method; Vortex Particle; Rotary Wing Acoustics; Noise

16. SECURITY CLASSIFICATION OF:			17. LIMITATION OF ABSTRACT	18. NUMBER OF PAGES	19a. NAME OF RESPONSIBLE PERSON
a. REPORT	b. ABSTRACT	c. THIS PAGE			STI Help Desk (email: help@sti.nasa.gov)
					19b. TELEPHONE NUMBER *(Include area code)*
U	U	U	UU	104	(443) 757-5802